University of New Orleans

ScholarWorks@UNO

University of New Orleans Theses and Dissertations

Dissertations and Theses

Spring 5-19-2017

Ferroelectric-Semiconductor Systems for New Generation of Solar Cells

Rahmatollah Eskandari
University of New Orleans, New Orleans, reskanda@uno.edu

Follow this and additional works at: https://scholarworks.uno.edu/td

Part of the Semiconductor and Optical Materials Commons

Recommended Citation

Eskandari, Rahmatollah, "Ferroelectric-Semiconductor Systems for New Generation of Solar Cells" (2017). *University of New Orleans Theses and Dissertations*. 2318.
https://scholarworks.uno.edu/td/2318

This Dissertation is protected by copyright and/or related rights. It has been brought to you by ScholarWorks@UNO with permission from the rights-holder(s). You are free to use this Dissertation in any way that is permitted by the copyright and related rights legislation that applies to your use. For other uses you need to obtain permission from the rights-holder(s) directly, unless additional rights are indicated by a Creative Commons license in the record and/or on the work itself.

This Dissertation has been accepted for inclusion in University of New Orleans Theses and Dissertations by an authorized administrator of ScholarWorks@UNO. For more information, please contact scholarworks@uno.edu.

Ferroelectric-Semiconductor Systems for New Generation of Solar Cells

A Dissertation

Submitted to the Graduate Faculty of the
University of New Orleans
in partial fulfillment of the
requirement for the degree of

Doctor of Philosophy
in
Engineering and Applied Science
(Physics)

by

Rahmatollah Eskandari

M.Sc. University of Tabriz, Iran, 2006
B.Sc. Amirkabir University of Technology, Iran, 2002

May, 2017

Copyright 2017

Rahmatollah Eskandari

To:

My Family

Acknowledgement

I would like to express my heartfelt gratitude and appreciation to my advisor Prof. Leszek Malkinski who provided me the excellent opportunity to work and learn in his group. His kindness and patience provided a welcoming environment and his inspiring ideas created an exciting research while his knowledge, experience, and consistent help made the obstacles of the research easy. Thank you Dr. Malkinski.

I am thankful to my committee members Prof. Leonard Spinu, Prof. Weilie Zhou, Prof. Ashok Puri, and Prof. Paul Schilling for their time and helpful suggestions and comments and for supporting my research by providing instruments and helpful advice anytime I needed. I am also grateful to the support from Profs. Kevin Stokes and John Wiley for clarification of many scientific and technical issues. I am also indebted Dr. Xiaodong Zhang from Tulane University for the XPS measurements.

I would like to have this chance to appreciate my former and current group members Dr. Seong-Gi Min, John Gaffney, Ganesh Tiwari, Athanasios Chalastaras, Md Hasan, Atikur Rahman and Happyson Gavi for all the help and support I received from, especially Dr. Min for the training on various scientific instruments and introduction to a field that was little known to me. I would also like to acknowledge my friends in AMRI, Physics and Chemistry departments Dr. Taha Rostamzadeh, Dr. Satish Chandra Rai, Dr. Amin Yourdkhani, Ali Radmanesh, Shankar Khanal, Daniel Adams, Zhi Zheng, Shuke Yan, Dr. Sarah Wozny, Richie Provost, Sara Akbarian, Dr. Darius Montasserasadi, Dr. Parisa Pirani, and Dr. Saman Salemizadeh for the joyful time we shared together at UNO.

I am also thankful to the present and past AMRI office staff Poncho De Leon, Jennifer Tickle, and Amanda Lamastus for all of their help in paperwork and purchasing as well as Dr. Charles G. Seab and Denise Bauer at Physics Department's office for

providing assistantships that was vital to me and for their help. I am also indebted to Harry J. Rees for troubleshooting and fixing of key instruments.

Although no word can fully express my gratitude, my deepest appreciation goes to my wife Zahra Heidari, my father, mother, and my siblings for their never-ending support, patience, and love. I feel blessed to have you in my life and will be indebted forever for all the sacrifices you have made. Thank you.

I would like to thank National Science Foundation for the support through the grant NSF EPSCoR LA-SiGMA Cooperative Agreement No. EPS-1003897, Louisiana Board of Regents Contract No NSF(2010-15)-RII-UNO and UNO for the support via SCORE 2012 grant.

Table of Contents

Abstract ..... **ix**

Part I: Sputtered Si doped Hafnia: Synthesis, and Characterization of Ferroelectric and Photovoltaic Properties

Chapter 1: **2**
Photovoltaic Effect and Ferroelectricity, Theoretical Background **2**
1.1 Introduction 2
1.2 Photovoltaic Theory 4
1.2.1 P-N Junction 5
1.2.2 Schottky Junction 8
1.2.3 Current-Voltage Characteristics and Efficiency 8
1.2.4 Solar Cell Types 11
1.2.4.1 First Generation Solar Cells 11
1.2.4.2 Second Generation Solar Cells 12
1.2.4.3 Third Generation Solar Cells 13
1.2.4.4 New Generations of Solar Cells and Emerging Concepts 14
1.3 Ferroelectricity 15
1.3.1 Hysteretic Behavior in Ferroelectrics 17
1.3.2 Applications of Ferroelectric Materials 19
1.4 Photovoltaic Ferroelectrics 19
1.5 Focus of the Study 21
References 23

Chapter 2: **26**
Synthesis of Ferroelectric HfO_2 Thin Films **26**
2.1 Introduction 26
2.1.1 Ferroelectricity in HfO_2 thin films 28
2.1.2 Crystal Structure of HfO_2 29
2.1.3 Applications of HfO_2 31
2.1.4 Synthesis Methods of Ferroelectric HfO_2 32
2.2 Experimental 33
2.2.1 Sample Preparation and Deposition Conditions 33
2.2.2 Rapid Thermal Annealing 35
2.2.3 Electrode Preparation for Hysteresis Measurement 36
2.2.4 Characterization Methods 38
2.2.4.1 Film Thickness 38
2.2.4.2 Elemental Analysis 38
2.2.4.3 Crystalline Structure 39
2.2.4.4 Ferroelectricity and Hysteresis 39
2.3 Results and Discussion 41
2.3.1 XPS Results 41

2.3.2 Phase Evolution 41
2.3.3 Piezoresponse Force Microscopy of doped HfO_2 Thin Films 44
2.4 Conclusion 45
References 47

Chapter 3: 50
Polarization- Dependent Photovoltaic Effect in Ferroelectric-Semiconductor System 50
3.1 Introduction 50
3.1.1 Photovoltaic Ferroelectrics 50
3.1.2 Design Background (Previous Efforts) 51
3.1.3 Ferroelectricity in Hafnium Dioxide Thin Films 53
3.2 Experimental 53
3.2.1 Sample Preparation 53
3.2.2 Etching 54
3.2.3 Electrode preparation and I-V measurement 55
3.2.4 Poling 55
3.2.5 KPFM 56
3.3 Results and Discussion 58
3.3.1 Surface Potential 58
3.3.2 Current-Voltage 60
3.3.3 Band Diagram 61
3.4 Conclusion 62
References 64

Part II: Synthesis and Characterization of Multifunctional Epitaxial Thin Films for Micro-Origami Applications

Chapter 4: 67
Three-Dimensional Structures Built by Origami Techniques 67
4.1 Introduction to Micro and Nano-Origami 67
4.2 Active Forces in Thin Film Micro-Origami 69
4.2.1 Residual Stress 70
4.2.2 Tension on the Surface 73
4.3 Thin Film Growth 74
4.3.1 Growth Mechanisms 74
4.3.2 Epitaxy 75
4.3.3 Physical Vapor Deposition (PVD) Methods 77
4.3.3.1 Sputter Deposition 77
4.3.3.2 Electron-Beam Deposition 79
4.4 Characterization Methods 80
4.4.1 Reflection High Energy Electron Diffraction (RHEED) 80
4.4.2 Auger Electron Spectroscopy (AES) and Energy Dispersive X-ray Spectroscopy (EDX) 81
4.4.3 Scanning Electron Microscopy (SEM) 83
4.5 Goal of the Study 85
References 87

Chapter 5: 89
Growth of Epitaxial Films for Origami Purposes 89
5.1 Introduction 89
5.1.1 Previous Works (Magnetic Microtubes) 90
5.2 Experimental (Synthesis and Characterization Tools) 93
5.3 Results. 95
5.3.1 Epitaxy of Zinc (Zn) on Sapphire 95
5.3.1.1 Zinc on Sapphire with Ru buffer layer 97
5.3.1.1.1 RHEED Results 98
5.3.1.1.2 AES Results 100
5.3.1.1.3 SEM Results 101
5.3.1.2 Zinc on Sapphire with Ti Buffer Layer 105
5.3.1.2.1 RHEED Results 106
5.3.1.2.2 SEM Results 107
5.3.2 Epitaxy of NaCl on MgO 109
5.3.3 Epitaxy of Cr and Fe on MgO 110
5.4 Conclusion 112
References 114

Appendix: Copyright Permissions 115

VITA 123

Abstract

This dissertation includes two parts. In the first part the study is focused on the fabrication of multifunctional thin films for photovoltaic applications. There is no doubt about the importance of transforming world reliance from traditional energy resources, mainly fossil fuel, into renewable energies. Photovoltaic section still owns very small portion of the production, despite its fast growth and vast research investments. New methods and concepts are proposed in order to improve the efficiency of traditional solar cells or introduce new platforms. Recently, ferroelectric photovoltaics have gained interest among researchers. First objective in application of ferroelectric material is to utilize its large electric field as a replacement for or improvement of built-in electric field in semiconductor p-n junctions which is responsible for the separation of generated electron-hole pairs. Increase in built in electric field will increase open-circuit voltage of the solar cell.

In this regard, thin films of ferroelectric hafnium dioxide doped with silicon have been fabricated using physical vapor deposition techniques. Scanning probe microscopy techniques (PFM and KPFM) have been employed to analyze ferroelectric response and surface potential of the sample. The effects of poling direction of the ferroelectric film on the surface potential and current-voltage characteristics of the cell have been investigated. The results showed that the direction of poling affects photoresponse of the cell and based on the direction it can either improved or diminished.

In the second part of this work, epitaxial thin films have been synthesized with physical vapor deposition techniques such as sputtering and electron beam evaporation for the ultimate goal of producing multifunctional three-dimensional structures. Three-dimensional structures have been used for applications such as magnetic sensors, filters,

micro-robots and can be used for modification of the surface of solar cells in order to improve light absorption and efficiency. One of the important techniques for producing 3-D structures is using origami techniques. The effectiveness of this technique depends on the control of parameters which define direction of bending and rolling of the film or curvature of the structure based on the residual stress in the structure after film's release and on the quality and uniformity of the film. In epitaxially grown films, the magnitude and direction of the stress are optimized, so the control over direction of rolling or bending of the film can be controlled more accurately. For this purpose, deposition conditions for epitaxy of Zn, Fe, Ru, Ti, NaCl and Cr on Si, Al_2O_3 or MgO substrates have been investigated and optimized. Crystallinity, composition and morphology of the films were characterized using reflective high energy diffraction (RHEED), Auger electron spectroscopy (AES), energy dispersive X-ray (EDX), and scanning electron microscopy (SEM).

Keywords: photovoltaic, ferroelectric, hafnium dioxide, polarization, micro-origami, epitaxy.

Part I

Sputtered Si-doped Hafnia: Synthesis, and Characterization of Ferroelectric and Photovoltaic Properties

Chapter 1:

Photovoltaic Effect and Ferroelectricity, Theoretical Background

1.1 Introduction

Our economy, transportation, government, health system and schools, buildings and roads are all relied on energy which primarily comes from fossil fuels such as oil, natural gas, and coal as well as nuclear energy. The common aspect of these resources (except nuclear energy) is their limited reserves. The best predictions estimate the lifetime of resources such as oil and gas to be around 100 years. The main drawback for these types of resources, besides their limits, would be the environmental pollution and the increase in the amount of CO_2 which is proven to contribute to the global warming. Adding the growth rate of the world population and the amount of energy needed to provide the basic comfort for all humans and to keep the economy running, would legitimize the need for an alternative source of energy that is abundant and clean. Energy from the sun seems to be the best answer for all of these challenges, although the vanishing fossil fuels are indeed originated from the sun, too. Solar rays carry a tremendous amount of energy in which solar radiation that reaches the surface of the earth in a single year would be more than 7500 times the world's total annual need for energy. This abundant source of energy could be harvested directly and indirectly by different means. The direct method is to capture the radiation and convert it into electricity using a photovoltaic module. Although, high production cost and low efficiency of photovoltaic modules in the past decades made them economically unjustified for large commercial use, the recent advancement in technology reduced their cost to a point where they become even more

efficient than traditional sources of energies in some areas.[1] In Table 1-1 projected Levelized cost of energy (LCOE) for different energy sectors are listed. What is important in this table is the decrease in the production cost of renewable energy resources such as the wind and solar PV. These projections show about %68 decrease in solar PV costs and more than %50 on wind sector which makes it even cheaper than coal and advanced nuclear energy and also competitive with natural gas in the year 2020.[2,3]

By the year 2011, installed capacity of solar power plants were 68.8GW which shows nearly five times increase in the sector capacity compared to the 14.5GW capacity of the year 2008. World Energy Council also Predicts a 70 percent share of the energy production market to the solar family, including photovoltaics and solar-thermal power plants for the year 2100.[1]

These projections and current and planned investments show the importance of renewable energy sector, especially solar photovoltaics in the future. In this chapter, the theory behind the photovoltaic phenomenon and the traditional designs and structures of solar cells are briefly listed and explained.

Table 1-1: Projected Levelized cost of energy (LCOE) for different energy sectors. Projections for the year 2016 and 2020 were made on the years 2010 and 2015, respectively.

Estimates in %/MWh	Conventional Coal	Natural Gas (Advanced Combined Cycle)	Advanced Nuclear	Wind (Onshore)	Solar PV
2016[2]	110.4	79.3	119.0	149.3	396.1
2020[3]	95.1	72.6	95.2	73.6	125.3
% change	-13.9	-8.4	-20	-50.1	-68.4

1.2 Photovoltaic Theory

In 1839, French physicist, Edmond Becquerel discovered the photovoltaic effect when he made the first ever solar cell using platinum electrodes covered with silver chloride and dipped in an electrolytic solution.[4] Later in 1870s photovoltaic properties were discovered in selenium, however, the importance of this effect as a capable source of energy was not realized until 1950s due to the low efficiency of the cells. In 1954, Chapin from Bell Labs reported 6 percent conversion efficiency in a single crystal p-n junction silicon solar cell.[5] After this breakthrough, research on photovoltaic cells gained more speed, initially focusing more on non-terrestrial applications mainly due to the high production cost which was only bearable by space programs. During the next decades, different combinations of semiconductors were introduced for photovoltaic applications.

A photovoltaic cell by definition is a structure in which absorbs energy in the form of a photon (UV-IR range) and produces electrical current. Key components are required for a cell to successfully complete this reaction. First, it needs a material that can absorb the photons and produce free electron-hole pairs and later a driving force that separates these electron-hole pairs and pushes them towards the appropriate electrode.[6,7]

The absorption process takes place in a semiconductor material with a band gap value that provides absorption at the visible range radiation. Light absorption causes the electron to be excited and by gaining energy of the photons move from valence band to the conduction band, leaving a hole behind. These electron and hole pairs will have freedom to move inside semiconductor due to their elevated energy level and they move towards opposite electrodes resulting in a net current when subjected to electric force. This driving force generally is formed at the junction of two media with different work functions. This junction can be formed between a metal and a semiconductor or between two semiconductors. The junction between a metal and semiconductor is called a Schottky

junction and the junction between two semiconductors is generally referred as a p-n junction.[6,7]

1.2.1 P-N Junction

A solar cell is a typical p-n junction device and a p-n junction is made by joining two semiconductor materials that are doped with the different types of dopants. Silicon owns the majority of semiconductor devices due to its abundance, stability, and mature technology; however pure silicon is intrinsic, meaning that the numbers of electrons and holes that are free to move are equal. Intrinsic silicon at zero Kelvin has no free charges and by increasing the temperature, electrons get excited and gain enough energy to move inside the material. For this reason, the resistivity of an intrinsic semiconductor is infinite at zero Kelvin and it falls by rising temperature. However, their resistivity is generally higher than typical conductors and lower than insulators.

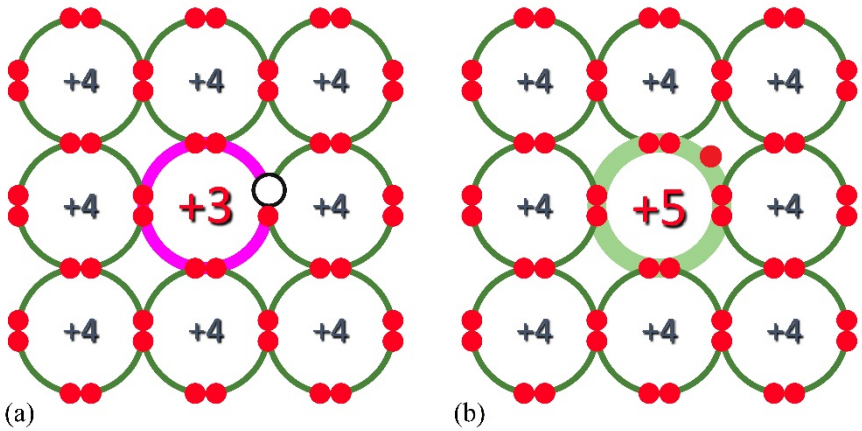

Figure 1-1. Schematic representation of p-type silicon doped with boron (a) and n-type silicon doped with arsenic or phosphorus (b).

Silicon's valence band is full and has four electrons. This balance between electron and hole inside the intrinsic silicon can be changed by doping silicon with elements such as boron (B) which only has three electrons in the valence band (an electron less than Si) or by elements such as arsenic (As) and phosphorous (P) which have five electrons in the valence band (one electron more than Si). Doping with elements which have fewer electron changes the balance in favor of the holes (p-type) and dopants with extra electron adds more free electrons to the semiconductor (n-type). Figure 1-1 represents a schematic of the atomic structure of p-type and n-type silicon.

When n-type and p-type semiconductors join together, electrons at n-type and holes at p-type diffuse into the other medium due to their different concentration on both sides which gives them different energy levels. This migration of carriers builds a positively charged region inside n-type and a negatively charged region inside p-type semiconductor and builds up an opposing electric field. The diffusion of charges continues until electric field becomes strong enough to stop them. The magnitude and distribution of the electric field at the junction depend on the doping level in each of the semiconductors (Figure 1-2b) and it defines the magnitude of the potential difference (voltage) between electrodes of the solar cell.

The region which is built at the junction becomes free of carriers and is called depletion zone or depletion layer. Any free carrier at this zone will be driven to one direction due to the existing electric field. Recombination rate will be small inside this zone and it increases at the edges due to the decrease in the magnitude of the electric field (Figure 1-2c).Under illumination of light, photons with the energy larger than the bandgap get absorbed and produce electron-hole pairs in the whole device, however, only those who are created inside the depletion zone and those that are located within the

diffusion length from the depletion zone and can diffuse into the zone, contribute to the net solar current.

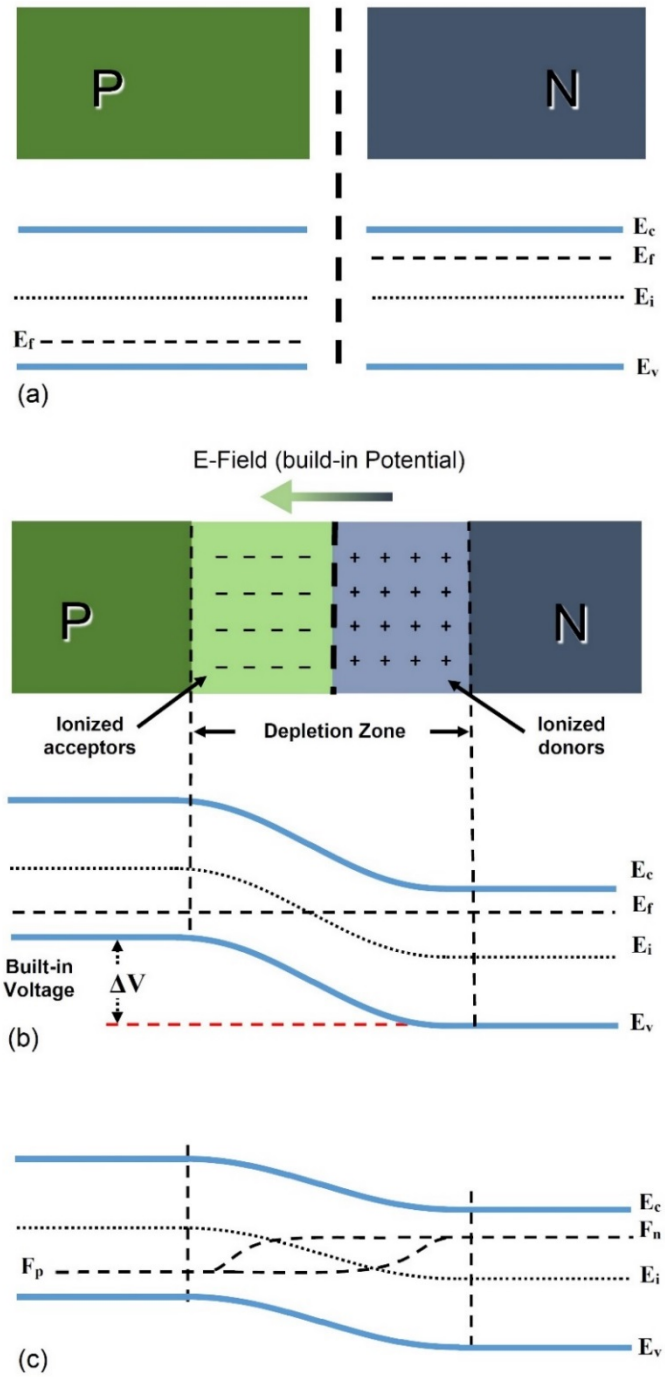

Figure 1-2. Formation of depletion zone at the junction between a p-type and an n-type semiconductor before two semiconductors' joining (a) and after joining together and building a junction at equilibrium conditions (b) and under illumination of light (c).

The p-n junction can be formed by joining any p-type semiconductor with any n-type semiconductor. If the joining parts have been made from same element or compound, such as silicon which has been explained, the junction is called a homojunction. If the junction is formed by two different compound or elements, it has been called heterojunction.

1.2.2 Schottky Junction

When a semiconductor is in contact with a metal, a similar alignment between the fermi level of metal and semiconductor takes place. Depending on the type of the semiconductor and position of its work function with respect to the metal, either ohmic contact or Schottky contact can be formed.

For a p-type semiconductor if the work function is higher than that of the metal, an ohmic contact forms which results in no resistance for the carriers to pass the junction. However, if the work function is lower than that of the metal, a Schottky junction is created which serves as a barrier in front of the holes. This junction creates a similar situation as a p-n junction which results in a driving force towards one direction for the carriers and blocking barrier to the opposite direction.

A similar situation can happen for an n-type semiconductor with a higher work function than joining metal which results in the creation of a Schottky junction. Some early solar cells worked based on the Schottky junction.

1.2.3 Current-Voltage Characteristics and Efficiency

Typical current-voltage (I-V) curve for a solar cell is depicted in Figure 1-3. The curve is same as a nonlinear diode current-voltage graph when it is in darkness but it shifts with the exposure to the light and produces open circuit voltage of V_{oc} and short-

circuit current of I_{sc}. The nonlinearity of this graph depends on the shunt resistance (R_{sh}) and series resistance (R_s) of the device. The best cells require small series resistance and large shunt resistance in order to acquire maximum efficiency. Figure 1-4 represents an equivalent circuit that includes important parameters in a solar cell. Large shunt resistance and small series resistance are necessary to maximize output current and voltage. Optimum shunt and series resistances increase the fill factor (FF) which is defined as the ratio of the maximum power output and product of V_{oc} and I_{sc}:

$$FF = \frac{V_m \times I_m}{V_{oc} \times I_{sc}} = \frac{P_m}{V_{oc} \times I_{sc}} \qquad (1-1)$$

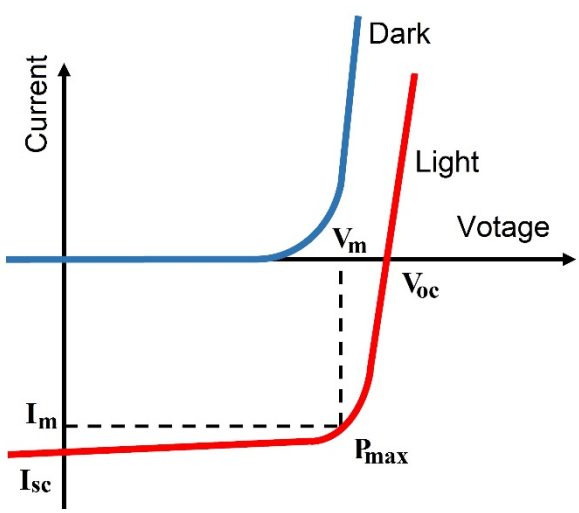

Figure 1-3. Typical I-V diagram for a solar cell in dark and under light.

The efficiency of solar cells is defined as the ratio of maximum output power to the power of incident light:

$$\eta = \frac{V_{oc} \times I_{sc} \times FF}{Incident\ power} = \frac{P_m}{Incident\ power} \qquad (1-2)$$

To some approximation, open-circuit voltage can be related to the band gap with a direct relationship. This implies that maximum possible photovoltage cannot exceed energy bandgap of the semiconductor. Besides, increasing the band gap will result in the dissipation of photons with lower energy. This means that increasing energy bandgap will decrease the amount of absorbed photons which lowers the efficiency. So, there is an optimum value for the band gap that can lead to a maximum efficiency by keeping the product of $V_{oc} \times I_{sc}$ maximized. This value has been calculated to be around 1.5 eV. Semiconductors that are used in solar cells, mostly have an energy bandgap at the range of 1.1 to 1.7 eV such as c-Si (1.12 eV), α-Si (1.7 eV), GaAs (1.4 eV), InP (1.3 eV), CdTe (1.5 eV) and CIGS (1.0-1.7 eV).[6,8,7]

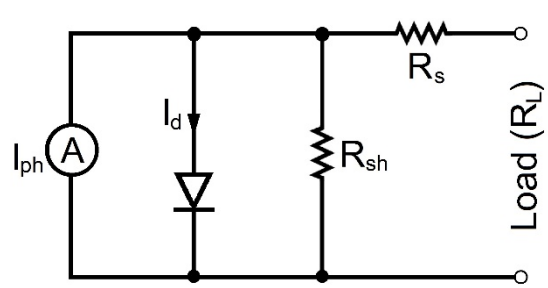

Figure 1-4. Equivalent representation of important factors in a solar cell.

1.2.4 Solar Cell Types

1.2.4.1 First-Generation Solar Cells

Traditionally, solar cells are classified into three main categories. First generation solar cells are mainly referred to single-crystalline and polycrystalline solar cells. This generation dominates the photovoltaic market due to their higher efficiency and high stability, despite their higher production cost. Polycrystalline cells are less efficient than single-crystalline cells but can be produced cheaper. The record values for c-Si and polycrystalline Si cells are 26.3% and 21.3%, respectively.[9] The grain boundaries in polycrystalline cells act as recombination sites and decrease the effective diffusion length of the carriers.[10,11] Figure 1-4 represents the relationship between the average grain size and efficiency of the solar cell.

GaAs and InP also fall in this category with a substantial difference as compared with silicon. Silicon has an indirect bandgap of 1.12 eV, while GaAs and InP have direct band gaps. The difference between direct and indirect bandgap is that in a direct gap semiconductor, the maximum of the valence band (VB) and the minimum of the conduction band (CB) occur at the same value of wavenumber (**k**). In this case, a photon with energy equal to E_g is enough to transfer an electron from VB to CB. In contrast, in an indirect bandgap, maximum VB and minimum CB don't happen at the same value of **k**. Therefore, in order to transfer an electron from VB to CB, a change in the momentum of the electron is required and since photons cannot provide this, lattice vibrations (phonons) with appropriate value get absorbed and change the momentum. Having a direct band gap increases the chance of photon absorption in a way that absorption coefficient drops very fast as depth of the semiconductor increases, meaning that for a direct bandgap a very thin layer (~1 µm for GaAs) is enough to capture all of the possible light while for silicon a thickness of more than 100 µm is required.[12]

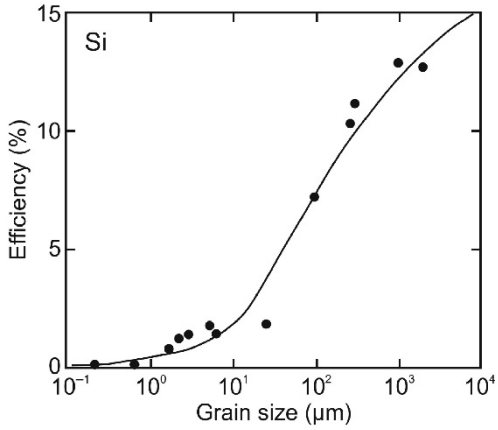

Figure 1-5. Relationship between grain size and efficiency of silicon solar cells (reprinted with permission from Ref. 11)

1.2.4.2 Second-Generation Solar Cells

Silicon has an indirect bandgap, so in order to absorb enough photons, a fairly thick layer of silicon is needed. This makes the cost of the crystalline and polycrystalline silicon solar cells high. In contrast, a solar cell that employs a direct bandgap semiconductor as an absorber doesn't require a thick layer of the material. Generally, a thin layer (~ 1μm) is enough for total possible absorption of light. This generation is also referred as thin film solar cells. $CuInSe_2$ (CIS) is a typical material in this category with 1 eV bandgap. An improved version of this type is $Cu(In,Ga)(Se,S)_2$ (CIGS) with a bit larger bandgap (1.2-1.6 eV), but improved efficiency. The record value for the efficiency of CIGS cells is 21.0% obtained by Solibro on 2014.[9] Cadmium telluride (CdTe) is another compound which is made by thin film deposition methods and has gained a huge attention due to the record efficiency of 21.0%.[9] These solar cells are built on the glass and this makes them cheaper than silicon solar cells and increases the competitiveness of this generation. A distinct characteristic of the second generation of solar cells is the incorporation of rare elements such as In, Ga, Te and Cd in their structures.[11–19]

These solar cells are built on glass instead of the silicon wafer, so the production cost is lower compared to silicon cells. Cheaper cost compensates lower efficiency of thin film solar cells and makes them competitive with crystalline silicon solar cells.

Amorphous silicon (α-silicon) solar cells are also considered as second generation solar cells. The structure is an imperfect ordering of silicon atoms with many dangling bonds which are bonded by hydrogen. This α-Si:H material is hard to be doped and doping also introduces more dangling bonds and imperfections which increase recombination rate and decrease diffusion length of the carriers. For these reasons, these cells are made in the form of a p-i-n structure. The intrinsic layer is responsible for the absorption of light and production of carriers. Usually, plasma-enhanced chemical vapor deposition method has been used for fabrication of α-Si:H solar cells. These cells, however, suffer from degradation which is a drawback for them, despite of their cheap and easy production methods.[19–21] The record value for the efficiency of these cells is about 10% for single junction and 14% for multiple junction structures.[9]

1.2.4.3 Third-Generation Solar Cells

The third generation of solar cells are generally referred to multijunction solar cells, concentrated and other high-efficiency solar cells. In multijunction cells, the goal is to capture the maximum possible light using different layers that operate at different energy levels. The junctions that are on the top generally have the largest bandgap, so they absorb high energy photons and permit the lower energy photons to pass. The energy gap is lowered step by step in lower junctions in order to capture the maximum of the light. The components of these cells are mainly comprised of ternary and quaternary compounds of III-V elements such as Ga, As, In, P, Al and so on. The efficiency record for these types are above 45%, however, their high cost makes them only applicable for special applications such as space missions.[9,22–26]

1.2.4.4 New Generations of Solar Cells and Emerging Concepts

Along with the above-mentioned structures, research is undergoing on other types of materials such as organic compounds, dyes, and perovskites. Organic solar cells, as the name implies are based on organic donor and acceptor media. They are designed in the form of a single junction and multijunction cells with a unique characteristic. The contact does not necessarily need to be in the form of a lamellar structure, so the acceptor and donor media can be blended which substantially increases the contact surface between donor and acceptor and improves separation of photogenerated electron-hole carriers.[21,27,28] Their record efficiency is about 11.2%.[9]

Dye-sensitized solar cells (DSSC) were first introduced in the 1990s and have grown from initial 7% efficiency[29] to the record of about 13%, recently.[30] Synthesis of DSSCs is easy and can be done by simple methods such as printing. They can be produced as transparent cells giving them decorative capabilities besides power generation and also can be made on flexible substrates. Although their efficiency is much lower than previous generations, their low production cost and less sensitivity to production parameters have made them competitive in the market.[31]

Perovskite solar cells created an excitement wave in photovoltaic research community during the most recent years. Their efficiency has rapidly reached the level of conventional solar cells to about 15% in 2013 after their introduction in 2009 and it shockingly boosted to about 20% in two years. [28,32–38] The name perovskite was taken from the name of the crystal structure of the absorber material that is used. The perovskite's molecular structure are in the form of ABX_3, with X referring to oxide or halide anions. These cells, however, have a drawback which holds them from practical applications and that is their sensitivity to the moisture.[34,35]

Ferroelectric photovoltaics are among the newest concepts that envision promising improvements in the efficiency of solar cells by increasing open-circuit voltage of the cells. This class utilizes polarization field from a ferroelectric material which can be of the order of tens of volts to separate photogenerated electron-hole pairs. The design for this class is focused on two groups: the first group considers a combination of a ferroelectric material with a semiconductor material.[39,40] In this design, polarization field from the ferroelectric material is employed for separation of carriers and semiconducting material has the role of absorbing the light and generation of the carriers. On the other hand, in the second group, the ferroelectric material is used alone and takes the role of absorption of the light, generation, and separation of the carriers, altogether.[41–44]

In our work that is performed at Advanced Materials Research Institute at the University of New Orleans, the effect of the combination of a thin layer of ferroelectric material with a semiconductor material with the aim of achieving new ferroelectric photovoltaic system has been investigated. In order to better understand the working principle of these cells, in the next sections, ferroelectricity has been briefly explained and then operational principles of the photovoltaic phenomenon in ferroelectrics and ferroelectrics combined with semiconductors have been introduced.

1.3 Ferroelectricity

Although the first ferroelectric compound that was discovered on the early 1920s was Rochelle salt, its very complicated structure and difficulties in the production of this ferroelectric compound, gave it an inconsiderable role among ferroelectrics these days. Practically first generations of ferroelectrics were synthesized later which were mainly phosphate crystals such as KH_2PO_4 and were ferroelectric in very low temperatures. Early theories of ferroelectricity were based on these crystal structures and suggested that the

ferroelectricity requires hydrogen bond(s) in their structure to introduce polarity. This made the ferroelectricity a dull topic for researchers until 1945 when ferroelectricity was discovered in $BaTiO_3$ (BTO). This opened a new era for ferroelectric research society, since BTO abandoned the hydrogen bond hypothesis and its exquisite properties such as chemical and mechanical stability, above room temperature and simple crystal structure with just five atoms per unit cell, made it the most favorable compound. Different compounds with structures similar to BTO (known as ABO_3 perovskite structure) and with ferroelectric properties were discovered soon after, in which $LiNbO_3$, $LiTaO_3$, and $PbTiO_3$ were among the first.

Ferroelectric materials are classified as a subgroup of pyroelectrics which themselves are part of a larger group called piezoelectrics. Piezoelectrics in general definition are referred to the materials that can build electrical dipoles under a mechanical stress or can create mechanical movement under applied voltage. Among all types of piezoelectric materials, only ferroelectrics and pyroelectrics can retain this polarization permanently. This permanent polarization is based on the asymmetry in the crystal structure which creates a permanent separation between the center of positive and negative ions in the lattice and leads to the formation of a dipole inside every lattice. All ferroelectrics show this property in a specific temperature range and beyond that temperature which is known as Curie temperature, undergo a phase transition with the loss of the permanent polarization. The new phase is referred to paraelectric.

These dipoles actually are always present inside the ferroelectric material, however, they are randomly oriented in a way that they cancel each other. The section with all dipoles in the same direction is called a domain. The macroscopic polarization becomes maximum when the dipoles of all domains align in the same direction. The direction of these dipoles can be switched in any direction by application of strong electric fields along

the desired direction. So, all domains can be aligned in the same direction under a high voltage.[45]

1.3.1 Hysteretic Behavior in Ferroelectrics

Ferroelectrics are characterized by their hysteresis graph which gives information about their polarization capability under electric field and values that can determine the magnitude of permanent polarization and required electric field for switching the polarization. By applying an electric field to the ceramic, domains start switching to the same direction as the applied electric field, until all domains are pointing to the same direction. Polarization becomes maximum as it is been called saturation polarization (P_s). By removing electric field part of these domains may turn again due to depolarization fields, however, the bulk material holds a net polarization which is called a remanent polarization (P_r). The electric field can be applied in the opposite direction resulting in further reversing the dipoles until the net polarization becomes zero. The electric field that is required to depolarize a polarized ferroelectric is called the coercive electric field (E_c). Figure 1-6 depicts a typical polarization-electric field (P-E) for a ferroelectric and shows the important quantities on the graph.

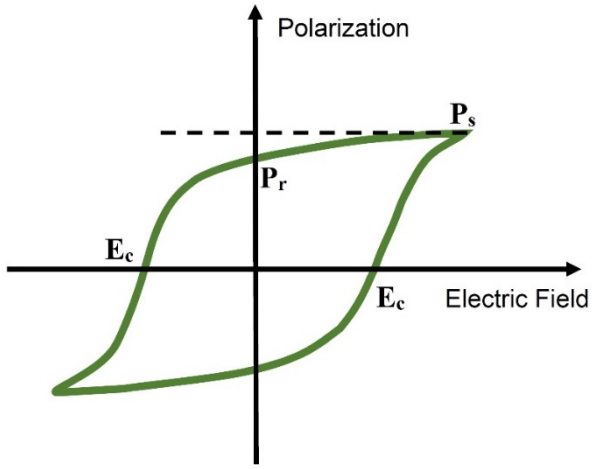

Figure 1-6. Typical P-E hysteresis graph for a ferroelectric material.

As mentioned, ferroelectricity is intimately related to the crystal structure and only non-centrosymmetric space groups can exhibit ferroelectricity. Most of the ferroelectrics crystallize in the form of ABO_3 perovskite crystal structure. Figure 1-7 depicts this crystal structure at ferroelectric and non-erroelectric phases. Permanent polarization results from dislocating Ti or Zr atoms from the center of the oxygen tetrahedron along c-axis which leads to mechanical deformation of the lattice and macroscopic movements in the direction of polarization.

This mechanical response is the evidence for piezoelectric properties of the sample and can be the first step in the characterization of ferroelectric materials.[45]

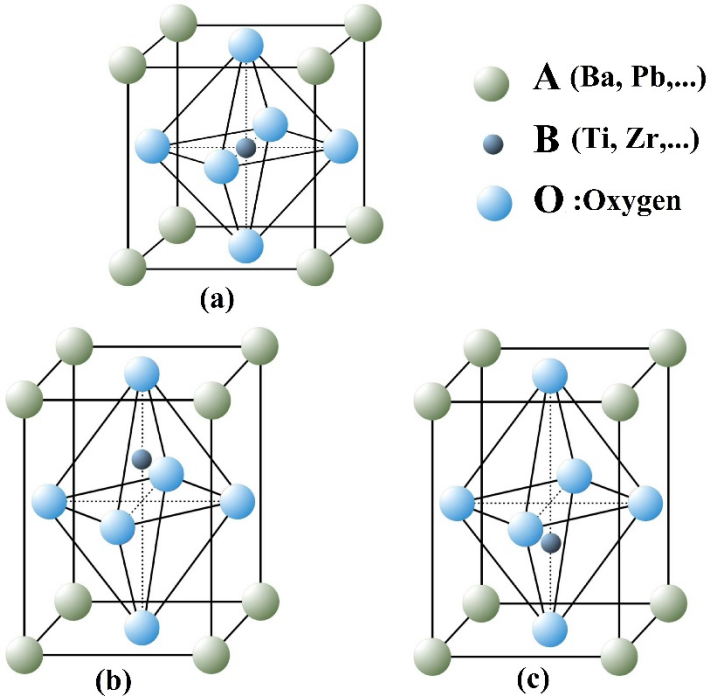

Figure 1-7. ABO_3 perovskite crystal structure of ferroelectrics (a) Material at non-ferroelectric phase ($T>T_c$), (b) and (c) Material at ferroelectric phase ($T<T_c$) with permanent polarization downward and upward.

1.3.2 Applications of Ferroelectric Materials

Ferroelectric (FE) materials have diverse applications either in bulk or in thin film form. FE capacitors are simply a ferroelectric layer that is sandwiched between two conductive electrodes. Their difference as compared with dielectric capacitors is that permittivity in FE capacitors can be tuned, so the capacitance is tunable. This brings them applications in microwave circuits. They have applications in sensors, actuators and micro-electromechanical systems (MEMS), micro-positioning, and more importantly in the non-volatile memory area.

Hysteresis behavior of FEs gives them an important role in the memory industry. They are extensively used as ferroelectric field effect transistors (FeFET) and ferroelectric random access memories (FeRAM).[46] There have been numerous efforts to incorporate conventional ferroelectrics such as $BaTiO_3$ (BTO), $SrBi_2Ta_2O_9$(SBT), $Pb(Zr,Ti)O_3$ (PZT), $BiFeO_3$ (BFO)[47–49] and also organic PVDF:TrFE[50] in the structure of FeRAMs and FeFETs. Ferroelectric tunnel junctions are also built relying upon a ferroelectric material.[51–54]

The most recent and fairly new utilization of ferroelectric materials is in photovoltaic applications which is the same as the subject of this work.[40,41,55–62]

1.4 Photovoltaic Ferroelectrics

As we have mentioned, traditional solar cells use the electric field at the p-n junction for separation of the electron-hole pairs. The fact that design of this junction necessitates considering crystal structure, bandgap, and alignment of two different materials limits materials' choice and complicates the technological aspects of the fabrication.[40]

In conventional photovoltaic cells, absorption of light introduces electron-hole pairs into the semiconductor and later these electrons and holes are separated from each other by the built-in electric field that is present in the depletion region of the p-n junction. So, the maximum voltage that a cell can produce depends on the bandgap of the semiconductor and even more on the alignment of the bands in the junction. The highest voltage that a conventional cell has achieved is smaller than 1V, however, results show that incorporation of a ferroelectric material in the structure of the cells even as a very thin film of a ferroelectric material, can produce a photovoltage as large as several volts.[44,63]

The main target in ferroelectric solar cells is to alter either built-in voltage or to introduce a new force for separation of electron-hole pairs using the potential arising from polarized ferroelectric particles or films[59]. For photovoltaic ferroelectrics, it has been observed that a homogeneous short-circuited crystal displays a photocurrent in the direction of spontaneous polarization under uniform illumination.[42]

Different designs have been proposed for ferroelectric photovoltaics which can be classified into two groups: In one group ferroelectric materials are responsible for the production of charge carriers besides providing the separating force, while in the other group, ferroelectrics are mixed with semiconductors and their large internal field from polarization is utilized to improve the driving force for the separation of charges. Unfortunately, due to the large energy bandgap of these materials, the absorption of light will be very small (Table 1-2). Thus, incorporation of ferroelectrics and semiconductors seems to be necessary.

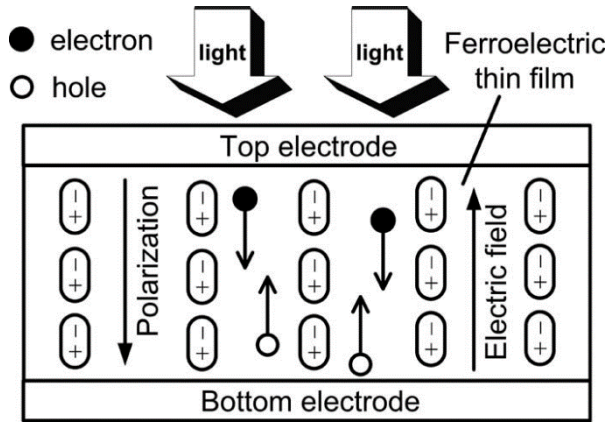

Figure 1-8. Schematic mechanism of a ferroelectric photovoltaic effect
(reprint with permission from Ref.61)

Photovoltaic properties of thin film ferroelectrics can be utilized in miniaturized devices in wide applications such as microsensors, MEMS, and microactuators. Qin et al.[61] have shown a conversion efficiency of 0.28 percent with a thin epitaxial film of $(Pb_{0.97}La_{0.03})(Zr_{0.52}Ti_{0.48})O_3$ (PLZT) sputter deposited on a conductive Nb-doped $SrTiO_3$ substrate and sandwiched with $La_{0.7}Sr_{0.3}MnO_3$. The photovoltaic effect has been investigated in well-known ferroelectric materials such as $Pb(Zr,Ti)O_3$,[64–66] $LiNbO_3$,[67] $BiFeO_3$,[41,56,60,68–70] and $BaTiO_3$.[40]

Table 1-2: Energy bandgap of some known ferroelectric compounds

Ferroelectric Compound	Band Gap (eV)	Reference
$BaTiO_3$	3.47	[71]
$BiFeO_3$	2.67	[42]
$LiNbO_3$	4.7	[72]
$Pb(Zr,Ti)O_3$	3.9 -4.4	[66]

1.5 Focus of the Study

The goal of this work was to improve the third stage of the photovoltaic phenomenon which is the separation of carriers by introducing a ferroelectric material and

employing its polarization field in order to create and/or improve the built-in electric field. Initially, the work was focused on the use of ferroelectric BTO nanoparticles and their composite combination with different semiconductors such as Si, CdS, CdSe and ZnO. As an example, for the structures that were prepared by sandwiching ferroelectric BTO nanoparticles between n-type and p-type silicon (n-Si/BTO/p-Si), initial results were promising and effect of the polarization of nanoparticles were observed on the transport characteristics of the structure, however, the devices were full of imperfections due the existing nanoparticles and the results were not repeatable.

The research then, focused on the fabrication of a thin ferroelectric film which could avoid the creation of imperfections on the cell structure and small thickness of the layer could allow transport via tunneling and other mechanisms. Doped hafnium dioxide was selected as the ferroelectric material for the study since it could hold ferroelectricity at very thin films. The compound was fairly new to the researchers and there were no reports on the fabrication of this compound with sputtering. So, first, the experimental conditions were optimized in order to produce a ferroelectric film of doped hafnia using the radio-frequency sputtering method. This part has been discussed in chapter two and in chapter three, the effect of polarization of very thin ferroelectric film of doped hafnia on the photoresponse of a lamellar device comprised of this ferroelectric film and a semiconductor layer has been explained.

References

1. World Energy Council. *World Energy Resources, 2013 Survey.* (2013).
2. Energy Information Administration. *2016 Levelized Cost of New Generation Resources from the Annual Energy Outlook 2010.* (2009).
3. Energy Information Administration. *Levelized cost and levelized avoided cost of new generation resources in the annual energy outlook.* (2015).
4. Williams, R. Bequerel photovoltaic effect in binary compounds. *J. Chem. Phys.* **32,** 1505–1514 (1960).
5. Chapin, D. M., Fuller, C. S. & Pearson, G. L. A new silicon p-n junction photocell for converting solar radiation into electrical power. *J. Appl. Phys.* **25,** 676–677 (1954).
6. Sze, S. M. & Ng, K. K. *Physics of semiconductor devices.* (Wiley-Interscience, 2007).
7. Grundmann, M. *The Physics of Semiconductors.* (Springer Berlin Heidelberg, 2010).
8. Würfel, P. *Physics of solar cells : from basic principles to advanced concepts.* (Wiley-VCH, 2009).
9. Green, M. A. *et al.* Solar cell efficiency tables (version 49). *Prog. Photovoltaics Res. Appl.* **25,** 3–13 (2017).
10. Werner, J., Taretto, K. & Rau, U. Grain Boundary Recombination in Thin-Film Silicon Solar Cells. *Solid State Phenom.* **80–81,** 299–304 (2001).
11. Ghosh, A. K., Fishman, C. & Feng, T. Theory of the electrical and photovoltaic properties of polycrystalline silicon. *J. Appl. Phys.* **51,** 446–454 (1980).
12. Reddy, P. J. *Science and technology of photovoltaics.* (BS Publications, CRC Press, 2009).
13. Rockett, A. & Birkmire, R. W. $CulnSe_2$ for phatsvoltaic applications. *October* **70,** (1991).
14. Bhattacharya, R. N. *et al.* High efficiency thin-film $CuIn_{1-x}Ga_xSe_2$ photovoltaic cells using a $Cd_{1-x}Zn_xS$ buffer layer. *Appl. Phys. Lett.* **89,** 88–89 (2006).
15. Chu, T. L. *et al.* 13.4% efficient thin-film CdS/CdTe solar cells. *J. Appl. Phys.* **70,** 7608–7612 (1991).
16. Roussillon, Y., Karpov, V. G., Shvydka, D., Compaan, A. D. & Giolando, D. M. Reach-through mechanism in CdS/CdTe solar cells. *Conf. Rec. IEEE Photovolt. Spec. Conf.* 340–342 (2005).
17. Singh, V. P., Lush, G. B., Santiesteban, R., McClure, J. C. & Chavez, H. Cadmium telluride films for lightweight solar cells for space and terrestrial applications. *AIP Conf. Proc.* **325,** 235–241 (1995).
18. Bai, Z., Yang, J. & Wang, D. Thin film CdTe solar cells with an absorber layer thickness in micro- and sub-micrometer scale. *Appl. Phys. Lett.* **99,** (2011).
19. Chopra, K. L., Paulson, P. D. & Dutta, V. Thin-film solar cells: an overview. *Prog. photovoltaics* **12,** 69–92 (2004).
20. Shah, A. V *et al.* Thin-film silicon solar cell technology. *Prog. Photovoltaics* **12,** 113–142 (2004).
21. Parida, B., Iniyan, S. & Goic, R. A review of solar photovoltaic technologies. *Renew. Sustain. Energy Rev.* **15,** 1625–1636 (2011).
22. Dimroth, F. High-efficiency solar cells from III-V compound semiconductors. *Phys. status solidi* **3,** 373–379 (2006).
23. King, R. R. *et al.* 40% efficient metamorphic GaInP/GaInAs/Ge multijunction solar cells. *Appl. Phys. Lett.* **90,** 183516 (2007).
24. Taek Kim. Multijunction solar cell. (2010).
25. Kinsey, G. S. *et al.* Concentrator multijunction solar cell characteristics under variable intensity and temperature. *Prog. Photovoltaics Res. Appl.* **16,** 503–508 (2008).
26. Dimroth, F. & Kurtz, S. High-efficiency Multijunction Solar Cells. *MRS Bull.* **32,** 230–235 (2007).

27. Ragoussi, M.-E. & Torres, T. New generation solar cells: concepts, trends and perspectives. *Chem. Commun.* **51,** 3957–3972 (2015).
28. Noh, J. H., Im, S. H., Heo, J. H., Mandal, T. N. & Seok, S. Il. Chemical Management for Colorful, E ffi cient, and Stable Inorganic − Organic Hybrid Nanostructured Solar Cells. *Nano Lett.* **13,** 1764–1769 (2013).
29. O'Regan, B. & Grätzel, M. A low-cost, high-efficiency solar cell based on dye-sensitized colloidal TiO_2 films. *Nature* **353,** 737–740 (1991).
30. Mathew, S. *et al.* Dye-sensitized solar cells with 13% efficiency achieved through the molecular engineering of porphyrin sensitizers. *Nat. Chem.* **6,** 242–247 (2014).
31. Grätzel, M. Recent Advances in Sensitized Mesoscopic Solar Cells. *Acc. Chem. Res.* **42,** 1788–1798 (2009).
32. Liu, M., Johnston, M. B. & Snaith, H. J. Efficient planar heterojunction perovskite solar cells by vapour deposition. *Nature* **501,** 395–398 (2013).
33. Yang, W. S. *et al.* High-performance photovoltaic perovskite layers fabricated through intramolecular exchange. *Science* **348,** 1234–1237 (2015).
34. Service, R. F. Perovskite Solar Cells Keep On Surging. *Science* **344,** 458 (2014).
35. Snaith, H. J. Perovskites : The Emergence of a New Era for Low-Cost , High-. *J. Phys. Chem. Lett* **4,** 3623−3630 (2013).
36. Lee, M., Teuscher, J., Miyasaka, T., Murakami, T. & Snaith, H. Efficient hybrid solar cells based on meso-superstructured organometal halide perovskites. *Science* **338,** 643–647 (2012).
37. Kojima, A., Teshima, K., Shirai, Y. & Miyasaka, T. Organometal Halide Perovskites as Visible-Light Sensitizers for Photovoltaic Cells. *J. Am. Chem. Soc.* **131,** 6050–6051 (2009).
38. Kim, H. S., Im, S. H. & Park, N. Organolead halide perovskite: new horizons in solar cell research. *J. Phys. Chem. C* **118,** 5615–5625 (2014).
39. Yuan, Y. *et al.* Efficiency enhancement in organic solar cells with ferroelectric polymers. *Nat. Mater.* **10,** 296–302 (2011).
40. Liu, F., Wang, W., Wang, L. & Yang, G. Ferroelectric-semiconductor photovoltaics: Non-PN junction solar cells. *Appl. Phys. Lett.* **104,** 103907 (2014).
41. Choi, T., Lee, S., Choi, Y. J., Kiryukhin, V. & Cheong, S. W. Switchable Ferroelectric Diode and Photovoltaic Effect in $BiFeO_3$. *Science* **324,** 63–66 (2009).
42. Basu, S. R. *et al.* Photoconductivity in $BiFeO_3$ thin films. *Appl. Phys. Lett.* **92,** 91905 (2008).
43. Cao, D. *et al.* High-Efficiency Ferroelectric-Film Solar Cells with an n-type Cu_2O Cathode Buffer Layer. *Nano Lett.* **12,** 2803–2809 (2012).
44. Yao, K., Gan, B. K., Chen, M. & Shannigrahi, S. Large photo-induced voltage in a ferroelectric thin film with in-plane polarization. *Appl. Phys. Lett.* **87,** 212906 (2005).
45. Lines, M. E. & Glass, A. M. *Principles and Applications of Ferroelectrics and Related Materials.* (Oxford University Press, 2001).
46. Suzuki, M. & Ami, T. A proposal of epitaxial oxide thin film structures for future oxide electronics. *Mater. Sci. Eng. B* **41,** 166–173 (1996).
47. Mikolajick, T. *et al.* FeRAM technology for high density applications. *Microelectron. Reliab.* **41,** 947–950 (2001).
48. Ishiwara, H. Impurity substitution effects in $BiFeO_3$ thin films-From a viewpoint of FeRAM applications. *Curr. Appl. Phys.* **12,** 603–611 (2012).
49. Zhang, M. M., Jia, Z. & Ren, T. L. Effects of electrodes on the properties of sol-gel PZT based capacitors in FeRAM. *Solid. State. Electron.* **53,** 473–477 (2009).

50. Lim, S. H., Rastogi, A. C. & Desu, S. B. Electrical properties of metal-ferroelectric-insulator-semiconductor structures based on ferroelectric polyvinylidene fluoride copolymer film gate for nonvolatile random access memory application. *J. Appl. Phys.* **96,** 5673–5682 (2004).
51. Garcia, V. & Bibes, M. Ferroelectric tunnel junctions for information storage and processing. *Nat. Commun.* **5,** 4289 (2014).
52. Wen, Z., Li, C., Wu, D., Li, A. & Ming, N. Ferroelectric-field-effect-enhanced electroresistance in metal/ferroelectric/semiconductor tunnel junctions. *Nat. Mater.* **12,** 617–621 (2013).
53. Zhuravlev, M. Y., Sabirianov, R. F., Jaswal, S. S. & Tsymbal, E. Y. Giant electroresistance in ferroelectric tunnel junctions. *Phys. Rev. Lett.* **94,** 1–4 (2005).
54. Scott, J. F. Ferroelectric Memories Today. *Ferroelectrics* **236,** 247–258 (2000).
55. Dong, W. *et al.* Enhanced Photovoltaic Effect in $BiVO_4$ Semiconductor by Incorporation with an Ultrathin $BiFeO_3$ Ferroelectric Layer. *ACS Appl. Mater. Interfaces* **5,** 6925–6929 (2013).
56. Sung, J. H. *et al.* Single ferroelectric-domain photovoltaic switch based on lateral $BiFeO_3$ cells. *NPG Asia Mater.* **5,** e38-5 (2013).
57. Fei, L. *et al.* Electrospun bismuth ferrite nanofibers for potential applications in ferroelectric photovoltaic devices. *ACS Appl. Mater. Interfaces* **7,** 3665–3670 (2015).
58. Guo, R. *et al.* Non-volatile memory based on the ferroelectric photovoltaic effect. *Nat. Commun.* **4,** 1990 (2013).
59. Zhang, J. *et al.* Enlarging photovoltaic effect: combination of classic photoelectric and ferroelectric photovoltaic effects. *Sci. Rep.* **3,** 1–6 (2013).
60. Yang, S. Y. *et al.* Photovoltaic effects in $BiFeO_3$. *Appl. Phys. Lett.* **95,** 62909 (2009).
61. Qin, M., Yao, K. & Liang, Y. C. High efficient photovoltaics in nanoscaled ferroelectric thin films. *Appl. Phys. Lett.* **93,** 122904 (2008).
62. Huang, H. Ferroelectric photovoltaics. *Nat. Photonics* **4,** 134 (2010).
63. Yang, S. Y. *et al.* Above-bandgap voltages from ferroelectric photovoltaic devices. *Nat. Nanotechnol.* **5,** 143–147 (2010).
64. Pintilie, L. in *Ferroelectrics: Physical Effects* 101–134 (InTech, 2009).
65. Kholkin, A., Boiarkine, O. & Setter, N. Transient photocurrents in lead zirconate titanate thin films. *Appl. Phys. Lett.* **72,** 130–132 (1998).
66. Pintilie, L., Vrejoiu, I., Le Rhun, G. & Alexe, M. Short-circuit photocurrent in epitaxial lead zirconate-titanate thin films. *J. Appl. Phys.* **101,** 64109 (2007).
67. Glass, A. M., Linde, D. von der & Negran, T. J. High-voltage bulk photovoltaic effect and the photorefractive process in $LiNbO_3$. *Appl. Phys. Lett.* **25,** 233 (1974).
68. Wu, F. *et al.* Photovoltaic effect of a bilayer thin film with $(Na_{0.5}Bi_{0.5})_{1-x}Ba_xTiO_3/BiFeO_3$ heterostructure. *J. Phys. D. Appl. Phys.* **46,** 365304 (2013).
69. Wang, C. *et al.* Switchable diode effect and ferroelectric resistive switching in epitaxial BiFeO3 thin films. *Appl. Phys. Lett.* **98,** 1–4 (2011).
70. Yan, F., Chen, G., Lu, L. & Spanier, J. E. Dynamics of photogenerated surface charge on $BiFeO_3$ films. *ACS Nano* **6,** 2353–60 (2012).
71. Suzuki, K. & Kijima, K. Optical Band Gap of Barium Titanate Nanoparticles Prepared by RF-plasma Chemical Vapor Deposition. *Jpn. J. Appl. Phys.* **44,** 2081–2082 (2005).
72. Thierfelder, C., Sanna, S., Schindlmayr, A. & Schmidt, W. G. Do we know the band gap of lithium niobate? *Phys. status solidi* **7,** 362–365 (2010).

Chapter 2:

Synthesis of Ferroelectric HfO_2 Thin Films

2.1 Introduction

Ferroelectric (FE) thin films that are utilized in electronic devices are mostly based on conventional perovskite ferroelectrics such as $BaTiO_3$ (BTO), $SrBi_2Ta_2O_9$(SBT), $Pb(Zr,Ti)O_3$ (PZT), and $SrTiO_3$(STO).[1] There are obstacles in the way of employing these materials in advanced electronic devices; despite few advancements that were reported recently on epitaxial growth of some of these oxides on silicon,[2,3] growth of these materials on silicon, still suffers from their incompatibility with silicon substrate, which is the basement for semiconductor and chip industry. Their growth is always accompanied by building a thin SiO_2 layer which introduces a depolarization field that weakens the effectiveness of the ferroelectric film and its polarization.[4,5] In the case of PZT which is the most used ferroelectric, toxicity of lead (Pb) has always been an environmental concern. Adding to these, the need for a minimum thickness for the creation and maintaining the remanent polarization at most of the conventional FEs makes them infeasible to be embedded into the structure of the advanced semiconductor devices such as ferroelectric field effect transistors (FeFET) and ferroelectric random access memories (FeRAM).[6] Besides all, the need for higher bandgap dielectrics that can serve as a perfect insulator in transistors encourages researchers to look for thinner FEs with higher band gap and high permittivity (κ).[7]

Figure 2-1 is the variation trend of some key dimensions in transistors predicted for ten years[8] which implies the need for materials that while supporting smaller node dimensions, can also provide better characteristics compared to the former material.

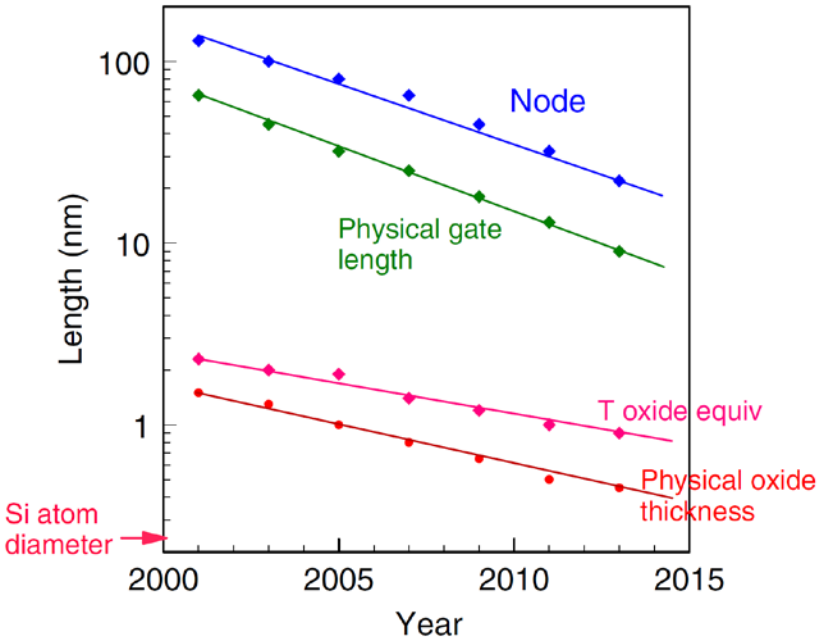

Figure 2-1. The trend of the scale of the node size, gate length, and oxide thickness[8].

Hafnium dioxide (HfO_2) is known for having attractive dielectric properties and comparably high permittivity ($\kappa = 25$) versus SiO_2 ($\kappa = 3.9$).[9] Due to the larger dielectric constant of HfO_2, a layer of HfO_2 with the same thickness as a SiO_2 layer would provide better insulation and can better adapt to lower dimension technologies that are emerging. Additionally, it can decrease the power consumption of the electronic devices due to the low leakage current. Eventually, it can be expected to take the role of SiO_2 as the dominant gate material in transistors as their size is shrinking year after year.

Unlike transistors, ferroelectric field effect transistors (FeFET) and ferroelectric random access memories (FeRAM) require more than a simple gate material. Retaining ferroelectric properties while satisfying low dimensional requirements is the main challenge

for these devices. There have been numerous efforts to incorporate conventional ferroelectrics such as BTO, PZT, SBT, BFO[10–12] and also organic PVDF:TrFE[13] in the structure of FeRAMs and FeFETs, however, instability and degradation of ferroelectric properties in these films is the major impediment as dimensions fall below 100nm. Worth adding that their deposition mechanism is not compatible with the industry, too.[14]

2.1.1 Ferroelectricity in HfO_2 thin films

Discovery of ferroelectricity in Si-doped HfO_2 thin films introduced a candidate for small dimensions that can adapt to 2× nm technology.[15] Ferroelectricity was also reported in doped HfO_2 films with variable amounts of other elements such as zirconium,[16] aluminum,[17] and yttrium.[18] Hafnium oxide has advantages over other metal oxides; it has a band gap that is wide enough to provide dielectric insulation with low leakage and it is also stable on silicon and SiO_2, thus compatible with silicon technology.[19] Now, with the addition of ferroelectric properties at low dimensions, it will be an ideal candidate for electronic devices that require direct ferroelectric/silicon junctions such as FeFET and capacitors.[15,20] Ferroelectric thin films of HfO_2 after optimizing the properties based on silicon content and film thickness, have been embedded in the structure of FeFET.[21] Several studies show that ferroelectricity in hafnium oxide starts showing up by increasing the doping level of silicon from zero percent and maximizes at about %4. Pure HfO_2 shows paraelectric polarization and addition of silicon introduces ferroelectricity in the film. Further increase of silicon content to %5 and higher changes the film into an antiferroelectric (AFE) and eventually fading the ferroelectric properties when it reaches the level of %10. Beside the silicon content, also the effects of film thickness and annealing temperature have been investigated and it has been shown that films as thin as 9 nm show clear and stable ferroelectric properties and ferroelectricity could last for films up to

30nm, though the effect weakens at thicknesses above 20nm. Films that are annealed at temperature of at least 800ºC showed higher remanent polarization (P_r) compared to those that were annealed at lower temperatures.[15,20–23]

2.1.2 Crystal Structure of HfO_2

Hafnium oxide crystallizes in four monoclinic, cubic, tetragonal and orthorhombic phases with different space groups. It was shown that even at room temperature, HfO_2 grows in monoclinic crystalline phase and this is attributed to the low-temperature crystallization of HfO_2 amorphous films.[24] Tetragonal and cubic phases need temperatures higher than 2050°K and 2803°K, respectively[25] and orthorhombic phase needs higher pressure for stabilization.[26] When crystallization occurs, tetragonal phase forms in nanocrystals even at low temperatures, but further growth of the crystals makes this phase unstable and forces them to transform back into the monoclinic phase.[27]

Mechanical confinement was shown to have an important role on crystallization. Annealing of HfO_2 films when they are capped with TiN layer, produces a mixture of tetragonal and monoclinic phases.[28] The role of capping layer is to provide mechanical stress and prevent possible dewetting between the substrate and HfO_2 film which can cause the formation of voids in the film.[28] Doping such as the addition of 5-10 mol. % of Si, capping layer and radius of impurities can stabilize tetragonal, cubic and orthorhombic phases at ambient conditions.[20,29] A major role of SiO_2 in this system is to increase the crystallization temperature of Si:HfO_2, favoring a controlled crystallization after capping. A secondary role of SiO_2 is to reduce the stability of the monoclinic phas.[29]

Before the discovery of ferroelectricity in HfO_2, all phase structures for bulk HfO_2 were known to be centrosymmetric and non-polar like space groups Pbcm, Pbca, $P2_1/c$, $P4_2/nmc$ and $Fm\bar{3}$;m. So, bulk HfO_2 cannot be ferroelectric.[30] However, the shreds of

evidence that Böscke and his colleagues gathered proved existing ferroelectric phase for HfO_2. They suggested a new non-centrosymmetric phase that could be considered for thin films (around 20nm) of HfO_2. They found reports[31–33] showing similar behavior for ZrO_2 when it was doped with Mg, crystallized in orthorhombic phase with the space group of $Pbc2_1$ (=$Pca2_1$). Considering all similarities between HfO_2 and ZrO_2, a non-centrosymmetric phase with space group $Pbc2_1$ was suggested for HfO_2 which is orthorhombic and has ferroelectric properties.[15] Theoretical calculations confirmed that orthorhombic phases with $Pca2_1$ and $Pmn2_1$ space groups can be existed and are the polar phases of doped hafnia.[26]

Figure 2-2 represents a schematic of the crystal structure of the hafnia in tetragonal and orthorhombic phases. Positions of atoms in non-polar tetragonal phase and in upward and downward polarized form of the polar orthorhombic phase are specified.

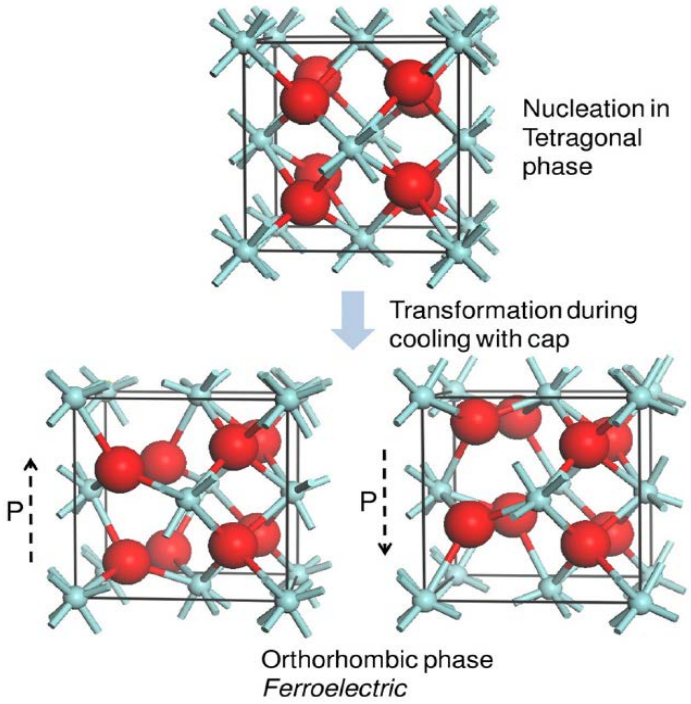

Figure 2-2. The phase transformation of HfO_2 from tetragonal ($P4_2/nmc$) into polar orthorhombic ($Pca2_1$). Up and down polarization states are shown (reprinted with permission from15)

As mentioned above, specific conditions such as doping and sandwiching the film between layers while annealing at high temperatures would ascertain the creation and stabilization of other phases besides monoclinic. In order to assure the creation of a polar ferroelectric phase in the film, those specific conditions need to be applied altogether. As an example, when the crystallization process is applied to a 10 nm thin film of HfO_2 which is doped with less than 4 mol.% of silicon, a mixture of monoclinic and tetragonal phases forms, however, when the same film is encapsulated between two layers, formation of these phases is suppressed and ferroelectric orthorhombic phase forms.[15,20]

Annealing is necessary to the crystallization, however, annealing of an amorphous film and a crystalline film may not both yield identical results. Böscke et al. interestingly found that when the Si:HfO_2 films are crystallized prior to annealing, the formation of desired properties such as capacitance and crystalline phase won't occur. Therefore, preparing an amorphous film of Si:HfO_2 which is capped between layers, besides observing the right mole ratio of silicon dopant, is essential to obtain the ferroelectric properties. His studies showed that when the mole ratio of silicon vs hafnium drops below 4 mol. %, ferroelectric properties become evident, while above that doping level, films lean more towards antiferroelectric.[15] It has been also found that films that are made with ion-assisted deposition (IAD) method below 300°C show amorphous structure.[34]

2.1.3 Applications of HfO_2

As discussed, hafnium oxide is considered one of the best candidates to replace SiO_2 as the gate dielectric in complementary metal–oxide–semiconductor (CMOS) and ferroelectric phase of it is compatible with the CMOS technology.[35,36] Hafnium oxide, however, has interesting optical properties which make it noteworthy for researchers. It is considered a good thermal barrier with high transparency from ultraviolet to the mid-

infrared region. Its transparency in the visible range does not sacrifice transparency in the near- to the mid-IR region. High refractive index (about 2 in the visible region) and melting point (2900 ºC) beside excellent thermal and chemical stability, makes this compound an excellent candidate for high index optical coatings and a good alternative to zirconium dioxide in visible and IR as well. Its applications include coatings in mirrors, anti-reflective coatings and interference filters.[34,37–42]

2.1.4 Synthesis Methods of Ferroelectric HfO_2

Although a vast number of methods have been used to fabricate hafnium oxide films, for films with ferroelectric properties, not all of the methods have been explored. To date, ion-assisted deposition (IAD)[34], metal organic atomic layer deposition (MOALD)[15] and atomic layer deposition (ALD)[28] were suggested and utilized to prepare ferroelectric HfO_2 thin films doped with silicon.

The MOALD process is based on Tetrakis-(ethylmethylamino)-hafnium (TEMA-Hf), Tetrakis-dimethylamino-silane (4DMAS), metalorganic precursors, and ozone. The level of silicon dopant is adjusted by changing the number and cycle ratio of precursors. Later, deposited films of doped HfO_2 with 7-10 nm thickness are capped with TiN and annealed at variable temperatures (higher than 500ºC) with rapid thermal annealing system to induce the crystallization.[15]

For the ALD method, $HfCl_4$ and D_2O are used as precursors and deposited on oxide surface at temperatures between 200°C to 350°C. Thin films of 3-20 nm thick doped hafnium oxide are capped with TiN layer and rapid thermal annealed at 1000°C for 5s in the nitrogen ambient. For characterization of HfO_2 films, the TiN capping layer is generally removed with a selective wet etch (NH_4OH (50 vol. %): H_2O_2 (30%): H_2O = 1:2:40).[28] An increase in the level of chlorine impurities and voids in the film is expected as the

deposition temperature decreases from 300 to 200°C.[43] Higher deposition temperature (e.g., 300°C vs 200°C) and post deposition annealing lower impurities and consequently improves electrical characteristics of the film. In general, properties of the films that are produced with ALD method can be tuned by deposition temperature, the precursor type, and post deposition processing.[43–48]

2.2 Experimental

2.2.1 Sample Preparation and Deposition Conditions

Hafnium dioxide thin films doped with different amounts of silicon (ranging from 6 to 10 percent) were fabricated by means of RF sputtering. Small pieces of n-type silicon chips were cut to cover a specific portion of the target's surface area and then mounted on the two inch diameter hafnium target (99.9%, K.J. Lesker Co.) using silver paste (Figure 2-3.).

N-type silicon wafers with (001) orientation were used as the substrate. As received wafers were cleaned according to the solvent clean procedure; Wafers were ultra-sonicated in acetone for 15minutes then dipped in hot (55ºC) acetone for 10minutes and then in hot (55ºC) isopropyl alcohol (IPA) for 10minutes. Each step followed by de-ionized (DI) water rinse. Cleaned wafers from organics and dust, dipped in hydrofluoric acid (HF, 4 vol. %) for two minutes in order to remove native oxide and followed by continuous DI water rinse for several minutes and at the end dried by nitrogen blow. Cleaned wafers were immediately mounted on the holder with stainless steel clips and loaded into the load-lock chamber.

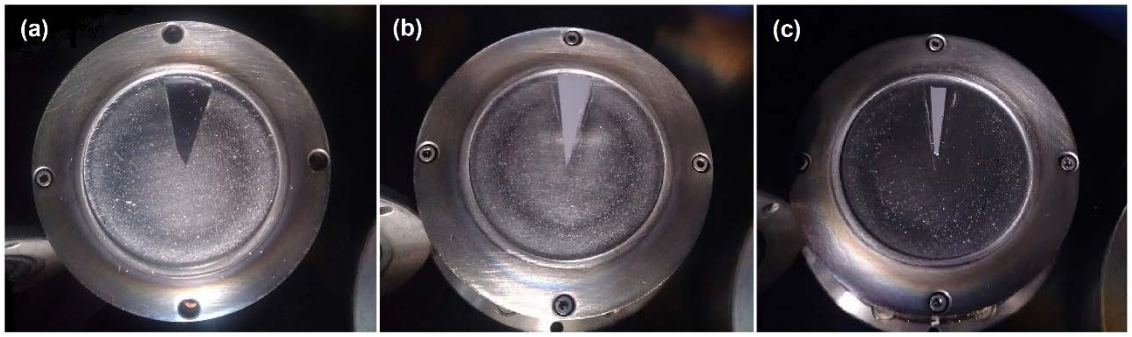

Figure 2-3. Silicon chips assembled on the surface of the hafnium target. a) %10 mole ratio of Si, b) 8% mole ratio of Si and c) 6% ratio of Si.

Multi-target sputtering system Orion-8 (AJA International Co.) was used for sputter deposition of silicon doped hafnium dioxide films. Chamber was pumped down to better than 5.0×10^{-8} Torr before introducing mixture of argon and nitrogen. Ti and Si:Hf targets were sputter cleaned for 10 minutes before insertion of the substrates into the deposition chamber. Substrates were heated to 300ºC for 5 minutes prior to deposition in order to acquire a uniform temperature on the entire wafer.

Hafnium oxide film was reactively sputter coated. Partial pressure of oxygen for hafnium oxide films was optimized to be about %10 of the total deposition pressure. Ultra-high pure (UHP) argon with 18 standard cubic centimeter per minute (sccm) flow rate was mixed with 2 sccm of UHP oxygen and introduced to the chamber and deposition pressure was set to be 3 mTorr. RF power of 150 W was used for deposition and substrate temperature was kept at 300ºC. Thin layer of TiN (about 20nm) was reactively sputter coated on top of doped hafnium oxide layer to serve as capping layer. Nitrogen partial pressure for TiN layer was optimized at %5 with 17.1 sccm of UHP argon gas flow and 0.9 sccm of UHP nitrogen. Deposition was carried out at the pressure of 2 mTorr using RF power of 150 W. Substrate was rotated during all depositions and kept at 300ºC to

ensure the uniformity of the films. Deposition rates for TiN and doped HfO_2 layer were calculated to be 20 Å/min for TiN and 63 Å/min for doped HfO_2.

2.2.2 Rapid Thermal Annealing

Films with capping TiN layers were annealed at 600ºC, 800ºC and 1000ºC for 20 seconds using a rapid thermal annealing (RTA) system (ULVAC-RIKO, model MILA-5000) under nitrogen flow. Samples were placed on a quartz holder next to a thermocouple and heating was supplied by four halogen lamps covering the sample from four directions. Annealing procedure was specified with three step programs and the diagram depicted in Figure 2-4 shows the annealing steps. After the third step (about three minutes), the RTA system was shut down and samples cooled down to 50 ºC in nitrogen ambient before taking them out of the furnace.

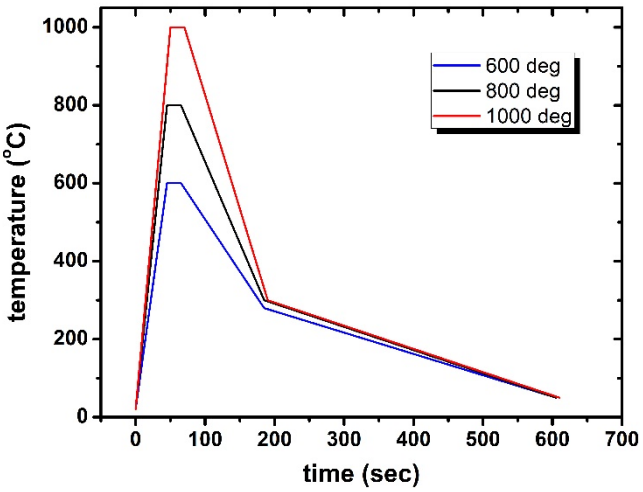

Figure 2-4. Rapid thermal annealing diagram. Samples were held at desired temperature for 20 seconds. Furnace was shut down after samples cooled down to about 300ºC (end of third step).

2.2.3 Electrode Preparation for Hysteresis Measurement

For the ferroelectric hysteresis measurements, gold electrodes were fabricated via photolithography and wet etching techniques. Thin film of gold with 30 nm thickness was deposited with electron beam evaporation system (AJA international) on top of TiN layer. Evaporation chamber was pumped down to better than 10^{-8} Torr and gold chunk was placed in a glassy-carbon crucible. Substrate was held at room temperature and deposition rate was adjusted to about 0.5 Å/sec. S1813 microposit photoresist (from Shipley) was spin coated (Brewer Science Spin Coater, model 200CB) at the speed of 4000rpm for 90 seconds. The photoresist was soft-baked at 110 ºC for 75 seconds and then exposed to UV (Newport Inc.) for three minutes under the mask with an array of 50µm×50µm squares separated with 20 µm space. After UV treatment, films were hard-baked for two more minutes at 110 ºC and then developed at MF-319 developer (Shipley) for 60 seconds. Final product were rinsed with distilled water and dried with nitrogen.

In order to etch away gold from undesired locations, an etchant with the following recipe was made: 30 gr of potassium iodide (KI) was dissolved in 30 ml of de-ionized water and then 300 milligrams of iodic acid (HIO_3) was added to increase iodine in the solution. Wafers then dipped in this solution for 30 seconds at room temperature and then rinsed and dried.

Following gold etching, TiN layer was selectively etched with a diluted standard clean (SC-1) solution with the following ingredients:

NH_4OH (50 vol. %): 1 part

H_2O_2 (30%): 1 part

H_2O: 10 part

The wafers were dipped in the etchant at 40 ºC for 60 seconds and then rinsed with DI-water and blow dried with nitrogen. Figure 2-5 is a step by step demonstration of the patterning and optical image of the final 50 µm×50 µm gold square electrodes.

Another piece from each sample was selectively etched to remove TiN without any pattern in order to record piezoresponse force microscopy (PFM) image from the surface and test the polarization switching of the domains.

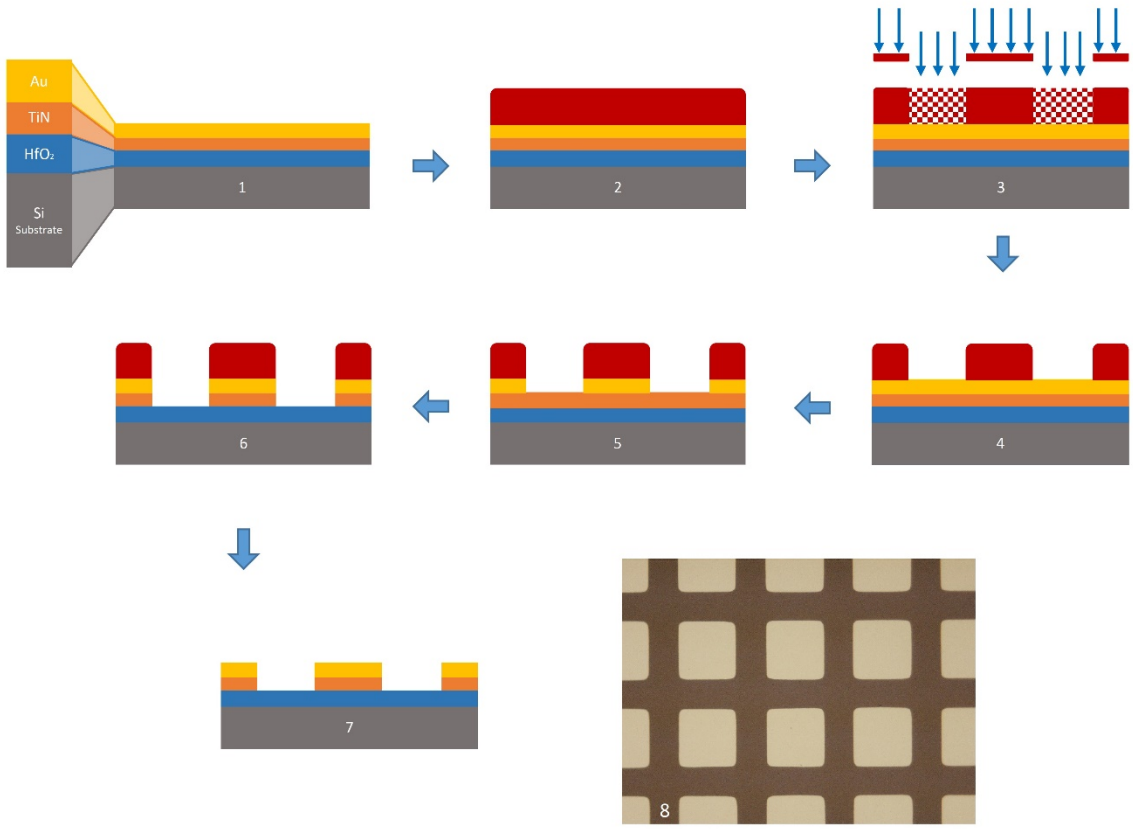

Figure 2-5. Schematic demonstration of the patterning and fabrication steps of the gold micro-square electrodes; 1) initial multilayered structure, 2) coating photoresist and soft-bake, 3) UV exposure with mask and hard-bake, 4) photoresist development, 5) gold layer etching, 6) TiN layer etching, 7) stripping the remaining photoresist, 8) top view optical image of the final pattern.

2.2.4 Characterization Methods

2.2.4.1 Film Thickness

Reflectometry and scanning probe microscopy techniques were used for thin film thickness measurements. Reflectometry method is based on the fact that light refracts at the interface of two material (e.g. film with air and film with substrate). So, reflected light will have information regarding the thickness and type of material. This method uses a wide spectrum in visible range and can be used for multilayer structures by considering refraction index (n) and absorption coefficient (k) of the films and estimates the thickness of films. For our samples, film, thickness of deposited films were calibrated individually using reflectometry method (Filmetrics, model F20). This instrument produces light at the range of 400-1100 nm wavelength and its measurement range is between 15nm up to 40 µm. So, for more accuracy, the measurements were carried out on thicker films of Si:HfO_2 (about 200nm) and TiN (about 60nm) and deposition rate were calculated and optimized for desired lower thicknesses.

Thickness of the films later confirmed using scanning probe microscopy (Asylum Research, MFP-3D) technique which operates based on scanning the surface with a stylus tip and measures the roughness by recording the vertical movement of the tip. For this purpose, sharp steps were created on the films and the height of the step were considered as the thickness of the film.

2.2.4.2 Elemental Analysis

X-ray photoelectron spectroscopy (XPS) is used for elemental analysis. The working principle is based on the excitation of electrons in the atomic orbitals using X-ray source. Generally, Kα X-rays from Mg (with energy 1254 eV) and Al (with energy 1487 eV) are used for excitation and energy of the electron emitting from different orbitals

are recorded. For our samples, in order to determine the Si/Hf mole ratio, a thicker film of doped hafnia was deposited at the same conditions on a sapphire substrate and XPS measurements were carried out on a VG Scientific MKII system with an Al Kα anode as the excitation source (hν=1486.6 eV). Obtained peaks via XPS were fitted with a custom VBA program in Microsoft Excel using Voigt profiles together with a Shirley background function.

2.2.4.3 Crystalline Structure

Crystalline structure of the films were examined using X-ray diffraction (XRD) method (Panalytical X'Pert, PW3040-PRO, Cu Kα radiation source) in a regular θ-2θ configuration. X'Pert High Score analysis software was used for identification of peaks and crystal. The background of the spectrum were subtracted for better comparison and better visibility of small peaks.

2.2.4.4 Ferroelectricity and Hysteresis

For the analysis of ferroelectric thin films, domain phase and displacement of the film surface and polarization change versus applied electric filed (P-E) are measured using piezoforce microscopy (PFM) technique. PFM is a scanning probe microscopy (SPM) technique which records the vertical movements or change in resonant frequency of the tip that results from variation of electrical forces on the surface.

Ferroelectrics as defined are the materials that can hold permanent polarization. The polarization in a single domain is unidirectional, however when ferroelectric is not polarized, each domain aligns in a random direction resulting in a zero net polarization. When PFM tip scans the surface, it forms a capacitor like structure with the surface. Due to random polarization of the domains in the surface, the electric field on the surface of each domain varies. So, their capacitance with PFM tip varies which results in attractive or repulsive force. The magnitude of change is interpreted as polarization direction and

magnitude in the domain and so on. This method can also be used for applying electric fields in order to change the direction of the domains besides recording it. Applying enough voltage to the tip causes the domains to align in the direction of the applied electric filed and test the polarizability of the sample.

Polarization versus applied electric field (P-E) is generally performed in a cyclic form, meaning that voltage is applied to the sample in the form of a wave (Figure 2-6) which starts from a value (e.g. 0 V) and increases to a maximum value that ensures full polarization of the sample and then decreases to the maximum negative value and finally ends at zero again. This may be repeated several times since the first cycle is generally does not represent the full hysteresis loop (as in Figure 1-6).

For the films in this study, dual AC resonance-tracking piezoresponse force microscopy (DART-PFM) technique was used which is more accurate than PFM. The instrument was an Asylum Research brand (Model MFP-3D) and the tip that was used for the measurements was a conductive silicon cantilever with titanium/platinum coating (OMCL-AC240TM-R3, the resonant frequency of 70 kHz and spring constant~2 N/m).

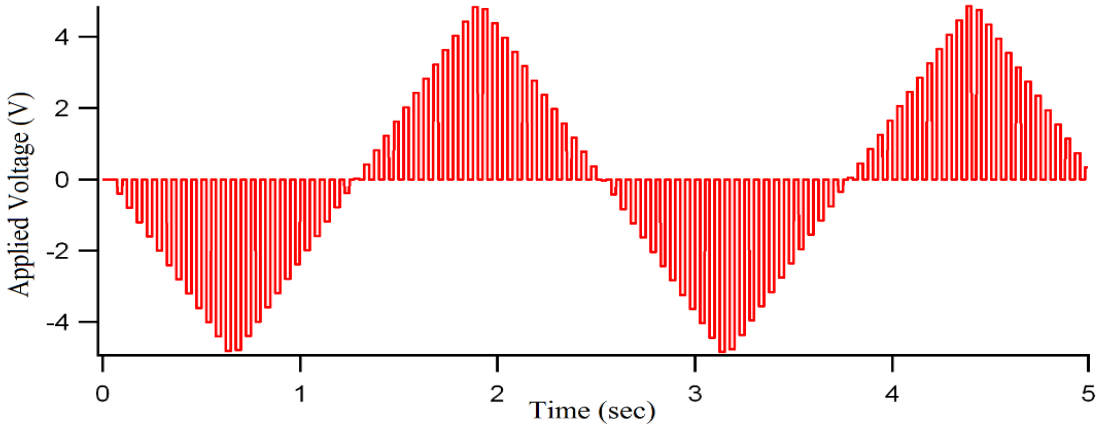

Figure 2-6. The waveform that is used for (P-E) hysteresis measurement.

2.3 Results and Discussion

2.3.1 XPS Results

Figure 2-6 shows the XPS results for the three groups of the samples. The thickness of the deposited films was about 200 nm and the substrate was chosen as alumina instead of silicon. The Si/Hf ratio for these groups were 6, 8 and 10 percent.

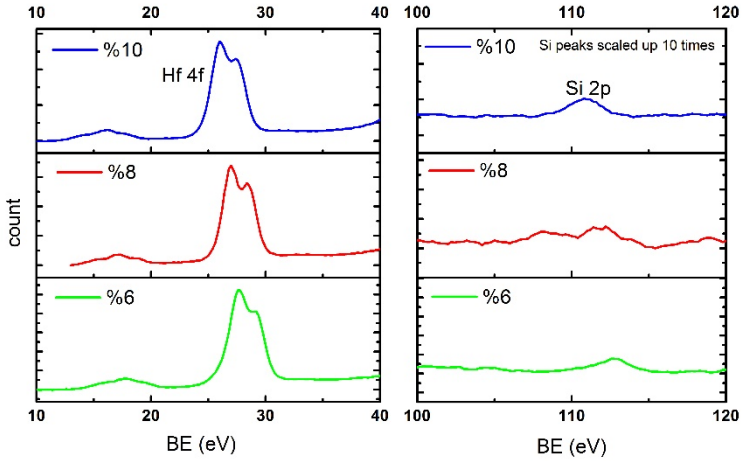

Figure 2-7. Obtained peaks via XPS were fitted with a custom VBA program in Microsoft Excel using Voigt profiles together with a Shirley background function.

2.3.2 Phase Evolution

Tracking the crystal structure of the films in the samples with 6% silicon dopant and 10nm thickness which were annealed at 800°C, confirmed the phase transition from monoclinic to orthorhombic. Samples right after deposition at 300°C, did not show any ferroelectricity, however, small peaks were shown up at XRD spectrum suggesting limited crystallization (Figure 2-8a). After annealing the samples at 800°C, the peak at θ~30° which is aligned with orthorhombic and tetragonal peaks started growing and other peaks

were also intensified showing improvement in crystallinity. The ferroelectricity analysis in these films affirmed that the film contains a polar phase which can be counted as the source of ferroelectricity. Figure 2-8 depicts the diffraction spectra of this ferroelectric film before and after annealing (Figs. 2-8(a) and 2-8(b), respectively) and compares them with a spectrum of the film without dopant (Fig 2-8(c)) that has the same thickness as the ferroelectric film (10nm) and was produced in the same deposition and annealing conditions. It is clear that the formation of tetragonal and orthorhombic phases strongly relates to the dopant. The peak at θ~43° belongs to cubic TiN films that generally grow above 400°C[49].

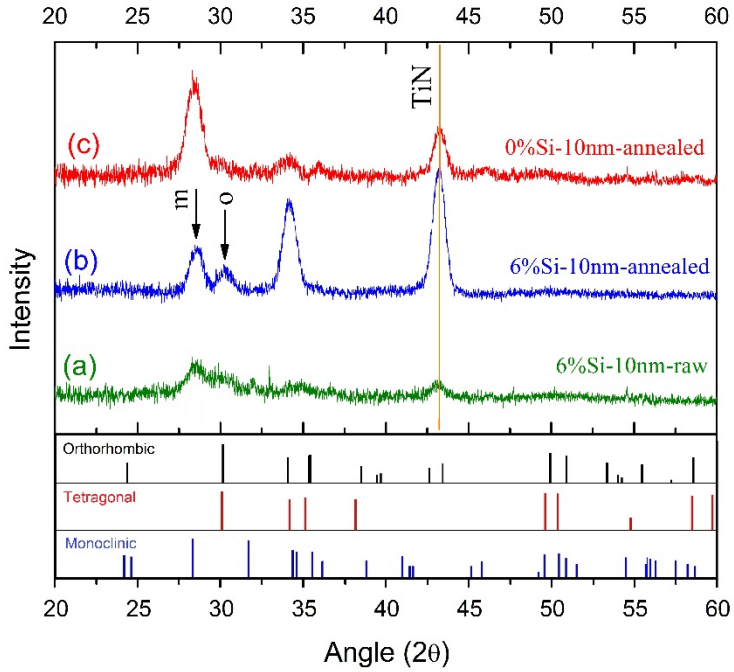

Figure 2-8. XRD patterns of the samples with 10nm thickness. (a) and (b) refer respectively to the as grown(raw) and annealed film with 6% silicon dopant. Growth of the peak at 30° is the sign of the orthorhombic phase growth. (c) represents the annealed sample without silicon dopant. Distinct peak that is used to distinguish monoclinic phase and orthorhombic phase is the peak at around 30°.

Figure 2-9 presents the diffraction patterns of the films doped with the same doping level (6% silicon) but with different thicknesses: 10, 15, 20nm and 200nm. The results showed that increasing the thickness of the film suppresses the formation of the orthorhombic phase. Monoclinic phase becomes the dominant phase when the thickness of the film passes 20nm.

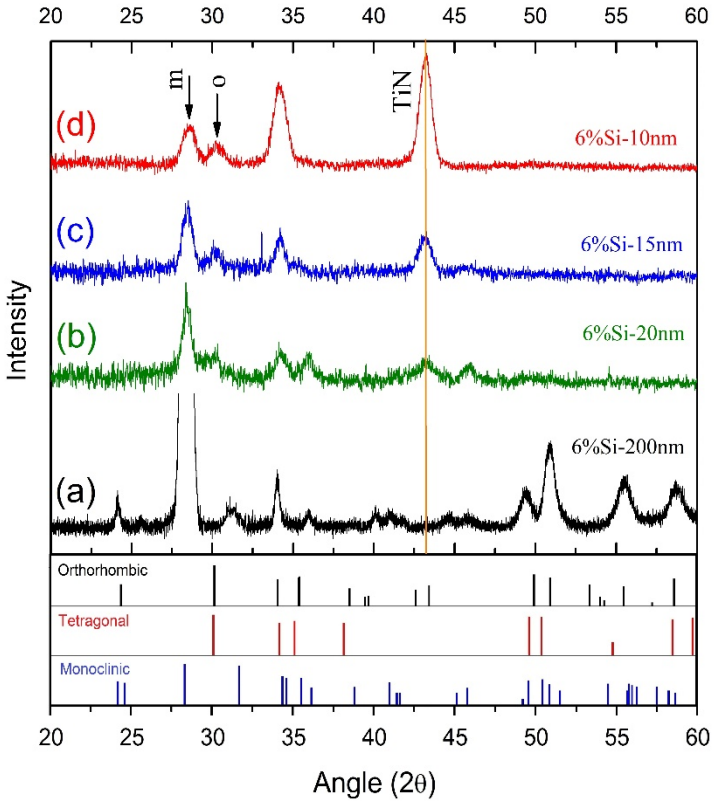

Figure 2-9. XRD patterns of the samples with 6% silicon dopant but different thicknesses: film with 200nm thickness (a), 20nm (b), 15nm(c) and 10nm (d). Only monoclinic phase remains when thickness of the film increases and the film with 200nm thickness proves this. The decrease at the intensity ratio of the peak at 30º (orthorhombic) to the peak at 28º (monoclinic) is the sign of phase conversion from orthorhombic to the monoclinic with further increase in the thickness of the film.

2.3.3 Piezoresponse Force Microscopy of doped HfO_2 Thin Films

Polarization switching of the domains of the film by the means of dual AC resonance-tracking piezoresponse force microscopy (DART-PFM) technique was used to examine local ferroelectric properties of the film. For this purpose, top TiN layer was selectively etched with a diluted standard clean (SC-1) solution (NH_4OH (50 vol. %):H_2O_2 (30 %):H_2O~1:1:10) at 40°C to expose doped hafnia film. The measurements were carried out using a conductive silicon cantilever with titanium/platinum coating (OMCL-AC240TM-R3, the resonant frequency of 70 kHz and spring constant~2N/m). PFM lithography technique was used to write two nested squares with the sizes of 10 µm and 5 µm (shown in Figure 2-10a) by applying the voltage to the conductive cantilever. The larger square was written by −5 V and inner square with +5 V applied to the tip while the sample was grounded. Figure 2-10a shows the phase image of the pattern obtained by PFM after lithography and dashed squares correspond to the locations of the oppositely polarized regions. Figure 2-10b is the corresponding amplitude image from the same area as in Figure 2-10a. Both of these images confirm the ferroelectric properties and domain switching in the film by applying electric fields.

Macroscopic ferroelectric properties were assessed via ferroelectric hysteresis measurements using the square gold electrodes that were produced via electron beam evaporation on top of TiN layer.

Hysteretic behavior of the film under applied electric field is shown in Figure 2-10c and Figure 2-10d. Figure 2-10c represents the phase change versus applied voltage. Phase change close to 180 degrees was observed when the voltage of the tip changed from −5 V to +5 V. Figure 2-10d shows the displacement of the film surface with applied voltage. As expected, the displacement diagram has a butterfly-shaped hysteresis. The piezoresponse mapping and hysteresis measurements together satisfy the ferroelectricity

criteria and rule out the possibility of the hysteresis effect due to the charge trapping phenomenon.[50]

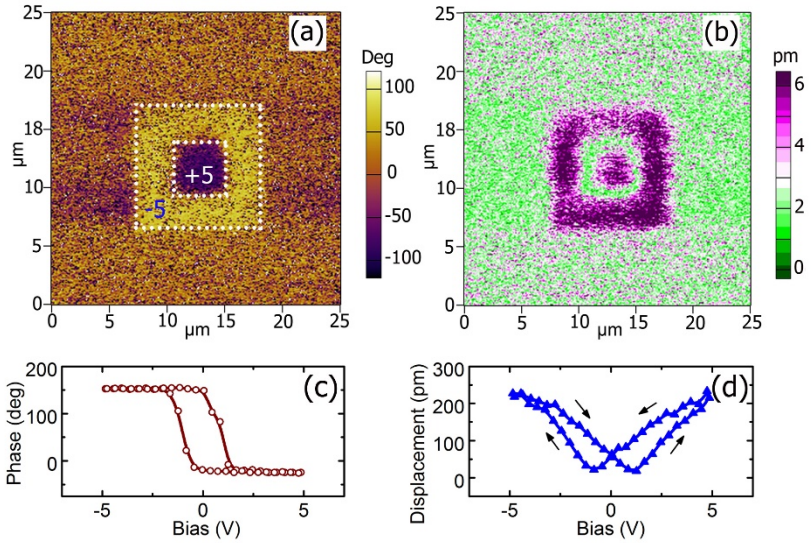

Figure 2-10. Piezoresponse force microscopy (PFM) of the TiN-etched surface of the Si:HfO_2 film: (a) phase image of the poled surface with corresponding poling pattern, larger dashed square was poled with -5V bias and smaller square was poled with +5V; (b) corresponding amplitude image for the same area; (c) and (d) represent phase and displacement hysteresis graphs obtained from the top of the gold square electrodes.

2.4 Conclusion

In summary, ferroelectric films of silicon doped hafnia were successfully fabricated using reactive RF sputtering technique. Samples with 6 mol. % of silicon dopant that were capped with TiN layer while annealed at 800°C showed clear ferroelectric properties as verified by domain switching using PFM methods and hysteresis measurement techniques.

Phase change from monoclinic to orthorhombic in ferroelectric samples were observed. The increase in thickness of the film decreased the orthorhombic to monoclinic

phase ratio demonstrating the polar-orthorhombic phase is only stable at lower thicknesses (below 20 nm).

Films doped with higher levels of dopant (8 mol. % and 10 mol. %) and those without capping layer did not show a stable ferroelectric effect.

Films that were annealed at 600°C did not show ferroelectricity. Low annealing temperature was insufficient for the creation of orthorhombic phase. Also, the experiments showed that samples that were annealed at 1000°C were affected by the etchants resulting in the destruction of the films during etch process.

References

1. Scott, J. F. Ferroelectric Memories Today. *Ferroelectrics* **236,** 247–258 (2000).
2. Warusawithana, M. P. *et al.* A ferroelectric oxide made directly on silicon. *Science* **324,** 367–370 (2009).
3. Dubourdieu, C. *et al.* Switching of ferroelectric polarization in epitaxial BaTiO3 films on silicon without a conducting bottom electrode. *Nat. Nanotechnol.* **8,** 748–54 (2013).
4. Xiong, S.-B. & Sakai, S. Memory properties of $SrBi_2Ta_2$ thin films prapared on SiO_2/Si substrates. *Appl. Phys. Lett.* **75,** 1613 (1999).
5. Kim, D. J. *et al.* Polarization relaxation induced by a depolarization field in ultrathin ferroelectric $BaTiO_3$ capacitors. *Phys. Rev. Lett.* **95,** 237602 (2005).
6. Suzuki, M. & Ami, T. A proposal of epitaxial oxide thin film structures for future oxide electronics. *Mater. Sci. Eng. B* **41,** 166–173 (1996).
7. Park, M. H. *et al.* Ferroelectricity and Antiferroelectricity of Doped Thin HfO_2-Based Films. *Adv. Mater.* **27,** 1811–1831 (2015).
8. Robertson, J. High dielectric constant gate oxides for metal oxide Si transistors. *Reports Prog. Phys.* **69,** 327–396 (2006).
9. Wilk, G. D., Wallace, R. M. & Anthony, J. M. High-κ gate dielectrics: Current status and materials properties considerations. *J. Appl. Phys.* **89,** 5243–5275 (2001).
10. Mikolajick, T. *et al.* FeRAM technology for high density applications. *Microelectron. Reliab.* **41,** 947–950 (2001).
11. Ishiwara, H. Impurity substitution effects in $BiFeO_3$ thin films—From a viewpoint of FeRAM applications. *Curr. Appl. Phys.* **12,** 603–611 (2012).
12. Zhang, M. M., Jia, Z. & Ren, T. L. Effects of electrodes on the properties of sol-gel PZT based capacitors in FeRAM. *Solid. State. Electron.* **53,** 473–477 (2009).
13. Lim, S. H., Rastogi, A. C. & Desu, S. B. Electrical properties of metal-ferroelectric-insulator-semiconductor structures based on ferroelectric polyvinylidene fluoride copolymer film gate for nonvolatile random access memory application. *J. Appl. Phys.* **96,** 5673–5682 (2004).
14. Mueller, S. *et al.* Correlation between the macroscopic ferroelectric material properties of Si:HfO_2 and the statistics of 28 nm FeFET memory arrays. *Ferroelectrics* **497,** 42–51 (2016).
15. Böscke, T. S., Müller, J., Bräuhaus, D., Schröder, U. & Böttger, U. Ferroelectricity in hafnium oxide thin films. *Appl. Phys. Lett.* **99,** 102903 (2011).
16. Müller, J. *et al.* Ferroelectric $Zr_{0.5}Hf_{0.5}O_2$ thin films for nonvolatile memory applications. *Appl. Phys. Lett.* **99,** 112901 (2011).
17. Mueller, S. *et al.* Incipient Ferroelectricity in Al-Doped HfO_2 Thin Films. *Adv. Funct. Mater.* **22,** 2412–2417 (2012).
18. Müller, J. *et al.* Ferroelectricity in yttrium-doped hafnium oxide. *J. Appl. Phys.* **110,** 114113 (2011).
19. Hubbard, K. J. & Schlom, D. G. Thermodynamic stability of binary oxides in contact with silicon. *J. Mater. Res.* **11,** 2757–2776 (1996).
20. Yurchuk, E. *et al.* Impact of layer thickness on the ferroelectric behaviour of silicon doped hafnium oxide thin films. *Thin Solid Films* **533,** 88–92 (2013).
21. Martin, D. *et al.* Downscaling ferroelectric field effect transistors by using ferroelectric Si-doped HfO_2. *Solid. State. Electron.* **88,** 65–68 (2013).
22. Böscke, T. S. *et al.* Phase transitions in ferroelectric silicon doped hafnium oxide. *Appl. Phys. Lett.* **99,** 79–82 (2011).

23. Schroeder, U. *et al.* Impact of different dopants on the switching properties of ferroelectric hafniumoxide Impact of different dopants on the switching properties of ferroelectric hafniumoxide. *Jpn. J. Appl. Phys.* **53,** 08LE02 (2014).
24. Cantas, A., Aygun, G. & Basa, D. K. In-situ spectroscopic ellipsometry and structural study of HfO2 thin films deposited by radio frequency magnetron sputtering. *J. Appl. Phys.* **116,** (2014).
25. Wang, J., Li, H. P. & Stevens, R. Hafnia and hafnia-toughened ceramics. *J. Mater. Sci.* **27,** 5397–5430 (1992).
26. Huan, T. D., Sharma, V., Rossetti, G. A. & Ramprasad, R. Pathways Towards Ferroelectricity in Hafnia. *Phys. Rev. B* **90,** 64111 (2014).
27. Garvie, R. C. The Occurrence of Metastable Tetragonal Zirconia as a Crystallite Size Effect. *J. Phys. Chem.* **69,** 1238–1243 (1965).
28. Triyoso, D. H., Tobin, P. J., White, B. E., Gregory, R. & Wang, X. D. Impact of film properties of atomic layer deposited HfO_2 resulting from annealing with a TiN capping layer. *Appl. Phys. Lett.* **89,** 132903 (2006).
29. Tomida, K., Kita, K. & Toriumi, A. Dielectric constant enhancement due to Si incorporation into HfO2. *Appl. Phys. Lett.* **89,** 142902 (2006).
30. Lines, M. E. & Glass, A. M. *Principles and Applications of Ferroelectrics and Related Materials.* (Oxford University Press, 2001).
31. Kisi, E. H. Influence of Hydrostatic Pressure on the t→o Transformation in Mg-PSZ Studied by In Situ Neutron Diffraction. *J. Am. Ceram. Soc.* **81,** 741–745 (1998).
32. Marshall, D. B., Jarnes, M. R. & Porter, J. R. Structural and Mechanical Property Changes in Toughened Magnesia-Partially-Stabilized Zirconia at Low Temperatures. *J. Am. Ceram. Soc.* **72,** 218–227 (1989).
33. Kisi, E. H. & Howard, C. J. Crystal Structures of Zirconia Phases and their Inter-Relation. *Key Eng. Mater.* **153–154,** 1–36 (1998).
34. Lehan, J. P., Mao, Y., Bovard, B. G. & Macleod, H. A. Optical and Microstructural Properties of Hafnium Dioxide Thin Films. *Thin Solid Films* **203,** 227–250 (1991).
35. Müller, J., Polakowski, P., Mueller, S. & Mikolajick, T. Ferroelectric Hafnium Oxide Based Materials and Devices: Assessment of Current Status and Future Prospects. *ECS J. Solid State Sci. Technol.* **4,** N30 (2015).
36. Callegari, A., Cartier, E., Gribelyuk, M., Okorn-Schmidt, H. F. & Zabel, T. Physical and electrical characterization of Hafnium oxide and Hafnium silicate sputtered films. *J. Appl. Phys.* **90,** 6466–6475 (2001).
37. Al-Kuhaili, M. F. Optical properties of hafnium oxide thin films and their application in energy-efficient windows. *Opt. Mater. (Amst).* **27,** 383–387 (2004).
38. Park, J.-W., Lee, D.-K., Lim, D., Lee, H. & Choi, S.-H. Optical properties of thermally annealed hafnium oxide and their correlation with structural change. *J. Appl. Phys.* **104,** 33521 (2008).
39. Khoshman, J. M., Khan, A. & Kordesch, M. E. Amorphous hafnium oxide thin films for antireflection optical coatings. *Surf. Coatings Technol.* **202,** 2500–2502 (2008).
40. Franta, D. *et al.* Optical characterization of HfO_2 thin films. *Thin Solid Films* **519,** 6085–6091 (2011).
41. Khoshman, J. M. & Kordesch, M. E. Optical properties of a-HfO_2 thin films. *Surf. Coatings Technol.* **201,** 3530–3535 (2006).
42. Bright, T. J., Watjen, J. I., Zhang, Z. M., Muratore, C. & Voevodin, A. A. Optical properties of HfO2 thin films deposited by magnetron sputtering: From the visible to the far-infrared. *Thin Solid*

Films **520,** 6793–6802 (2012).

43. Triyoso, D. *et al.* Impact of Deposition and Annealing Temperature on Material and Electrical Characteristics of ALD HfO_2. *J. Electrochem. Soc.* **151,** F220–F227 (2004).
44. Senzaki, Y., Park, S., Chatham, H., Bartholomew, L. & Nieveen, W. Atomic layer deposition of hafnium oxide and hafnium silicate thin films using liquid precursors and ozone. *J. Vac. Sci. Technol. A Vacuum, Surfaces, Film.* **22,** 1175–1181 (2004).
45. Kukli, K. *et al.* Influence of thickness and growth temperature on the properties of zirconium oxide films grown by atomic layer deposition on silicon. *Thin Solid Films* **410,** 53–60 (2002).
46. Kim, H., McIntyre, P. C. & Saraswat, K. C. Effects of crystallization on the electrical properties of ultrathin HfO_2 dielectrics grown by atomic layer deposition. *Appl. Phys. Lett.* **82,** 106–108 (2003).
47. Kim, H., Saraswat, K. C. & McIntyre, P. C. Comparative Study on Electrical and Microstructural Characteristics of ZrO_2 and HfO_2 Grown by Atomic Layer Deposition. *J. Mater. Res.* **20,** 3125–3132 (2005).
48. Triyoso, D. H., Hegde, R. I., White, B. E. & Tobin, P. J. Physical and electrical characteristics of atomic-layer-deposited hafnium dioxide formed using hafnium tetrachloride and tetrakis(ethylmethylaminohafnium). *J. Appl. Phys.* **97,** (2005).
49. Vasu, K., Krishna, M. G. & Padmanabhan, K. A. Substrate-temperature dependent structure and composition variations in RF magnetron sputtered titanium nitride thin films. *Appl. Surf. Sci.* **257,** 3069–3074 (2011).
50. Pintilie, L. & Alexe, M. Ferroelectric-like hysteresis loop in nonferroelectric systems. *Appl. Phys. Lett.* **87,** 112903 (2005).

Chapter 3:

Polarization- Dependent Photovoltaic Effect in Ferroelectric-Semiconductor System

3.1 Introduction

3.1.1 Photovoltaic Ferroelectrics

Photovoltaic phenomenon involves three main processes: light absorption, generation of the electron-hole pairs and separation of the free charges. A suitable semiconductor material with an energy gap in the range of visible light can accomplish the first two steps; however, for the separation of the carriers, more than just a semiconductor medium is required. Conventional solar cells utilize the built-in electric field at the interface of two doped semiconductors (p-n junction) to efficiently separate electrons and holes. This electric field is limited by the energy bandgap and alignment of the energy levels of the two joining semiconductors.[1] Additionally, in the junction-based structure, materials' choice is limited due to doping and lattice mismatch issues.[2] To overcome these limits, a new and less explored approach involving ferroelectric materials has been recently gaining attention. Polarization field in ferroelectrics which can be much larger than the built-in electric fields in the depletion layer of a semiconductor p-n junction can efficiently separate electron-hole pairs.[2–4] Research on photoconductivity in ferroelectrics started four decades ago on famous ferroelectrics such as $BaTiO_3$[5], $LiNbO_3$[5–7] and $Pb(Zr,Ti)O_3$;[8] however, due to their large band gaps (between 3 and 4 eV), the efficiencies were limited by small current densities negating the effect of their large open circuit photovoltages. In the recent years, the discovery of photoconductivity in

smaller band gap ferroelectrics such as $BiFeO_3$ (Refs. 9–11) ($E_g \sim 2.67$ eV (Ref. 11)) has given new promises for the higher efficiency in ferroelectric solar cells.

3.1.2 Design Background (Previous Efforts)

Various efforts have been taken to realize charge separation in solar cells based on ferroelectric materials. In simplest designs, besides the separation of charges, a ferroelectric layer sandwiched between two electrodes[12–14] acts also as the source of electron-hole pairs (Figure 3-1a). It has been shown that in these cells, above band gap photo-induced voltages can be observed only when the current flows perpendicular to the domain walls of the ferroelectric; otherwise, the response to the light is limited to photoconductivity of the ferroelectric material.[14] In these cells, however, the efficiency is still more than an order of magnitude smaller than those of commercial cells, mainly because of low quantum efficiency, large band gap and high resistivity of the ferroelectrics.[4,15,16]

An alternative approach is to incorporate low bandgap semiconductors inside ferroelectric matrix to improve quantum efficiency (Figure 3-1b). The drawback of this design is the trapping states that are introduced into the band gap.[17,18] In another design, Liu et al.[2] utilized polarization field from ferroelectric layer to create positive and negative bound charge sites on the surface of the adjacent semiconductor to separate electron-hole pairs and drive them along the surface of the semiconductor. In their design of solar cell, the free charges generated inside the semiconductor were collected on electrode without entering the ferroelectric medium (Figure 3-1c). Therefore, their concept cannot be easily implemented to improve conventional p-n junction solar cells. In our design (Figure 3-1d), the charges photogenerated in the semiconductor traverse ferroelectric layer. This makes it possible to integrate the ferroelectric layer with p-n junction based solar cells.

Organic photovoltaics have also benefitted from ferroelectric polymers such as P(VDF-TrFE).[19,20] The polarization field from ferroelectric layer seems to obviate the need for an external bias and enhances the charge separation, although the ferroelectric polymer needs to be very thin (less than 10 nm) in order to facilitate tunneling of the charge carriers.[20] In our approach, the polarization field from a very thin inorganic ferroelectric film of doped hafnium dioxide (~10 nm) is used to separate free charge careers produced inside the semiconductor, and low thickness of the film allows the careers to tunnel across the ferroelectric film. This method can be potentially exploited to enhance the efficiency of p-n junction solar cells by enhancing the electric field in the vicinity of the depletion zone.

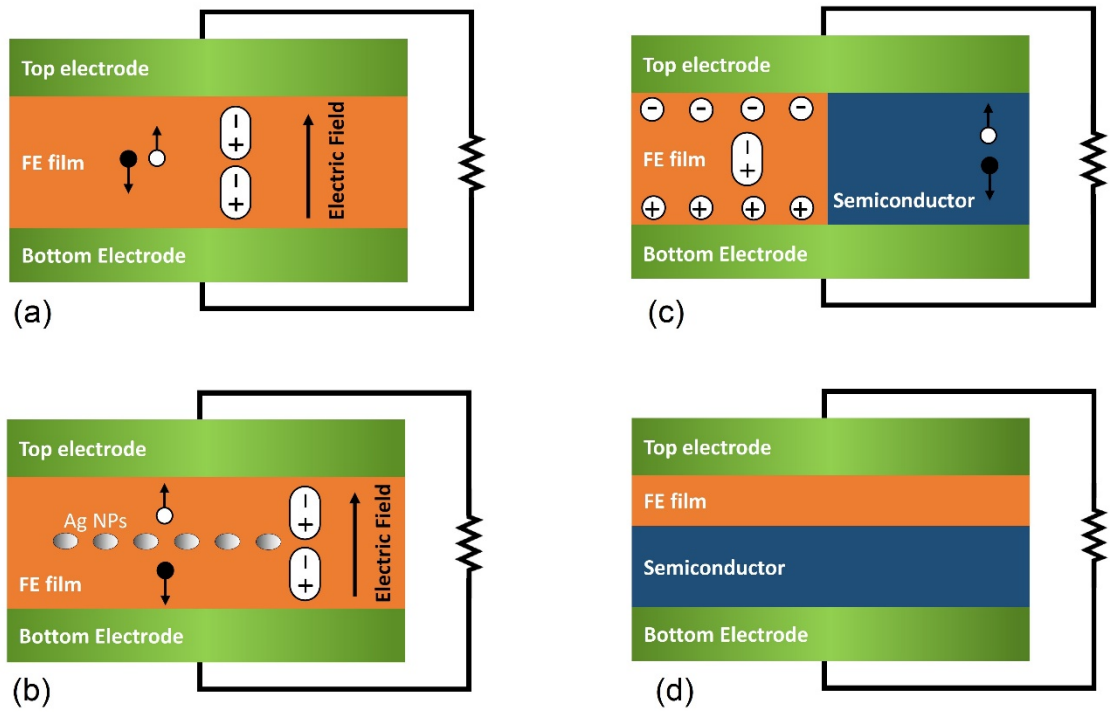

Figure 3-1. Schematic of different proposed designs for utilization of ferroelectric materials for photovoltaic applications: adapted from Ref. 13 (a), Ref. 17 (b), Ref. 2 (c) and the design for the sample in this work (d)

3.1.3 Ferroelectricity in Hafnium Dioxide Thin Films

As discussed in the previous chapter, ferroelectricity has recently been reported in hafnium dioxide (HfO_2) thin films doped with Si[21] and other elements.[22,23] A variety of methods such as ion-assisted deposition (IAD),[24] metal organic atomic layer deposition (MOALD)[21] and atomic layer deposition (ALD)[25] were suggested and utilized to prepare ferroelectric HfO_2 thin films. We utilized RF sputtering technique to fabricate ferroelectric hafnia and optimized the conditions based on the varying the thickness of the film, doping level, annealing temperature, and deposition conditions. The results showed that the films with 6 mol. % of silicon doping level and thickness of 10 nm that were deposited at 300°C, capped with a thin layer of TiN and annealed at 800°C had the best ferroelectric performance.

The benefit of ferroelectric hafnia is that it holds its ferroelectric properties at very low thicknesses (~ 10nm). Incorporation of this thin film would allow tunneling across the film in a lamellar cell structure and the polarization field from the film can be used to separate free charge careers. This method can be potentially exploited to increase the efficiency of p-n junction solar cells by enhancing the electric field in the vicinity of the depletion zone.

3.2 Experimental

3.2.1 Sample Preparation

Thin films of hafnium dioxide with variable thickness and dopant level were prepared via RF sputtering method as described in chapter 2. Films with 10 nm thickness and 6 mol. % silicon dopant that were annealed at 800°C for 20 seconds showed the best

ferroelectric properties and could be poled with AFM tip or by applying an external electric field.

Three sets from this sample were cut and the TiN layer was removed from the top of them to expose hafnium dioxide layer for further characterization. Bare surface of hafnium dioxide was used for surface potential measurements using Kelvin probe force microscopy (KPFM) and samples with gold coat on top of them as electrode were used for I-V measurements. Two sets of the films out of three were poled in opposite directions under an intense electric field and the third one kept intact (unpoled) in order to investigate the effect of polarization on KPFM and I-V results.

3.2.2 Etching

As mentioned earlier, in order to analyze surface potential variation on the surface of the hafnium dioxide films, TiN capping layer from the top of the ferroelectric hafnia was etched away using a diluted standard clean-1 (SC-1) solution with the following ratios:

NH_4OH (50 vol. %): 1 part

H_2O_2 (30%): 1 part

H_2O: 10 part

The etching process was carried out in a glass dish on a hot plate which provided the desired etching temperature of 40°C. The etch rate of TiN layer in the above solution was measured to be 40 nm/min at these conditions. This solution was also tested on hafnia film to investigate its possible destructive effects and the results showed that this etchant is safe for hafnium dioxide films.

3.2.3 Electrode preparation and I-V measurement

For I-V measurements hafnium dioxide films were coated with a semi-transparent gold layer to serve as the top electrode. 5 nm of gold was deposited through a mask with $5mm^2$ opening area via an electron beam evaporation system (AJA international) at room temperature. Vacuum level in the deposition chamber before the deposition was better than 10^{-8} Torr and a glassy carbon crucible was used for gold deposition target. The sample was rotated during deposition to ensure the uniformity and deposition rate was adjusted to about 0.2 Å/sec. The bottom side of the structure (silicon side) was coated with silver to serve as the bottom electrode.

Current-voltage (I-V) curves were recorded using picoammeter (Keithley 2614B Sourcemeter unit) while cells were exposed to simulated AM1.5 spectrum from a sun light simulator. The voltage was scanned between −1 V and +1 V for 400 data points, and the current was recorded.

3.2.4 Poling

In order to investigate the possibility of ferroelectric HfO_2 films to be incorporated into the structure of photovoltaic cells, first, we need to polarize the films so we can employ that polarization field for the separation of the carriers. To this end, three pieces from the same ferroelectric sample (10 nm thick, 6 mol. % Si) were cut and two of them were exposed to a high electric field at room temperature. These two pieces were poled in opposite directions using the poling setup that is schematically depicted in Figure 3-2. The samples were placed between two 0.1 mm thick glass slides, separating them from electrodes. The glass slides were used to prevent damage to the samples that could be due to possible arcing between the electrodes. The voltage of 5 kV was applied between

electrodes while the separation of the electrodes was about 1 mm. The poling direction was defined as positive for the sample with the substrate (Si) at the negative electrode (anode) side and HfO_2 film close to the positive electrode (cathode) leading to an upward (from the substrate to the film) polarization direction (Figure 3-2b). For the negative poling, the sample was flipped over, so the polarization direction was downward (from film towards the substrate). All samples were poled at the same time to ensure the same treatment procedure and equal conditions for comparison purposes.

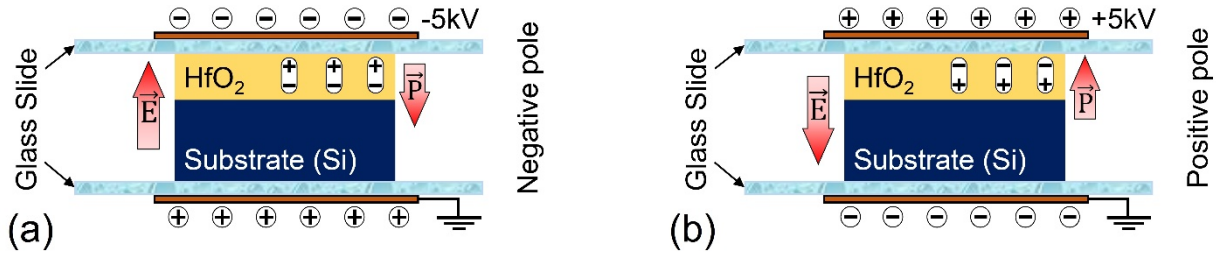

Figure 3-2. Schematic of poling setup for the positive and negative poling configurations. Two glass sheets with 100 µm thickness were placed on the top and bottom of the samples in order to prevent arcing between the electrodes. Separation of electrodes were 1mm.

3.2.5 KPFM

KPFM is a technique for the measurement of surface potential. This method is a scanning probe microscopy technique which records potential of the surface by applying a voltage to the tip. The surface potential depends on the work function of the electrons on the surface and can be attributed to the bonding energy of the electrons. Measurements for the sample were carried out in a scanning probe microscopy system (Asylum Research, MFP-3D) using a conductive silicon cantilever with titanium/platinum coating (OMCL-AC240TM-R3, the resonant frequency of 70 kHz and spring constant~2N/m). The sample with exposed hafnium dioxide layer was placed on the special holder and grounded. AFM tip initially tuned in air for regular AC mapping (tapping mode) of the surface and the

resonant frequency for this tip was found to be about 60 kHz. Then the tip was lowered and the parameters were adjusted for regular surface mapping. While tip was in contact with the surface, the system was switched to KPFM (in Asylum Research software, this mode is referred to Scanning Kelvin Probe Microscopy) and tip was tuned again while a voltage of 2 V was applied to the tip.

For regular roughness measurements, the tip moves on the surface line by line (256 lines for the whole square surface) until it reaches the end, however, for measuring surface potential, tip scans each line twice. During the first pass, it measures the surface roughness similar to regular roughness measurement and records it as the roughness profile for that line. For the second pass, the tip is kept at a constant distance from the surface (in nanometer range) and scans the same line. The tip's movement follows the recorded roughness profile to ensure that the tip always has the same distance from the surface. The term "NAP mode" is referred to when the tip is scanning the surface with a constant distance from the surface. For these films, the tip was lifted about 20 nm from the surface during the NAP mode. Figure 3-3 depicts a schematic of how tip moves on the surface while measuring the surface potential.

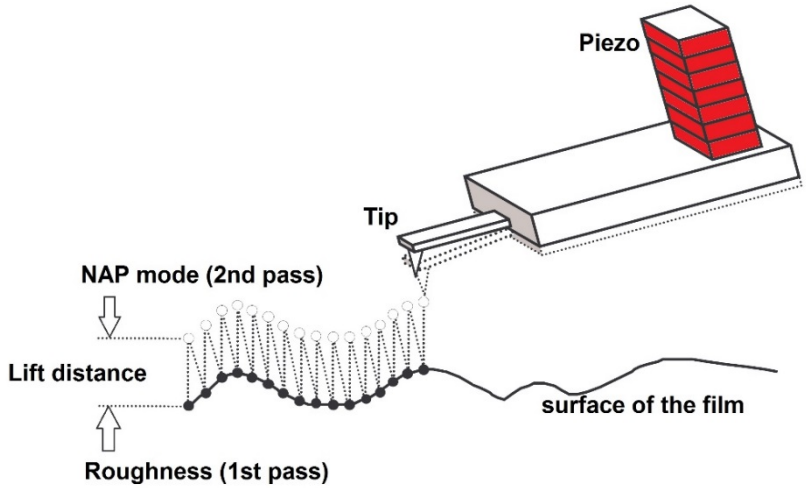

Figure 3-3. Schematic of tip positioning and movement in NAP mode.

3.3 Results and Discussion

3.3.1 Surface Potential

All three samples were studied by measuring their surface potential in the dark (OFF mode) and under the light (ON mode) using Kelvin probe force microscopy (KPFM) method. Surface potential depends on the location on the sample, so in order to measure the response from the same location of the sample while light turns on and off, scanning was disabled in one direction and only performed along a 2 µm long line (vertical direction in Figure 3-4.

Figures 3-4a, 3-4b and 3-4c show the surface potential for the negatively poled sample, unpoled and positively poled sample, respectively. During the scan, the light that was remotely provided by an optical fiber from a 150 W tungsten halogen lamp, was turned on and off in an equal time-frames in order to record the difference between surface potential for the time the light was on and off and also for the results to be comparable for all three samples. In Figure 3-4d, the cross-section of the image which is averaged over the total length of the scan for the three samples is presented. As evidenced by cross section image, polarization introduced an obvious change in the way that polarized and unpolarized samples responded to the light. When the light turns on, the negatively poled sample responds to the light in an opposite way compared to the positively poled and unpoled samples. In positively poled and unpoled samples, surface potential decreases when the light turns on while negatively poled sample, shows an increase in surface potential.

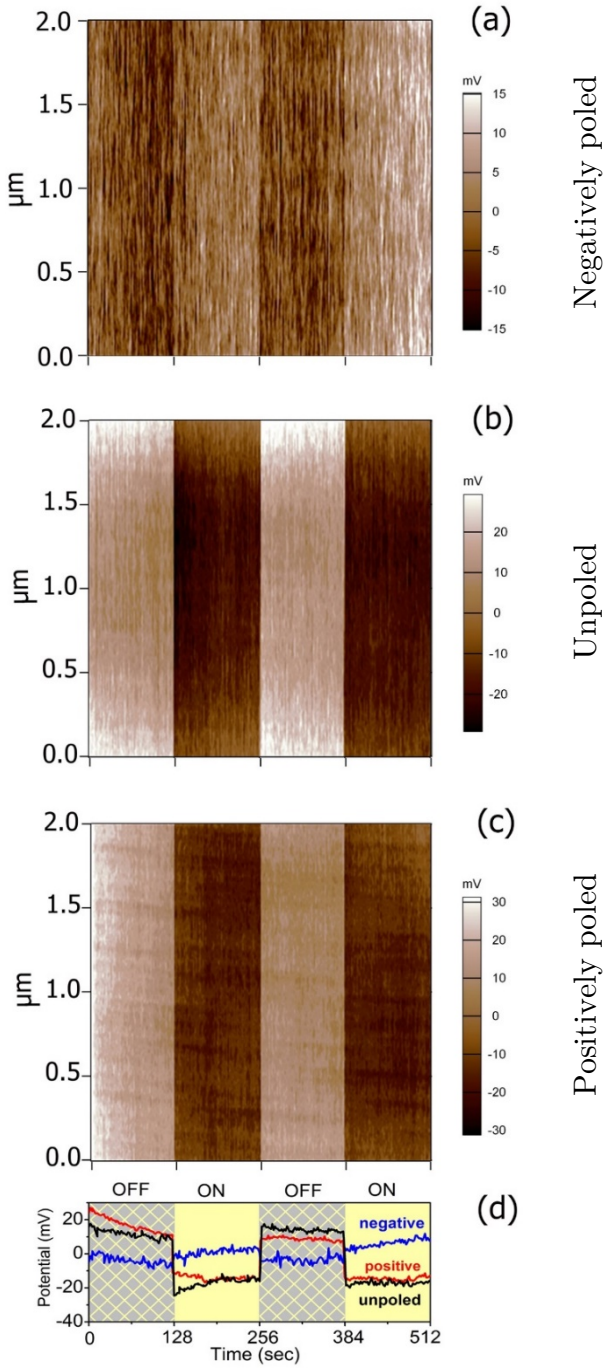

Figure 3-4. KPFM of the TiN-etched surface of the Si:HfO_2 thin film. Surface potential of the negatively poled (a), unpoled (b) and positively poled (c) films at OFF-ON-OFF-ON conditions. (d) Corresponding surface profile which is averaged over the entire vertical scanning length.

It is worth to mention that KPFM is a quasi-quantitative method and the measured values representing the difference between the potential of the tip and the surface are not absolute. The change in surface potential under illumination shows the photoconductivity response of the sample, however since there is no actual current passing through the film, due to the large band gap of the HfO_2 film, charge carriers are expected to face a high barrier in an actual cell. Therefore, complementary measurements were carried out to study the tunneling and carrier transport across the lamellar structure that includes a thin layer of ferroelectric hafnia.

3.3.2 Current-Voltage

The I-V diagrams of the three samples under AM1.5 illumination are presented in Figure 3-5. Interestingly, the polarization of the ferroelectric film of doped hafnia had a significant impact on the charge transport properties of the device's structure. The polarization of the film in the negative direction (dipoles aligned towards the Si substrates) improved open-circuit voltage (V_{oc}) compared to unpolarized sample and on the other hand, polarization of the film in the positive direction (dipoles aligned outward from the Si substrates) diminished open-circuit voltage. This is very important because it shows the importance of polarization direction and the fact that open-circuit voltage of a solar cell can be improved by utilization of a polarized film in an appropriate direction.

Hafnium dioxide has a large band gap (~5.7 eV). Taking into account, its band gap together with its small thickness of the layer, makes it very unlikely to be the source of the generated photocarriers, however, to make sure whether it has any photoresponse to the light source we carried out supplementary photoconductivity measurements on the surface of doped HfO_2 (~200 nm thick) using four-point probe system. The results confirmed the initial thoughts and showed that the resistivity of HfO_2 does not change

under illumination. Based on these results, we assume that the generation of the photocarriers occurs in the layer of Si adhering to the hafnia. It can be concluded that the lower band gap media (silicon) is the source of generated electron-holes and the polarization field from ferroelectric film separates them and drives them in opposite directions, thus explaining the occurrence of the photovoltaic effect in the Si/HfO_2 system.

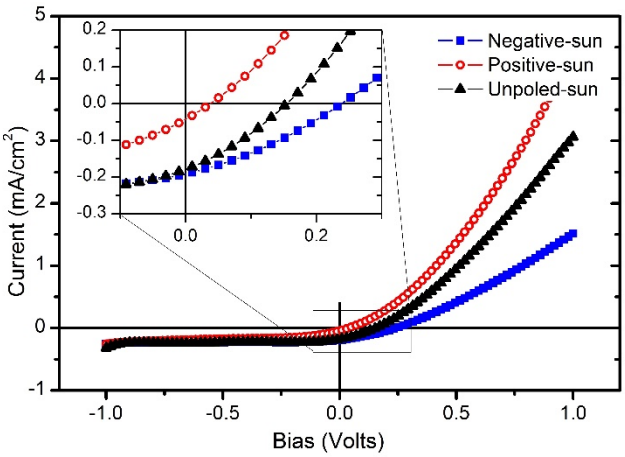

Figure 3-5. Current density-voltage characteristic of the Si/ HfO_2/Au cell. The inset is the magnified depiction of the identified region close to the zero bias voltage.

3.3.3 Band Diagram

Suggested band alignment for the positive and negatively poled samples in equilibrium and under illumination is presented in Figure 3-6. There is a substantial difference between band structures of the negatively poled sample and positively poled one. When the two samples are illuminated, the band alignment in the negatively poled sample increases the chance of transport across the ferroelectric layer. The light produces free electron-hole pairs inside semiconductor and by increasing the number of charges, their energy level increases and this may amplify the tunneling across ferroelectric layer or excite the electrons in order to easily transport across the FE layer.

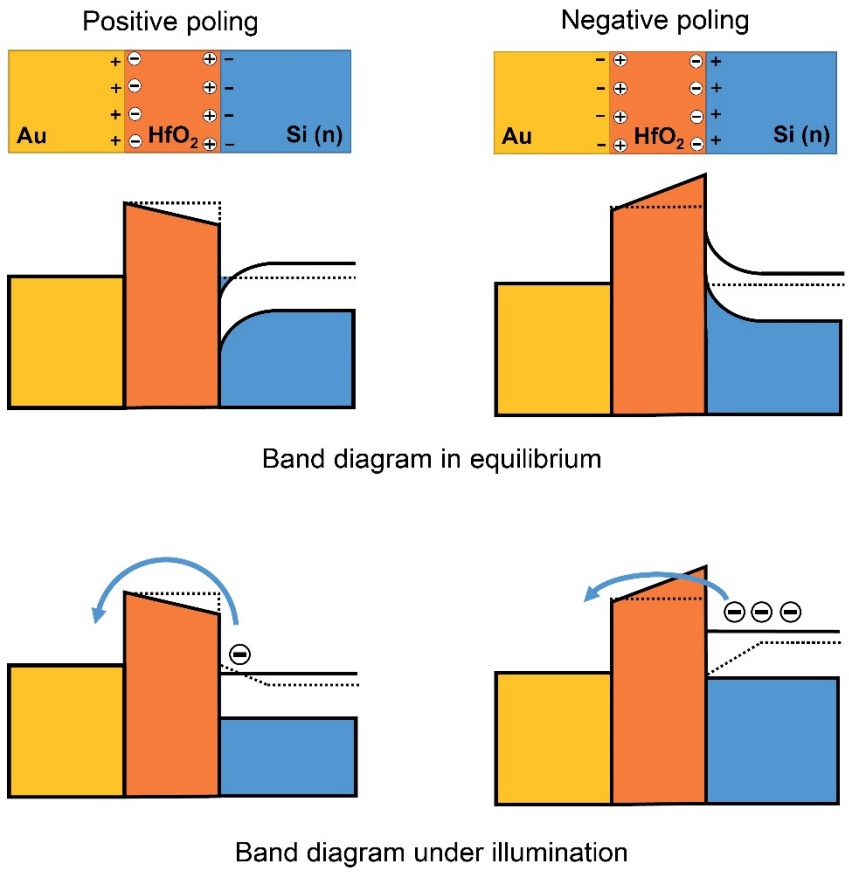

Figure 3-6. Band diagram change under illumination for positively (left) and negatively (right) poled samples.

3.4 Conclusion

We have demonstrated that the performance of ferroelectric-semiconductor solar cells can be enhanced by polarizing thin ferroelectric films in a proper direction. Polarization of ferroelectric layer impacts the open-circuit voltage and it can increase it if the polarization is performed in the correct direction.

KPFM and I-V measurements showed that photogeneration takes place inside the Si layer adhering to the ferroelectric film of HfO_2. On the other hand, highly resistive HfO_2 layer with larger bandgap did not show any trace of photoconductivity. Therefore,

silicon can be considered as the source of the carriers and occurrence of the photovoltaic effect in the Si/HfO_2 system can be ascribed to the existing ferroelectric layer.

The role of the electric field which separates photogenerated carriers and directs them towards solar cell electrodes was revealed by using different polarization directions of the ferroelectric layer. For the Si/ HfO_2/Au cell, the direction of poling made a difference in the way the cell responded to the light. Negatively poling the sample (ferroelectric dipoles turning towards the silicon) increased the open-circuit voltage while poling it in opposite direction lowered the photovoltaic properties by decreasing the open-circuit voltage and short-circuit current.

It can be speculated that the mechanism of generating or enhancing the photovoltaic effect by the means of electric field from the ferroelectrics can lead to a new generation of solar cells. It is expected that the efficiency of such cells can be greatly enhanced by fabricating multilayered structures. It is important to mention that our results indicate a great potential of ferroelectric layers to be implemented in conventional cells to enhance voltage in p-n junction based solar cells.

References

1. Würfel, P. *Physics of solar cells : from basic principles to advanced concepts.* (Wiley-VCH, 2009).
2. Liu, F., Wang, W., Wang, L. & Yang, G. Ferroelectric-semiconductor photovoltaics: Non-PN junction solar cells. *Appl. Phys. Lett.* **104,** 103907 (2014).
3. Alexe, M. & Hesse, D. Tip-enhanced photovoltaic effects in bismuth ferrite. *Nat. Commun.* **2,** 256 (2011).
4. Yang, S. Y. *et al.* Above-bandgap voltages from ferroelectric photovoltaic devices. *Nat. Nanotechnol.* **5,** 143–147 (2010).
5. Fridkin, V. M. & Popov, B. N. Anomalous photovoltaic effect in ferroelectrics. *Sov. Phys. Uspekhi* **21,** 981–991 (1978).
6. Glass, A. M., Linde, D. von der & Negran, T. J. High-voltage bulk photovoltaic effect and the photorefractive process in $LiNbO_3$. *Appl. Phys. Lett.* **25,** 233 (1974).
7. Glass, A. M., von der Linde, D., Auston, D. H. & Negran, T. J. Excited state polarization, bulk photovoltaic effect and the photorefractive effect in electrically polarized media. *J. Electron. Mater.* **4,** 915–943 (1975).
8. Brody, P. S. & Crowne, F. Mechanism for the high voltage photovoltaic effect in ceramic ferroelectrics. *J. Electron. Mater.* **4,** 955–971 (1975).
9. Basu, S. R. *et al.* Photoconductivity in $BiFeO_3$ thin films. *Appl. Phys. Lett.* **92,** 91905 (2008).
10. Choi, T., Lee, S., Choi, Y. J., Kiryukhin, V. & Cheong, S. W. Switchable Ferroelectric Diode and Photovoltaic Effect in $BiFeO_3$. *Science* **324,** 63–66 (2009).
11. Yang, S. Y. *et al.* Photovoltaic effects in $BiFeO_3$. *Appl. Phys. Lett.* **95,** 62909 (2009).
12. Cao, D. *et al.* High-Efficiency Ferroelectric-Film Solar Cells with an n-type Cu_2O Cathode Buffer Layer. *Nano Lett.* **12,** 2803–2809 (2012).
13. Qin, M., Yao, K. & Liang, Y. C. High efficient photovoltaics in nanoscaled ferroelectric thin films. *Appl. Phys. Lett.* **93,** 122904 (2008).
14. Seidel, J. *et al.* Efficient photovoltaic current generation at ferroelectric domain walls. *Phys. Rev. Lett.* **107,** 126805 (2011).
15. Pintilie, L., Vrejoiu, I., Le Rhun, G. & Alexe, M. Short-circuit photocurrent in epitaxial lead zirconate-titanate thin films. *J. Appl. Phys.* **101,** 64109 (2007).
16. Yao, K., Gan, B. K., Chen, M. & Shannigrahi, S. Large photo-induced voltage in a ferroelectric thin film with in-plane polarization. *Appl. Phys. Lett.* **87,** 212906 (2005).
17. Yang, X. *et al.* Enhancement of photocurrent in ferroelectric films via the incorporation of narrow bandgap nanoparticles. *Adv. Mater.* **24,** 1202–1208 (2012).
18. Shvydka, D. & Karpov, V. G. Nanodipole photovoltaics. *Appl. Phys. Lett.* **92,** 53507 (2008).
19. Asadi, K., de Bruyn, P., Blom, P. W. M. & de Leeuw, D. M. Origin of the efficiency enhancement in ferroelectric functionalized organic solar cells. *Appl. Phys. Lett.* **98,** 183301 (2011).
20. Yuan, Y. *et al.* Efficiency enhancement in organic solar cells with ferroelectric polymers. *Nat. Mater.* **10,** 296–302 (2011).
21. Böscke, T. S., Müller, J., Bräuhaus, D., Schröder, U. & Böttger, U. Ferroelectricity in hafnium oxide thin films. *Appl. Phys. Lett.* **99,** 102903 (2011).
22. Müller, J. *et al.* Ferroelectric $Zr_{0.5}Hf_{0.5}O_2$ thin films for nonvolatile memory applications. *Appl. Phys. Lett.* **99,** 112901 (2011).
23. Müller, J. *et al.* Ferroelectricity in yttrium-doped hafnium oxide. *J. Appl. Phys.* **110,** 114113 (2011).
24. Lehan, J. P., Mao, Y., Bovard, B. G. & Macleod, H. A. Optical and Microstructural Properties of

Hafnium Dioxide Thin Films. *Thin Solid Films* **203,** 227–250 (1991).

25. Triyoso, D. H., Tobin, P. J., White, B. E., Gregory, R. & Wang, X. D. Impact of film properties of atomic layer deposited HfO_2 resulting from annealing with a TiN capping layer. *Appl. Phys. Lett.* **89,** 132903 (2006).

Part II

Synthesis and Characterization of Multifunctional Epitaxial Thin Films for Micro-Origami Applications

Chapter 4:

Three-Dimensional Structures Built by Origami Techniques

4.1 Introduction to Micro and Nano-Origami

Today's technology is moving towards miniaturizing objects or producing them from smaller (miniaturized) building blocks. This gives us the advantage of a product that has benefits of a micro/nano-structured material. The benefits of nanomaterials have been proven for the humans and numerous efforts have been taken in order to make those benefits tangible in human's life. Once the nano-size structure is synthesized, assembly methods could be used to bring the building blocks next to each other and form larger complexes.[1] One of the methods that are used in building three-dimensional (3D) nano/micro size structures is called origami. Origami is the name of a Japanese art which means paper-folding. Although origami is mainly considered an art, it has had an obvious presence in high-end technologies such as satellites solar panel's unfolding system, automotive airbags and even a complete machine that can transform based on origami techniques.[2–4] Origami can convert a paper sheet into a complex free-standing structure and produce three-dimensional systems or machines. A beautiful example of this technique reported recently showing a robot that originally is in the form of a flat sheet and when starts folding, creates a 3D structure and then crawls like a machine. The authors have used computational origami software to design folding mechanism and used memory alloy composites to provide forces to accomplish self-assembly of the robot.[4]

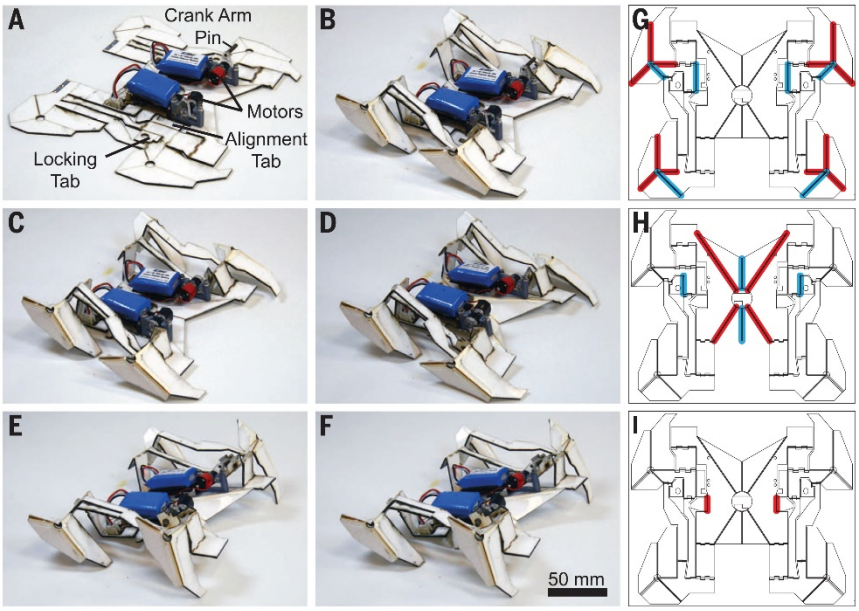

Figure 4-1. The self-assembly steps for the robot designed by origami techniques (Reproduced with permission from Ref.4).

Since the introduction of origami in technology, a variety of methods for self-assembling were developed at wide length scales between nanometer to centimeters[1]. When designing foldable parts by origami techniques, two options could be considered; either designing a mechanism that forms a permanent shape (static) and is not reversible or a structure that can repeatedly fold and unfold (dynamic) and can provide movable parts for the final product.[1,4]

Downscaling the figures that are built by origami techniques to micro and nano-size, requires appropriate materials with acceptable strength in that scale besides convenient methods for mass producing the product. The use of a nanomanipulator[5] could be considered as an option for making single nanostructures, however, for an applicable outcome that may require thousands or millions of nano-size figures, this method may not look wise. Instead, other methods that utilize natural forces that already exist in the structure or is built during production procedures such as surface tension, interfacial stresses, and adhesion forces, could be used as the driving force to accomplish the self-

assembling process. For example, external heat can be used to deform memory alloys or polymers which are embedded in the structure, photosensitive polymers can deform under the light, capillary forces can deform paper and interfacial stresses can produce driving force when the structure is released from substrate.[4,6–10] There are two ways to utilize these forces; either to use them to create permanent 3D structures or to embed them in moving parts that provide motion to the objects. The later has already gained a lot of interest in biomedical research. However, the structures must be in submicrometer scale to be applicable to live substances. This size limit rules out some of the options such as shape memories since they cannot hold their properties in smaller scales. Utilizing magnetic forces from magnetic materials will be a good choice for small dimensions since magnetic substances show strong properties even at nanoscale range.[11–15] In this chapter, I will review the methods and requirements for the creation of 3D structures that can be formed by micro-origami techniques and the focus will be on thin film methods for the preparation of them.

4.2 Active Forces in Thin Film Micro-Origami

A variety of forces can be utilized to transform and actuate thin film patterns into 3D structures. As mentioned, capillary forces and stresses that are built in the film or interface between the films are the most important ones. However, it is not just the force that determines the full process of transforming a flat sheet into origami structure. Beside force's magnitude, elastic moduli of the film substance and its thickness determine the shape or diameter of the curvature of the 3D structure. Additionally, the shape of the pattern, direction of etching and anisotropic stresses decides the direction of the curving.

4.2.1 Residual Stress

One of the main parameters that play an important role in thin film growth and the resulting product is residual stress. Polycrystalline materials that are grown with different mechanisms may produce significant residual stresses in thin film materials.[16,17] Island growth (Volmer-Weber) or Stanski-Krastanow growth[18] of polycrystalline films may result in significant residual stresses due to coalescence of grains. Also, growth of bilayered or multilayered films of different materials can produce interfacial stresses due to lattice mismatch between constituent phases. When the films with residual stresses are released from the substrate on which they were grown they undergo deformation.

The curvature of the films depends on the internal stress level and the thickness of the film besides the mechanical properties of the material. For the simple bi-layered beam the continuum elasticity theory predicts that the curvature κ (inverse of radius r) is:[17]

$$\kappa = \frac{6E_1E_2(h_1+h_2)h_1h_2\varepsilon}{E_1^2h_1^4 + E_2^2h_2^4 + 4E_1E_2h_1^3h_2 + 4E_1E_2h_2^3h_1 + 6E_1E_2h_1^2h_2^2} \qquad (4-1)$$

where E_1 and E_2 are Young's moduli and h_1 and h_2 are thicknesses of the layers and ε denotes the interfacial strain between the two layers. Based on this equation, it is easy to demonstrate the general rule that for the layers with similar thicknesses and Young's moduli the radius of the structures is inversely proportional to the film thickness. Thus, the smaller origami figures we wish to design the thinner films we must use. Multilayered patterns or complex shapes require numerical solutions by the means of computer simulations to predict their conformations at a certain level of residual stresses. The microstructure of thin films can vary with their thickness which results in variation of

residual stress across the film thickness. Thus, even the single polycrystalline magnetic films can form magnetic microtubes[19] or other micro-origami figures.

If the tensile stresses in the bilayers are smaller near the substrate than on the film surface, the film released from the substrate tend to bend under and may form wrinkles rather than regular micro-origami patterns. An example of wrinkled squares of magnetic films is presented in Figure 4-2. This indicates that the sequence of the deposition of the films matters. Depositing metal A on top of B will not result in the same structure as depositing B on A.

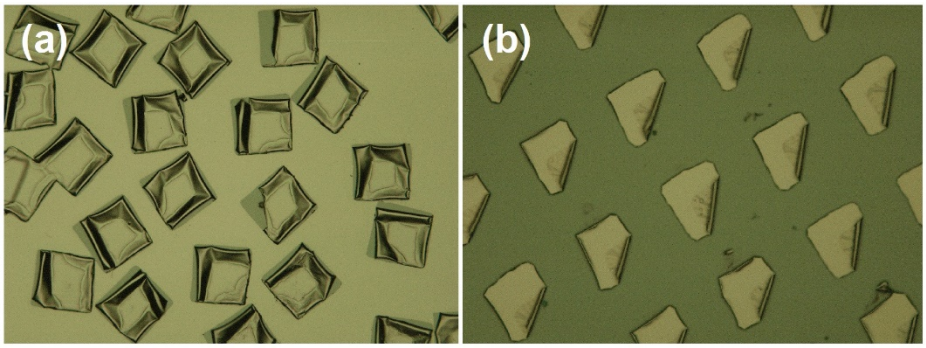

Figure 4-2. (a) Wrinkling of permalloy-Ti films and (b) correct rolling of the edges of Ti-permalloy squares.[35]

Residual stresses in thin film patterns or surface tension of adhering liquids can be used to create complex 3-dimensional structures from flat patterns. One can use origami techniques in micro or nanoscale to design such complex functional architectures. The technology of fabricating multiwall nanotubes and nanosprings from heteroepitaxial semiconductor film patterns was introduced by Prinz et al.[20–22] who used 7.5% lattice mismatch between adhering layers of different semiconductors. Growth induced stresses in dissimilar polycrystalline films were employed by Deneke et al.[19] to fabricate magnetic microtubes. Schumacher et al.[23] experimentally validated the relation between the interfacial strain, the diameter of a tube and the thicknesses of the deposited layers.

According to their model, the diameter of the microtubes can be controlled by adjusting the interfacial strain, elastic properties, and thickness of the constituting layers. Although the source of residual stresses induced in the films during their growth has been discussed in several review articles, the particular mechanisms responsible for self-rolling of magnetic films have not been identified. Also, the stresses in the polycrystalline films are very sensitive to deposition conditions such as base vacuum pressure or deposition rate[16] and therefore difficult to control. Beside conditions during deposition, residual stress can be controlled after growth, by application of external forces such as electric or magnetic force, heat, chemical reactions and so on.[24–26]

Stress engineering in multilayered 3D micro-structures is the key factor to control bending and rolling mechanisms. Epitaxial growth of films improves the stress and so ability to control rolling and bending the structures.

Rolling mechanism is due to the stress at the interface of the bilayers. Lattice mismatch is one of the main producers of this stress. The layer with lattice constant a_2 which is a bit larger than a_1 (lattice constant of the second layer), if deposited on a substrate with lattice constant comparable with a_1, will be compressed during deposition and this will produce a large stress at the interfaces.

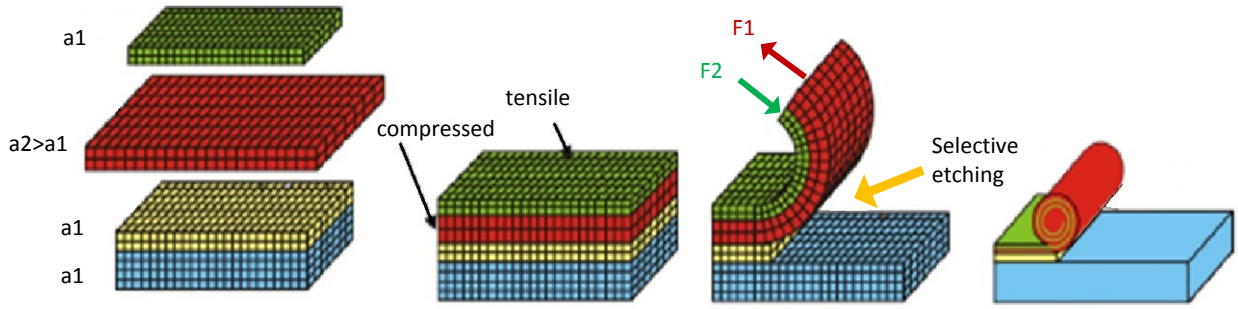

Figure 4-3. Heteroepitaxial semiconductor structures which result in formation of nanotubes of GaAs/InAs when sacrificial layer of AlAs on InP substrate is selectively etched releasing the film pattern from the substrate (reproduced with permission from Ref. 36).

4.2.2 Tension on the Surface

When it comes to micro- and nanoscale, some forces gain more importance than in macroscale. Surface tension in liquids is one of these forces. Capillary force or surface tension of evaporating drop of liquid can be utilized to pull and lift thin film patterns that are built by photolithography methods. Gagler[27] and Gracias et al.[28–30] used the same principal to produce 3D figures, such as boxes and pyramids with the size of several micrometers. Their patterns consisted of thick rigid films that formed the facets and connected with thinner, flexible films or polymers as hinges. This method can be used for magnetic applications by simply incorporating a magnetic film in the structure of the 3D shapes[27] or can serve as building blocks for mesoscopic meta-materials with interesting responses to electromagnetic waves and optical radiations.[31,32] An example of 3D origami shapes that are built by capillary origami is represented in Figure 4-4.

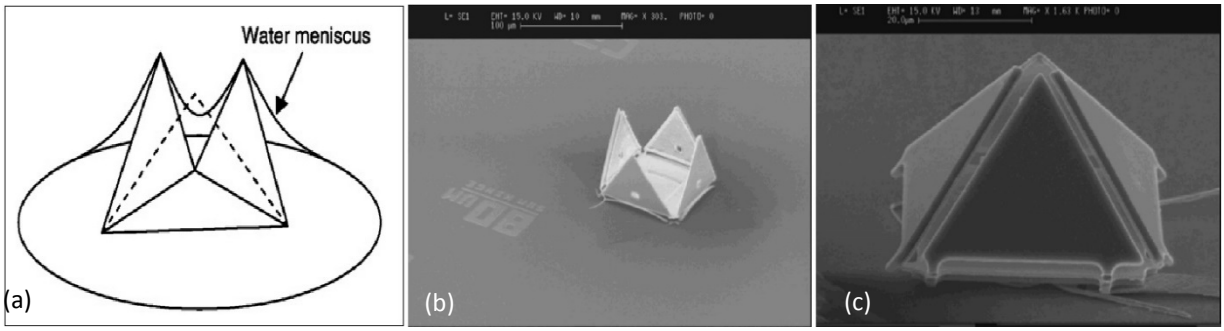

Figure 4-4. A micron size pyramid made with capillary origami technique. (a) Schematic of water meniscus around the facets while bending them, (b) and (c) SEM images of the pentahedral voxel during and after closure (reproduced with permission from ref. 27)

4.3 Thin Film Growth

4.3.1 Growth Mechanisms

The growth of the film on a substrate depends on different parameters. The temperature of the substrate, crystal structure and orientation of the lattice with respect to the surface, cleanliness of the substrate, deposition rate and pressure of the chamber during deposition are the most important ones to be named. Once vapors of the depositing material arrive at the surface of the substrate, they look for the positions with minimum possible energy and once they found it, form chemical bonds and settle at that location. Materials generally form crystals in order to lower the energy. So, if enough energy and time were given to the vapors and conditions optimized, atoms can diffuse on the surface of the substrate and find their lowest energy by forming a single crystal film (epitaxial growth). On the other hand, if these conditions are not provided, atoms get locked on the surface on random locations and form an amorphous film.[17]

Atoms moving on the surface (adatoms) can make chemical bonds with either substrate or another atom of the same type (deposited atoms). If the energy of the bond between deposited atoms is stronger than their bonding energy with the underlying substrate, the atoms tend to form islands instead of a uniform film. This type of growth is referred as Volmer-Weber (VW) island growth mode (shown in Figure 4-5). On the other side, if the arriving atoms are tightly bound to the substrate than each other, they prefer to attach to the substrate than to each other, so they cover the whole area of the surface before sitting on top of each other. This mode creates a layer by layer deposition which in most cases are desired. This mode is called Frank-van der Merwe (FM) growth mode. Sometimes, the situation changes after film grows in planar mode (FM mode) and favors cluster mode (VW mode) growth. In this situation, the film initially grows in the

form of layer by layer, then it forms islands on top of the bottom layer. The possible cause for this case could be the buildup of a force which was ignored at first place, but growth of the film has increased its magnitude and effect. This type of growth which is a combination of Volmer-Weber and Frank-van der Merwe growth modes is called Stanski-Krastanov (SK) growth mode.

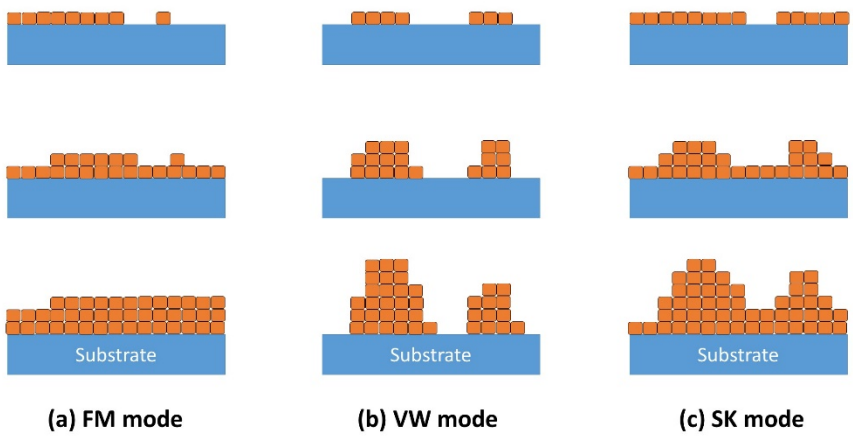

Figure 4-5. Mechanisms of thin film growth.

4.3.2 Epitaxy

Epitaxy is defined as the growth of a film in the form of a single crystal, meaning that all atoms and unit cells are oriented in the same direction and there is no breakage or dislocation of the atoms in the structure. If depositing material is same as the substrate in terms of material compound and structure, the growth is called homoepitaxy (e.g. GaAs on GaAs) and if different, it is been called heteroepitaxy (e.g. Ge on GaAs).

In order to produce an epitaxial film, some conditions need to be met. Beside necessity of having a clean and smooth substrate and optimum conditions such as substrate temperature, deposition pressure, rate, and etc. one parameter plays the most

important role which is defined as the mismatch (misfit) in lattice constants between the film and substrate. Lattice mismatch is defined by the following equation:[17]

$$M = \frac{a_s - a_f}{a_s} \qquad (4-2)$$

where a_s and a_f are the lattice constants of the substrate and the film, respectively. The value of lattice mismatch is been considered as the magnitude of the strain that film faces while formed on the substrate. For very thin films (only some atomic layers) the chemical bond between film and substrate may suppress the effect of the strain, however as the film grows, the strain increases and if the film cannot hold it, it will be cracked. Sometimes, a buffer layer can help to gradually change the lattice constant of the substrate in order to decrease the mismatch. In such conditions, epitaxial growth might be possible, however, the film may be polycrystalline and the interface may have a large density of dislocations and voids.

Figure 4-6 shows the growth mechanism for homoepitaxy and heteroepitaxy.

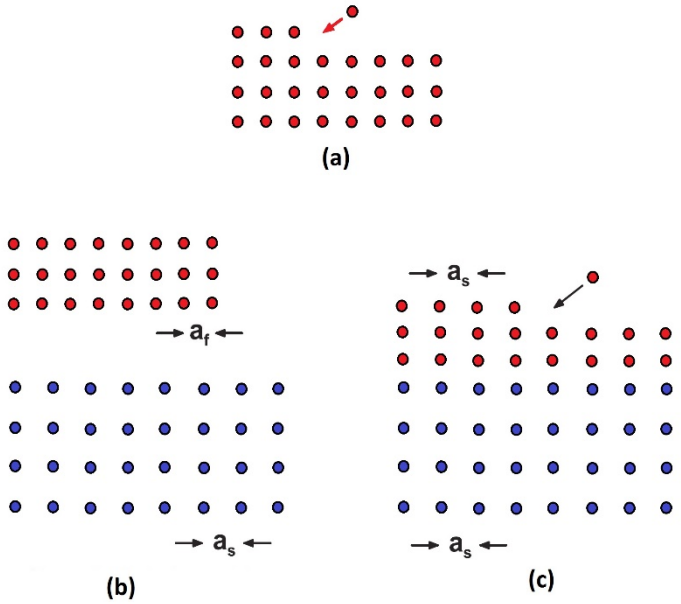

Figure 4-6. Schematic of epitaxial growth mechanism. (a) homoepitaxy, (b) Film and substrate crystals before deposition and (c) after heteroepitaxy.

4.3.3 Physical Vapor Deposition (PVD) Methods

A variety of methods is used for fabrication of thin films. High-quality films with minimum contamination generally are produced inside the chambers with high to ultra-high vacuum levels. This is necessary for minimizing contamination in the film by isolating deposition materials and substrate from the environment and to better control of the deposition parameters such as temperature, gas level and the ratio of the gasses and to prevent from undesired oxidation.

Depending on the nature of the process, each deposition method could be considered suitable for a specific application. Adding to this, the cost of the output makes some methods commercially feasible. Deposition methods are classified into two major groups: Methods which utilizes chemical reactions for the formation of product from precursors are referred as chemical vapor deposition (CVD) methods. Another group, on the other hand, utilizes physical methods (e.g. evaporating, sputtering and ion plating) in order to transfer depositing material to the surface of the substrate. These methods, in general, are referred to physical vapor deposition (PVD) methods.[18,33]

In this work, we have used sputtering and electron beam evaporation techniques in order to fabricate thin films. So, we briefly introduce these methods and their working principles.

4.3.3.1 Sputter Deposition

Physical sputter deposition is a non-thermal vaporizing process using highly energetic ions of noble gasses. The vacuum chamber is filled with noble gasses (mostly Ar) and by application of a high potential difference between the cathode (depositing target) and anode (substrate in which thin film will be deposited). Gas atoms ionize under high electric field and form plasma inside the chamber and accelerate toward the target

which results in the bombardment of the target by highly energetic ions. These ions interact with the target and transfer their momentum to the target and eject atomic particles from target's components. The ejected material travels in low-pressure chamber until reaches the substrate. Figure 4-3 represent a schematic of the sputtering process.

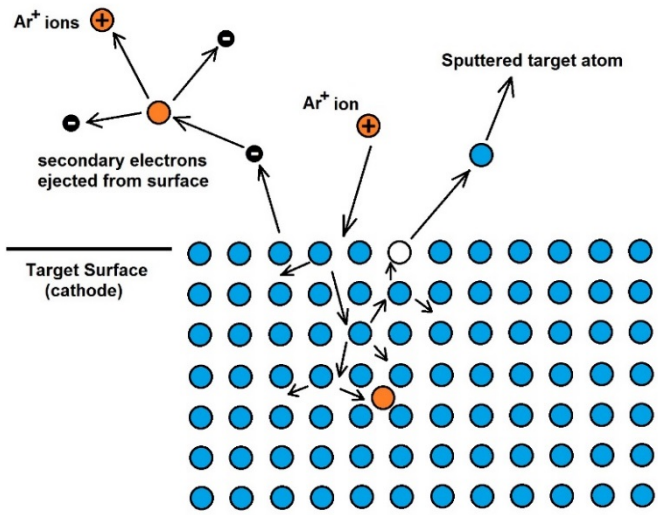

Figure 4-7. Schematic representation of sputtering process by bombardment of the target using Ar^+ ions.

The sputtering process can be done in the pressures in the range of 50 mTorr down to 10^{-5} Torr. It can be used for deposition of pure elements and for the compound materials either by using a compound target or by the addition of reacting gasses to the chamber in order to induce chemical reaction (reactive sputtering).

A noble gas is used as the sputtering gas and to create plasma, however, the yield of the sputtering process highly depends on the chosen gas. For depositing heavy atoms such as gold and silver, heavier (larger atomic weight) gasses such as Kr and Xe perform better, but for lighter elements, Ar provides better yield. He and Ne are too small compared to the most of the elements and sputtering yields are very small.[33] Considering the abundance and cost of the noble gasses, argon is the most used sputtering gas.

A modified sputtering system incorporates magnets in the design of sputtering guns in order to better guide and accelerate ions to the surface of the target. This modification improves the yield of the sputtering process and this type of gun is called magnetron sputtering gun.

4.3.3.2 Electron-Beam Deposition

In this physical evaporation method, a very high energetic and concentrated beam of electrons is guided to hit the target. The target is put inside a thermally insulating crucible (for some applications metallic crucibles are used, too) and energy of the incoming electron beam evaporates material either by melting it or by a direct sublimation process. The electron beam is produced by a tungsten filament by thermionic emission at the currents ranging between 20-30 A and an acceleration voltage of 10-20 kV. This electron beam is usually deflected by means of a magnetic field in order to protect e-beam gun from being exposed to the depositing materials. Crucibles are put in a water cooled liner made of copper. The liners are generally designed to hold multiple targets at the same time that gives the option of changing the targets without opening the chamber.

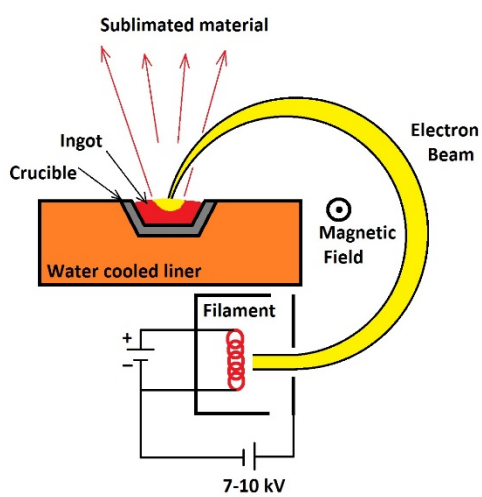

Figure 4-8. Operation principle of the electron beam evaporation gun.

Electron beam evaporation process does not require process gas, so the deposition process can be performed at very high vacuums and the gun can be designed for a UHV chamber which accordingly decreases contamination chance and improves films quality. A drawback of this process is when the target is an insulating material. At this situation, a charged cloud forms on top of the target and deflects incoming beam.[33,34]

4.4 Characterization Methods

Different techniques that were used for characterizing deposited film's properties are briefly introduced here.

4.4.1 Reflection High Energy Electron Diffraction (RHEED)

Reflection High Energy Electron Diffraction (RHEED) is an in-situ method for observing the crystal structure of the substrate film. It principally works based on diffraction of electrons from the flat surface of the film or substrate. Figure 4-9 shows how RHEED works. A very narrow and focused electron beam accelerated towards the sample and hits the sample with a small angle (less than 5°). After colliding with the surface of the sample, electrons are diffracted from the surface of the film and form a diffraction pattern on the opposite side of the chamber on a fluorescent screen. The diffraction pattern is in the form of dots or parallel lines and the distance between them is attributed to the spacing between crystal planes. If the dimensions of the chamber (L) is known, by measuring the distance between diffraction lines (D), lattice parameters (d_{hkl}) can be calculated using the following equation:

$$d_{hkl} = \frac{L\lambda}{D} \qquad (4-3)$$

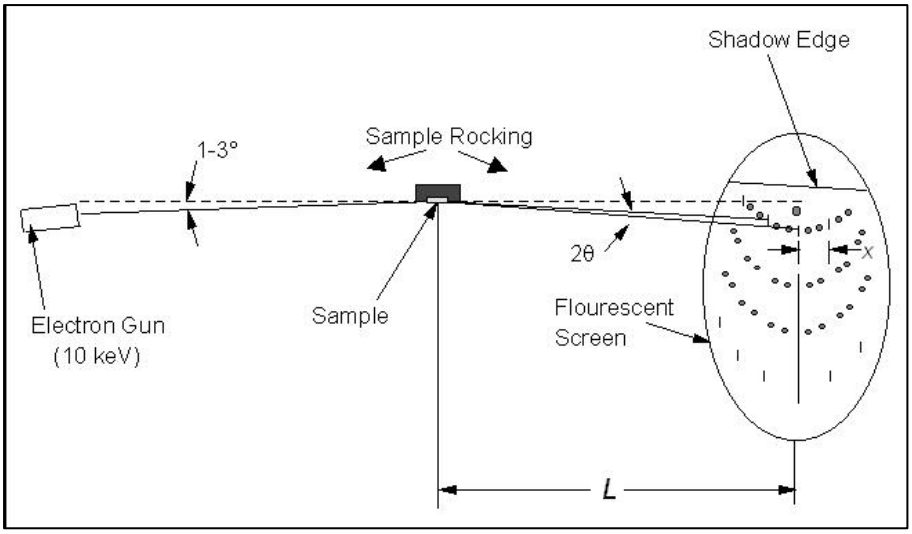

Figure 4-9. Schematic of RHEED working principle.

4.4.2 Auger Electron Spectroscopy (AES) and Energy Dispersive X-ray Spectroscopy (EDX)

Auger Electron Spectroscopy (AES) is an elemental analysis tool that is applied on the surface of the material and its depth of measurement falls within several atomic layers. The principle of AES relies on the atomic orbitals and the energy gap between them. As depicted in Figure 4-10, electrons at the inner shells of the atom such as K and L can be excited by an incident photon or bombarded electrons. Excited electron if gains enough energy, can escape from the shell and leave a vacancy behind. This vacancy can be filled with different mechanisms. If another electron from higher energy shell (such as L or M) drops into that vacancy, it will release energy equal to the difference between the energy of the two shells. This energy is in X-ray range and is characteristic of the element. However, this energy can be absorbed by another electron from higher shells and make them escape the material. Now, if the resulting X-ray is recorded, the method is called EDX (Energy Dispersive X-ray Spectroscopy) and if the ejected electron (Which is called

Auger electron) is recorded, the method is called AES. For the EDX, the energy of the X-ray depends on the difference in the energy of the involved shells in the transition. For the case that is presented in Figure 4-10, the transition occurs between L and K shells and the X-ray is referred as $K\alpha$ X-rays.

$$E_{K\alpha} = E_K - E_L \qquad (4-4)$$

Other transitions can occur between different shells such as $K\beta$ X-rays which results from $M \rightarrow K$ transition and $L\alpha$ X-rays from $M \rightarrow L$ transition.

The energy of the Auger electrons can be calculated knowing the transition shells and the energy of each one of them using following example for KLL transition:

$$E_{KLL} = E_K - E_{L_1} + E_{L_2} \qquad (4-5)$$

Other transitions such as LMM and MNN can be observed, too. For both EDX and AES recorded values of the energy are characteristic of the element and can be used for identification of the elements.

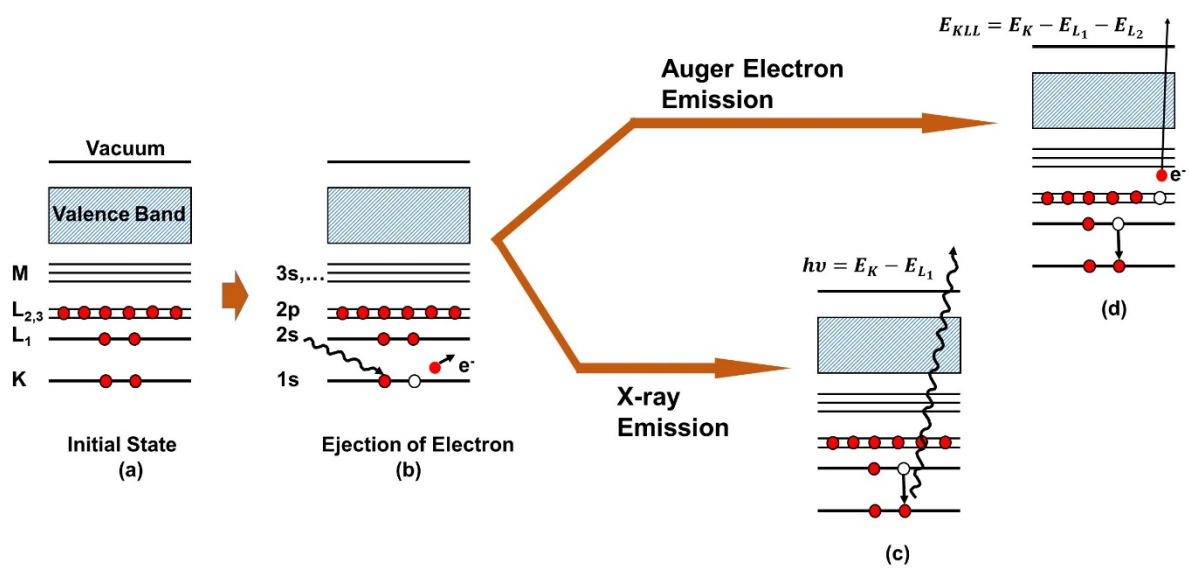

Figure 4-10. Schematic of electron transitions within the atomic orbitals which may result in two different outcomes: X-ray or Auger electron emission.

4.4.3 Scanning Electron Microscopy (SEM)

As mentioned in the previous section, the incident of an atom with electrons may result in ejecting electrons or photons which are characteristic to the elements. However, these are not the only products of the interaction of electron beam and material. When electron beam hits the material, electrons and photons at different energy levels are produced. The interaction volume is simulated to be in the form of a tear shape (Figure 4-11). Electrons can be ejected from different shells of the atoms with different energy levels or can be scattered with an small angle or large angles in which can result in different products such as weak or strong electron or sharp and high energy X-rays or continuous and low energy X-rays. The weak electrons which are called Secondary Electrons (SE) can only escape the material if they are produced in the vicinity of the surface (e.g. several angstroms). For this reason, they carry useful information regarding the morphology of the surface.

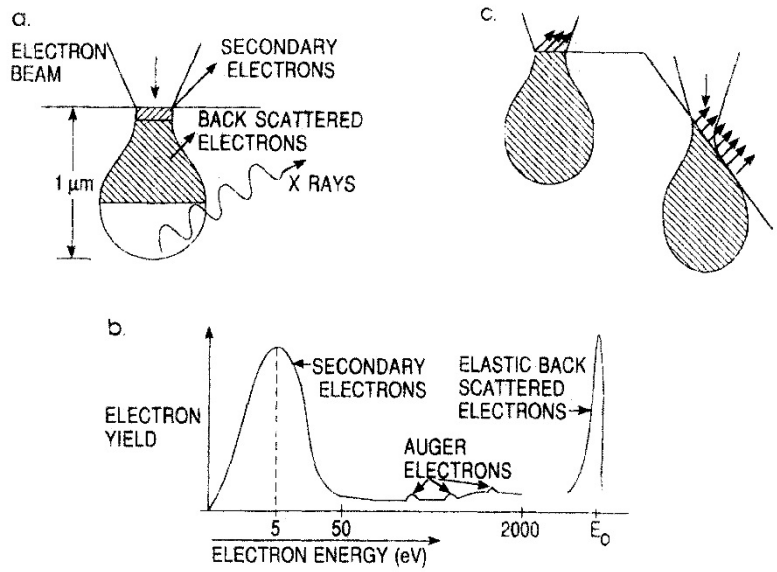

Figure 4-11. (a) Tear shaped interaction volume between incident beam and material, (b) typical range of the energy of the produced electrons (SE, Auger and BSE), and (c) principle of morphology observation by tear shaped interaction volume.[18]

As depicted in Figure 4-11c, once electron beam hits the material, depending on the surface morphology which determines the slope of the surface, more or less secondary electrons can escape from the surface. Thus, the magnitude of detected electrons will be different for the inclined and flat surface. This information once converted into visual representation by a cathode-ray tube (CRT), will show the morphology of the sample similar to an optical microscope. However, this technique provides information in nanometer scale which optical microscope are not capable of operation in that range.

Beside SE electrons which emit from the surface, backscattered electrons (BSEs) can bring information from deeper regions of the sample. These electrons are those which hit the atomic nucleus and deflect backward (back scatter). They have larger energies than SE electrons and they can provide information about the size of the atoms and density of the material since they will be more scattered when confronted larger nuclei and dense regions. Auger electrons and X-rays (Figure 4-11a) can be also recorded using appropriate detectors and be used for elemental analysis.

In order to record emitting electrons or photons without external interference, the material needs to be in a high vacuum. The resolution of the imaging depends on the energy of the incident electrons. For this reason, the electron beam accelerated in a columnar vacuum chamber and focused and scanned over the sample using multiple magnetic lenses and scanners. Different detectors are attached to the chamber in order to detect different products as discussed above. All of this is done in an instrument which is called Scanning Electron Microscopy (SEM). SEMs have different resolutions based on their design, gun type and gun power, focusing system and etc. The SEMs that are used for our measurements were JEOL Model 5410 and LEO 1530VP.

4.5 Goal of the Study

As discussed earlier, origami is a technique to create three-dimensional structures and in micro- and nanoscale, it can be accomplished by internal forces in thin films such as residual stress between the layers and this stress can be optimized and better controlled by deposition of epitaxial films. Stress due to the lattice mismatch between layers determines the direction of rolling. If the film is grown in polycrystalline form, the magnitude and direction of the strain forces at different grains will be different and they will cancel each other if they randomly oriented. However, growth of the film in epitaxial form aligns these forces and makes the strain force to be maximum. It will also makes the control of the rolling direction possible which helps in purposefully bending and rolling the structures in the desired direction.

Origami structures are usually built on a sacrificial layer which is dissolved or removed by different methods to release the structure. Thus, if the film desired to be epitaxial, the sacrificial layer needs to be epitaxial, too.

The purpose of this study was to produce and optimize epitaxial films to be served as sacrificial layers in micro-origami techniques for creating 3D structure. Deposition conditions of different materials on different substrates have been investigated and the results are presented in chapter 5.

The ultimate goal of this work would be the creation of 3D features on the surface of the solar cells. As earlier mentioned in the introduction of this chapter, one of the first technological applications of origami techniques in macroscale was for solar panels in spaceships. Now, in microscale, this technique can be used to modify the surface of solar cells by fabrication of free-standing photovoltaic structures or to improve efficiency of

cells by increasing the light absorption and/or concentration of the light. This can be done by fabrication of micro-lenses or prisms on the surface.

References

1. Whitesides, G. M. & Grzybowski, B. Self-Assembly at All Scales. *Science* **295,** 2418–2421 (2002).
2. Cheng, Q. *et al.* Folding Paper-Based Lithium-Ion Batteries for Higher Areal Energy Densities. *Nano Lett.* **13,** 4969–4974 (2013).
3. Min, C. C. & Suzuki, H. in *Manufacturing Systems and Technologies for the New Frontier* 159–162 (Springer London, 2008).
4. Felton, S., Tolley, M., Demaine, E., Rus, D. & Wood, R. A method for building self-folding machines. *Science* **345,** 644–646 (2014).
5. Heeres, E. C. *et al.* A compact multipurpose nanomanipulator for use inside a scanning electron microscope. *Rev. Sci. Instrum.* **81,** 23704 (2010).
6. Yasu, K. & Inami, M. in *Advances in Computer Entertainment* 406–420 (Springer Berlin Heidelberg, 2012).
7. Hubert, A., Calchand, N., Le Gorrec, Y. & Gauthier, J.-Y. Magnetic Shape Memory Alloys as smart materials for micro-positioning devices. *Adv. Electromagn.* **1,** 75 (2012).
8. Tolley, M. T. *et al.* Self-folding origami: shape memory composites activated by uniform heating. *Smart Mater. Struct.* **23,** 94006 (2014).
9. Paul, K. B. & Malkinski, L. Friction on the microscale. *Rev. Sci. Instrum.* **80,** 85110 (2009).
10. Guberan, C. Hydro-Fold by ECAL/Christophe Guberan on Vimeo. Available at: https://vimeo.com/39914902.
11. Vollmers, K., Frutiger, D. R., Kratochvil, B. E. & Nelson, B. J. Wireless resonant magnetic microactuator for untethered mobile microrobots. *Appl. Phys. Lett.* **92,** 144103 (2008).
12. Ishiyama, K., Sendoh, M. & Arai, K. I. Magnetic micromachines for medical applications. *J. Magn. Magn. Mater.* **242,** 41–46 (2002).
13. Pawashe, C., Floyd, S. & Sitti, M. Modeling and Experimental Characterization of an Untethered Magnetic Micro-Robot. *Int. J. Rob. Res.* **28,** 1077–1094 (2009).
14. Honda, T., Arai, K. I. & Ishiyama, K. Micro swimming mechanisms propelled by external magnetic fields. *IEEE Trans. Magn.* **32,** 5085–5087 (1996).
15. Fusco, S. *et al.* An integrated microrobotic platform for on-demand, targeted therapeutic interventions. *Adv. Mater.* **26,** 952–7 (2014).
16. Koch, R. The intrinsic stress of polycrystalline and epitaxial thin metal films. *J. Phys. Condens. Matter* **6,** 9519–9550 (1994).
17. Freund, L. B. & Suresh, S. *Thin film materials: stress, defect formation and surface evolution.* (Cambridge University Press, 2003).
18. Ohring, M. *Materials science of thin films: deposition and structure.* (Academic Press, 2002).
19. Deneke, C. *et al.* Fabrication of radial superlattices based on different hybrid materials. *Phys. Status Solidi Curr. Top. Solid State Phys.* **5,** 2704–2708 (2008).
20. Prinz, V. Y. *et al.* Free-standing and overgrown InGaAs/GaAs nanotubes, nanohelices and their arrays. *Phys. E* **6,** 828–831 (2000).
21. Nastaushev, Y. U., Prinz, V. Y. & Svitasheva, S. N. A technique for fabricating Au/Ti micro- and nanotubes. *Nanotechnology* **16,** 908 (2005).
22. Prinz V. Ya, Vorob'ev A. B., S. V. A. Three-dimensional structuring using self-rolling of strained InGaAs/GaAs films. in *Compound Semiconductors 2001* **170,** 319–323 (2002).
23. Schumacher, O. *et al.* Lithographically defined metal-semiconductor-hybrid nanoscrolls. *Appl. Phys.*

Lett. **86,** 143109 (2005).

24. Min, S. *et al.* Novel approach to control diameter of self-rolled magnetic microtubes by anodizing ti layer. *IEEE Magn. Lett.* **3,** 4000304 (2012).
25. Jackman, R. J., Brittain, S. T., Adams, A., Prentiss, M. G. & Whitesides, G. M. Design and Fabrication of Topologically Complex, Three-Dimensional Microstructures. *Science* **280,** (1998).
26. Moiseeva, E., Senousy, Y. M., Mcnamara, S. & Harnett, C. K. Single-mask microfabrication of three-dimensional objects from strained bimorphs. *J. Micromech. Microeng. J. Micromech. Microeng* **17,** 63–68 (2007).
27. Gagler, R., Bugacov, A., Koel, B. E. & Will, P. M. Voxels: volume-enclosing microstructures. *J. Micromechanics Microengineering* **18,** 55025 (2008).
28. Fernandes, R. & Gracias, D. H. Self-folding polymeric containers for encapsulation and delivery of drugs. *Adv. Drug Deliv. Rev.* **64,** 1579–1589 (2012).
29. Leong, T. G., Lester, P. A., Koh, T. L., Emma K. Call & Gracias, D. H. Surface Tension-Driven Self-Folding Polyhedra. *Langmuir* **23,** 8747–8751 (2007).
30. Cho, J. H., Azam, A. & Gracias, D. H. Three dimensional nanofabrication using surface forces. *Langmuir* **26,** 16534–16539 (2010).
31. Randhawa, J. S. *et al.* Three-dimensional surface current loops in terahertz responsive microarrays. *Appl. Phys. Lett.* **96,** 191108 (2010).
32. Cho, J. H. *et al.* Nanoscale origami for 3D optics. *Small* **7,** 1943–1948 (2011).
33. Mattox, D. *Handbook of Physical Vapor Deposition (PVD) Processing.* (Noyes Publications, 1998).
34. Frey, H. & Khan, H. R. *Handbook of Thin-Film Technology.* (Springer Berlin Heidelberg, 2015).
35. Malkinski, L. & Eskandari, R. in *Magnetic Materials* (ed. Maaz, K.) (InTech, 2016).
36. Prinz, V. Y. A new concept in fabricating building blocks for nanoelectronic and nanomechanic devices. *Microelectron. Eng.* **69,** 466–475 (2003).

Chapter 5:

Growth of Epitaxial Films for Origami Purposes

5.1 Introduction

As discussed in the previous chapter, Three-dimensional (3D) structures of multifunctional materials can be fabricated by the means of micro-origami techniques. This technology that relies on bending, folding, twisting or rolling flat thin film patterns to form free-standing functional structures, can be achieved by different mechanisms. Surface tension of a liquid droplets or the residual stresses that form during growth or after film formation, can be utilized to deform the film while it has been released from substrate. Film release from substrate can be done by wet or dry etching or by dissolving a sacrificial layer on top of which the patterns are grown. The process of removal of the sacrificial layer must be extremely selective, so it does not affect the film patterns or the substrate. For example, selectivity of chemical etching as high as 1:10,000 was required to fabricate multiwall nanotubes from GaAs/InGaAs semiconductor films using AlAs as a sacrificial layer.[1,2] Finding a new sacrificial layer is especially challenging in the case of heteroepitaxial structures, because in addition to high selectivity of removal of the sacrificial layer, both the sacrificial layer and the films grown on top of it must match the crystallographic structure of the substrate.

This technology initially introduced by Prinz et al.[3] to fabricate multiwall nanotubes and nanosprings from heteropeitaxial semiconductor film patterns. He used stress from the lattice mismatch of 7.5% between adhering layers of different semiconductors to make rolling of the thin film patterns possible. In dissimilar

polycrystalline films, stress from lattice mismatch may not be strong enough, however growth conditions can induce more stresses in which satisfy the forces needed for curling and bending the pattern. Deneke et al.[4] employed this technique to fabricate magnetic microtubes. Schumacher et al.[5] experimentally validated the relation between the interfacial strain, the diameter of a tube and the thicknesses of the deposited layers. According to their model the diameter of the microtubes can be controlled by adjusting the interfacial strain, elastic properties and thickness of the constituting layers. Several review articles (e.g. Refs. 6,7) have discussed the source of residual stresses induced in the films during their growth. Also, the stresses in the polycrystalline films are very sensitive to deposition conditions such as base vacuum pressure or deposition rate[8] and therefore difficult to control.

5.1.1 Previous Works (Magnetic Microtubes)

Magnetic microtubes with multiwall structure were designed and produced incorporating a sacrificial layer, a magnetic and an accompanying layer.[9–11] An array of 50 µm×50 µm squares films of polycrystalline copper layer with 50nm thickness was produced by lift-off lithography and sputtering methods on silicon wafer. Lithography steps were carried out in a class 100 cleanroom, with a deep UV exposure/mask aligner system from Newport, Inc. On top of the copper squares, using the mask aligner, another rectangular hole pattern with 20µm×50µm dimensions was produced in which portion of the rectangles was on the silicon substrate and the rest of it on the copper square. A layer of Ti with 20 nm thickness deposited as the bottom layer and second layer was chosen to be a magnetic film such as Ni (30 nm thick) or FeGa (40 nm thick). On the top, a thin layer of gold was coated to protect magnetic film from oxidation. All depositions were carried out with sputtering method using a magnetron sputtering system (model ACT Orion 8) form AJA International. Figure 5-1a shows an optical image of the whole

structure after stripping the residual photoresist and before etching the sacrificial layer. Copper layer that was considered as sacrificial layer was dissolved in a 30 wt. % solution of $CuSO_4$ at 70°C for 8 minutes. While dissolving the copper layer, the bilayers of Ti/Ni and Ti/FeGa started rolling upward due to the residual stresses that were produced at the interface between the dissimilar materials. The portion of the rectangular bilayer that was on the copper square started making a roll while the fragment that is sitting on the silicon served as an attachment of the microtube to the substrate. Figure 5-1b shows a SEM image of the magnetic microtube array and a larger magnification of a single roll is shown at the inset.

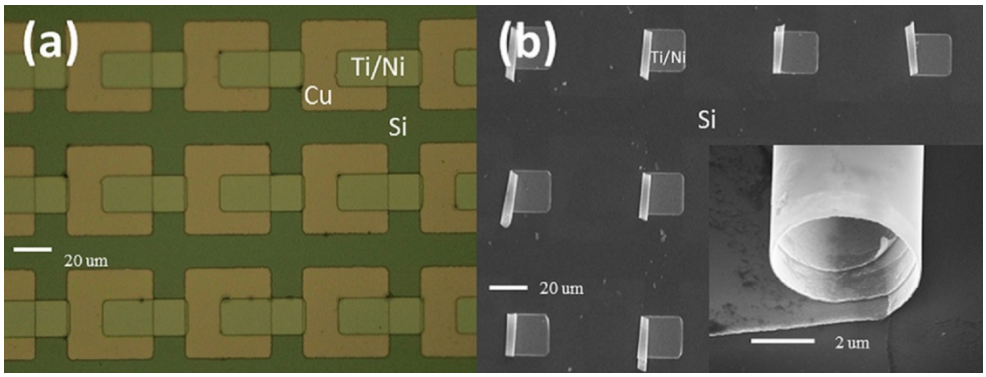

Figure 5-1. a) Optical microscope image of an array of flat rectangular film patches of Ti (20 nm)/Ni (30 nm)/Au (2 nm) on top of Si wafer and partially overlapping with sacrificial Cu films squares. b) Scanning microscope image of the array of magnetic scrolls and a magnified image of a single scroll in the inset formed after selective etching of Cu(Reprinted with permission from ref.9).

Having a polycrystalline sacrificial layer in which the whole structure was built on it resulted in a structure that is made of polycrystalline films. Deposition of polycrystalline films may not produce the largest possible stress at the interface or in the layers, however other techniques can be used to increase the stress and modify the bending or curling degree and size of the tubes. Figures 5-2 and 5-3 show examples in which diameter of the magnetic microtubes were decreased by anodizing non-magnetic layer of titanium.

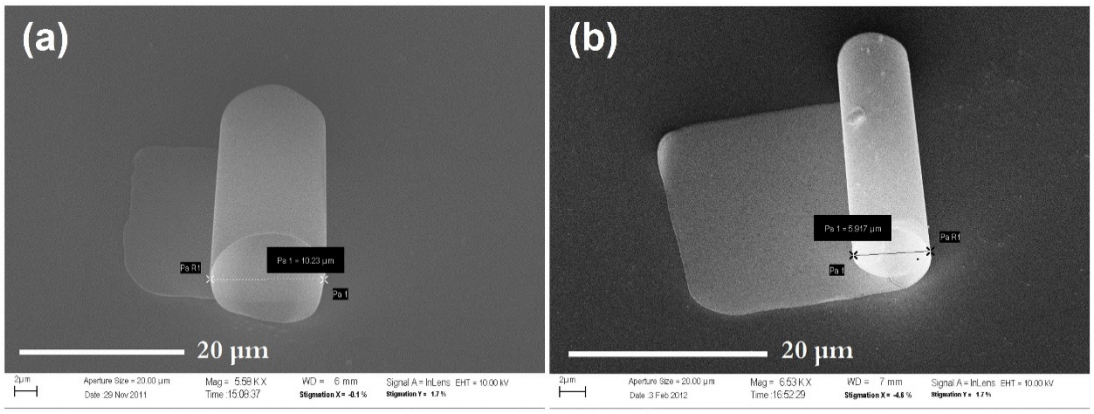

Figure 5-2. Effect of anodization of the Ti layer on the radius of the Ti(20nm)/FeGa(40nm)/Au(15nm) film. (a) Before and (b) after anodizing.[10]

Titanium (Ti) layer was anodized in ethylene glycol+NH_4F+H_2O solution with 60 V, 500 mA at 10°C for 15sec. Anodizing Ti layer converts Ti into TiO_2 which introduces a volume expansion and change in crystal structure, yielding more interfacial stress between magnetic film and anodized Ti layer. This stress increase reduces diameter of the microtubes by nearly 50 % (Figure 5-3 and Figure 5-4).

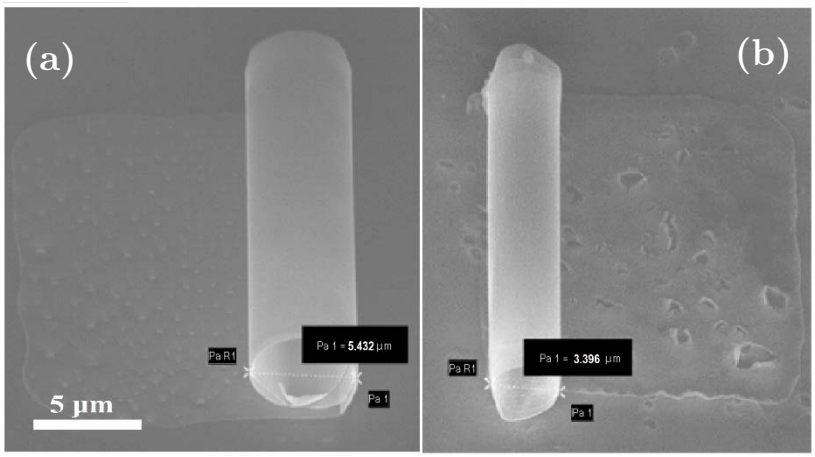

Figure 5-3. Effect of anodization of Ti layer on the radius of Ti(20nm)/Ni(30nm)/Au(2nm). (a) Before and (b) after anodizing.

Although, stress can be introduced even at polycrystalline films and interface between them, however maximum stress between two layers can be acquired when two layers possess highest possible mismatch so long as epitaxial growth of them on each other and substrate is permitted. Meaning that having a lattice mismatch between layers is essential to produce stress, though increasing the lattice mismatch reduces the chance of epitaxial growth. Theoretically, epitaxial growth is possible when lattice mismatch between layers is less than 10 %. In this chapter, the results of research on new sacrificial layers that can specifically be grown epitaxially on the desired substrate and also support epitaxial growth of the films and structures on top of them, are presented.

5.2 Experimental (Synthesis and Characterization Tools)

All synthesis of the films and characterization of the samples were carried out at thin film lab and shared facilities at the Advanced Materials Research Institute (AMRI) at the University of New Orleans (UNO). Three-chamber physical deposition system ORION-8 from AJA International Co. was used which consisted of a magnetron sputtering, an electron beam evaporation and an analysis chamber and quipped with the in-vacuum analysis tools such as thin film growth sensors, Reflection High Energy Electron Diffraction (RHEED) from Staib Co. with kSA400 analysis software and Auger Electron Spectrometer (AES) from OCI, which were used to determine, thickness, crystallinity and composition of the deposited films, respectively. The microstructure of the films was additionally investigated using electron microscopy tools: Scanning Electron Microscopy (SEM) and Field Emission Electron Microscopy (FESEM) and Electron Dispersive X-ray Spectroscopy (EDS). Both AES and EDS were used to verify that the sublimation of Zn films at after heat treatment.

Silicon (001) wafers, Sapphire (Al_2O_3, with (0001) orientation, from MTI) and magnesium oxide (MgO, with (001) orientation, from MTI) single crystal pieces were selected as the substrates for depositions. Prior to deposition, possible dust and particles contamination were cleaned from the surface of the substrates using ultrasonic cleaner for 10 minutes in acetone. Then organic contaminants were further cleaned in hot acetone (55-60ºC) for 10 more minutes following with 10 minutes dipping in hot isopropyl alcohol (IPA) at 55-60ºC with intense de-ionized water rinse after each step. Silicon wafers were etched in 4% HF at room temperature for one minute in order to remove native silicon dioxide from the surface and bare pristine and crystalline surface of the silicon. After final rinse, substrates were dried in high pressure nitrogen flow and right away loaded into the chamber.

Based on the survey of literature, some elements and compounds were selected considering their lattice mismatch, crystal structure and applicability and also availability of the deposition methods. Crystal structure and lattice parameters of the some materials are listed in Table 5-1.

Table 5-1. Lattice constants of some elements.

Element/Compound	Structure	Lattice Constants (Å)	Comments
Al2O3 (Sapphire)	HCP	a=4.758, c=12.99	
C (Graphite)	Hexagonal	a=2.4612, c=6.708	
SiC	Hexagonal	a=3.01	
ZnO	Hexagonal	a=3.252, c=5.313	
ZnSe	Wurtzite	a=3.98	
ZnS	Wurtzite	a=3.81	
CdS	Wurtzite	a=4.137, c=6.749	
Mg	HCP	a=3.21, c/a=1.63	Sublimates at 327°C
Ti	HCP	a=2.95	
Ru	HCP	a=2.7, c/a=1.584	
Co	Hexagonal	a=2.51	
Zn	HCP	a=2.66	Sublimates at 250°C

5.3 Results

5.3.1 Epitaxy of Zinc (Zn) on Sapphire

Out of selected elements and compounds in Table 5-1, zinc (Zn) shows an interesting characteristics. It can be sublimated at relatively low temperatures ranging from 160 ºC to 200 ºC in vacuum[12] and it has a matching lattice with some important metals such as cobalt (Co), titanium (Ti) and ruthenium (Ru). So, it can be considered as an excellent candidate for the sacrificial layer for micro-origami patterns. However, there is deep vacancy in the literature on the deposition of crystalline metallic Zn despite its major produce (ZnO) which attracted huge attention due to its many applications and has a mature research history.

Initially, direct depositions of Zn on sapphire were carried out via DC magnetron sputter deposition. The results showed that Zn films most of the time were oxidized during deposition and grew in the form of oxide clusters on the substrate. This was attributed to the deposition conditions such as lower vacuum processing in sputtering versus other vacuum depositions methods such as electron-beam (e-beam) evaporation in which increases the chance of oxidation in the chamber. Since Zn is highly reactive in vacuum, reaction with the oxide substrate was also considered. Review of literature shows that many metals between early transition metals to noble metals do not grow on oxides at room temperature,[13] therefore higher temperatures and/or buffer layers are required for deposition.[14,15] However, deposition temperature is limited for Zn by the sublimation temperature, so introduction of a buffer layer is necessary between sapphire and Zn layer. Ru, Ti and Co are three choices that have initial requirement to be matched with Zn which is low lattice mismatch. Since, Co is magnetic and may affect magnetic properties of 3D structure to be made on the sacrificial layer, just Ru and Ti were considered. Lattice

mismatch between Zn and these two materials can be calculated using Equation 5-1:

$$M = \frac{a_{sub} - a_{film}}{a_{sub}} \qquad (5-1)$$

which a_{sub} refers to the lattice vector of the substrate and a_{film} refers to the lattice vector of the film. Lattice mismatch between Zn film deposited on Ti calculated to be 9.8% and for Zn film deposited on Ru is 1.5%. Theoretically, both depositions could be epitaxial in regards to the lattice mismatch and similarity in crystal structure.

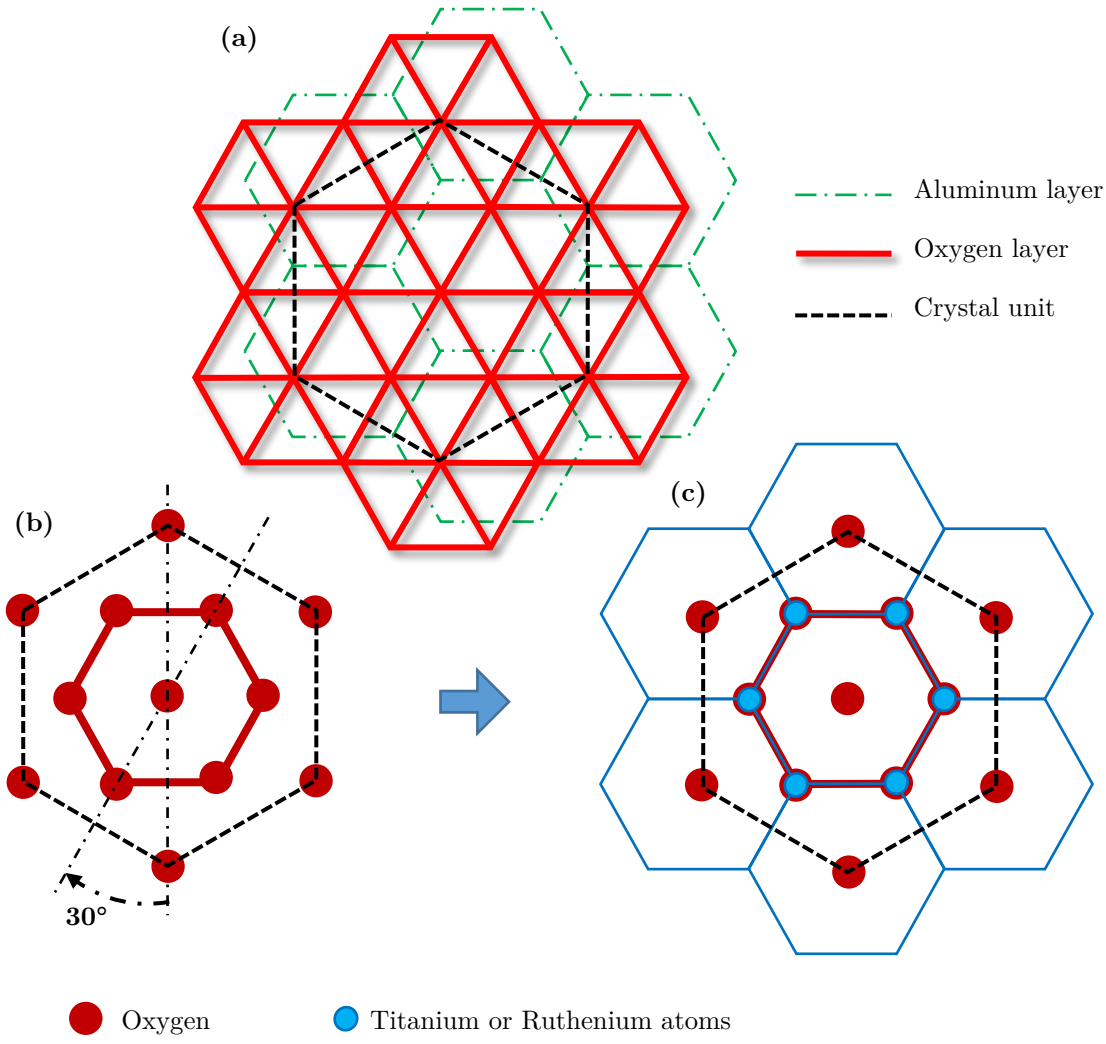

Figure 5-4. Schematic of lattice matching between sapphire and Ti or Ru films. (a) position of aluminum, and oxygen layers in sapphire. Locations of atoms are the intersections of the lines. (b) Sapphire lattice presenting positions of oxygen layer in c-plane, (c) possible epitaxial growth direction of the films. Note that Ti lattice will be 30 degree rotated relative to the sapphire lattice.

Before depositing Zn on buffer layers, conditions for epitaxial growth of Ru and Ti films on sapphire were investigated. If we imagine epitaxial growth of Ru on sapphire in which lattice vector $\vec{a}$ of Ru to be parallel to $\vec{a}$ vector of sapphire substrate, lattice mismatch based on the values of Table 5-1 will be more than 43% which strongly rejects the possibility of epitaxial growth. However if we consider oxygen layer from sapphire substrate, the distance between two neighboring oxygen atoms in its hexagonal structure is equal to 2.747Å and if we rotate Ru lattice about its c-axis, then its c-plane will exactly match with oxygen layer and the mismatch between them will be equal to 1.7% which proves the strong possibility of epitaxial growth of Ru on sapphire. Figure 5-4c shows the schematic of the orientation of the deposited film on the sapphire substrate and locations of the atoms of film and substrate.

Ru films were deposited by magnetron sputtering on sapphire and epitaxial conditions were optimized following the guidelines developed by Sutter et al.[14]. For the sample that showed the best crystallinity, chamber was pumped down to 2×10^{-8}torr and substrate heated up to 600ºC prior to deposition. DC power supply was set to 50W giving us a deposition rate of 0.4Å/sec and argon (Ar) flow was adjusted to be 18 standard cubic centimeter per minute (sccm) giving us a deposition pressure of 3×10^{-3}torr. Sample was rotated during deposition to obtain best possible thickness and temperature uniformity along the surface of the substrate.

Sputter deposition of Ru on single crystal Al_2O_3 (0001) substrate resulted in an epitaxial film which is a perfect seed layer for epitaxial growth of Zn. RHEED image of Ru layer is shown at Figure 5-5b.

5.3.1.1 Zinc on Sapphire with Ru buffer layer

Zinc film was deposited on Ru buffer layer at room temperature and elevated temperatures. Considering the sublimation of Zn at low temperatures and deepening on

the vacuum level, no film formed when deposition performed at temperatures higher than 150°C in vacuum level of 10^{-3} torr. Films created by sputtering showed very rough surface suggesting the strong oxidation of the film due to the nature of sputtering process which requires lower vacuum and incorporation of gasses which may increase oxygen level in the chamber.

Evaporation of Zn in an electron beam (e-beam) evaporation chamber gave us more uniformity and crystallinity compared to sputtering method which could be attributed to the better vacuum conditions. For the e-beam process, Zn pellets were placed in an alumina crucible in a multi-hearth electron gun from Telemark Company. Vacuum lowered to better than 10^{-8}torr and Zn is deposited at temperatures ranging from room temperature (RT) up to 100°C with deposition rates between 0.1-1.0Å/sec. Zinc film was subjected to the heat treatment in order to improve crystallinity and also test the sublimation procedure. Crystallinity of the film was investigated during deposition at different stages and after sublimation of the Zn film using RHEED and composition and morphology of the films were measured using AES, SEM and EDS methods.

5.3.1.1.1 RHEED Results

As earlier mentioned, the films grown by sputtering and e-beam evaporation directly on sapphire substrate were polycrystalline and rough. So, 10nm Ru buffer layer was deposited on sapphire to promote epitaxial growth of Zn layer. Figure 5-5 showed the RHEED results from the substrate, Ru layer and Zn layer when it was 30nm and 75nm thick and after sublimation of the film at 200°C. The results prove the epitaxial growth of Zn on Ru layer. The depicted images are from the sample that was deposited at 100°C and 0.2Å/sec deposition rate. Recovering Ru diffraction pattern after sublimation of Zn which was performed at 200°C for 10min, confirms Zn sublimation process.

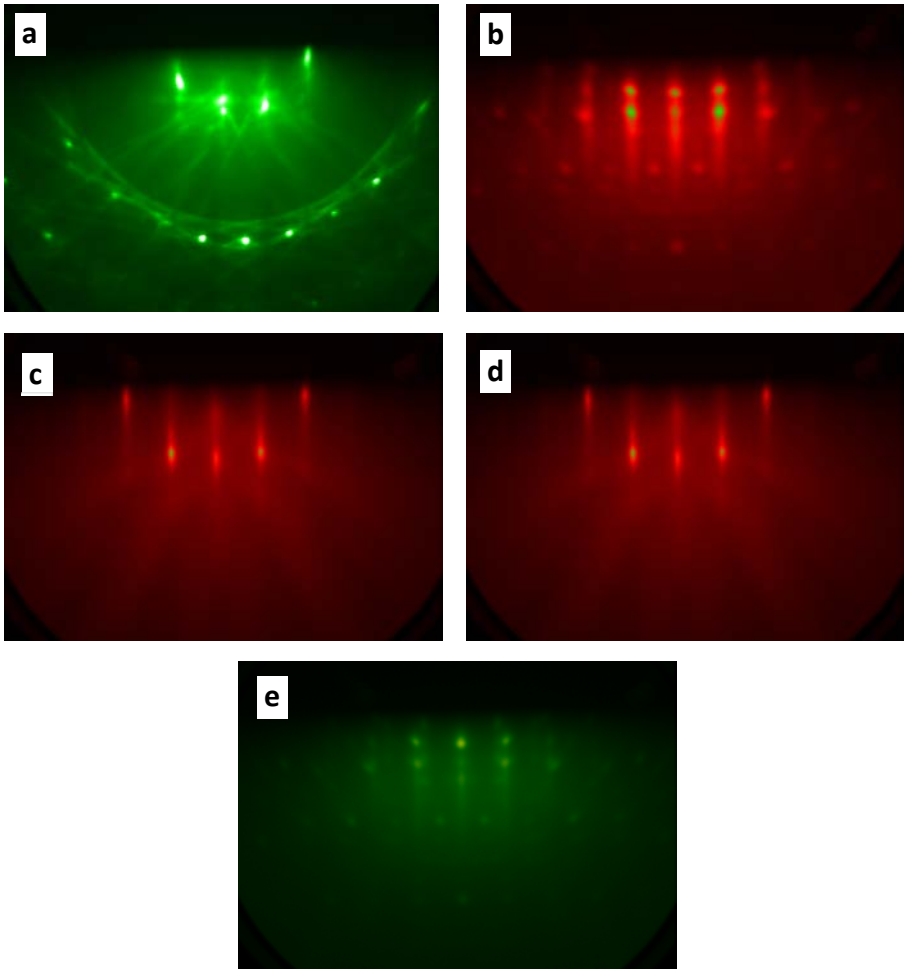

Figure 5-5. RHEED image from a) the sapphire substrate, b) 10nm Ru on sapphire sputtered at 600°C, c) 30nm Zn film on Ru, d) 75nm Zn film on Ru evaporated at 100°C, and e) After sublimating Zn at 200°C. All images are taken at 25kV along [1$\bar{1}$00] direction.

Although, most of Zn film sublimated at 200°C in vacuum and RHEED image after sublimation shows that the pattern is from Ru crystal but not Zn, but further investigations by AES and SEM show existing amount of Zn on the substrate. Detection of oxygen before and after sublimation shows the possibility of oxidation of Zn layer inside the chamber which will prevent complete sublimation of the film. Along optimizing the deposition conditions, heat treatment was applied to the films after deposition in order to improve crystallinity of the films. Figure 5-6 shows RHEED images of the Zn film at two

different directions [$1\bar{1}00$] and [$2\bar{1}\bar{1}0$] before and after heat treatment at 140°C, indicating improvement in the crystallinity of the film.

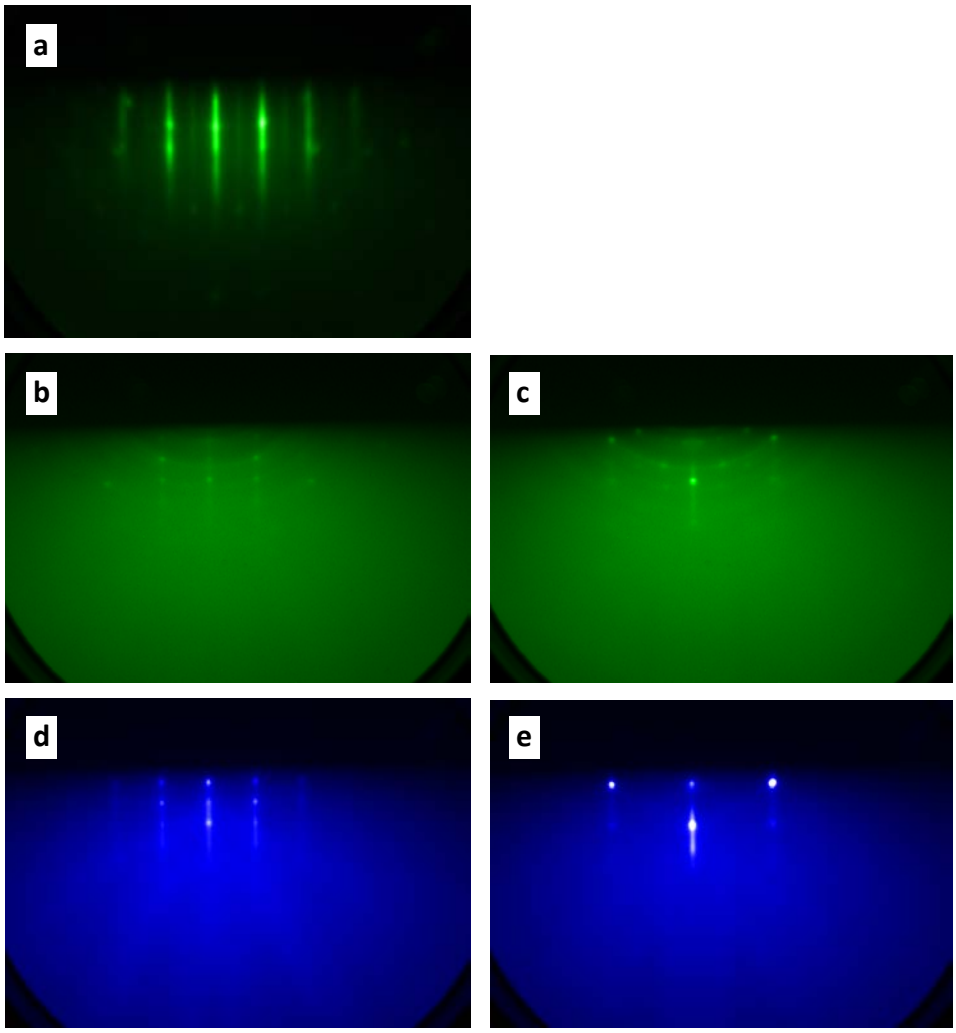

Figure 5-6. RHEED images of Ru (10nm) on sapphire at 600°C (a) and epitaxial Zn film after deposition at [$1\bar{1}00$] (b) and [$2\bar{1}\bar{1}0$] (c) direction and after heat treatment at 140°C in vacuum for 10minutes along [$1\bar{1}00$] (d) and [$2\bar{1}\bar{1}0$] (e). All images were taken at the acceleration voltage of 25kV.

5.3.1.1.2 AES Results

Auger spectroscopy results revealed more details about structure and composition of the film. After sublimation, Zn was still present in AES graph indicating that all of the Zn was not sublimated. The result could be explained by considering the second peak that

was present before and after sublimation and that peak was from oxygen. Clearly, oxygen was still present in the chamber even at vacuums better than 10^{-8}torr and due to high reactivity of Zn vapors, forms ZnO that mixes with the Zn film and/or oxidizes the surface of the film in which is stable at 200°C and remains on the surface after sublimation. Recovering Ru peak at AES graph, also proves the sublimation, though not complete.

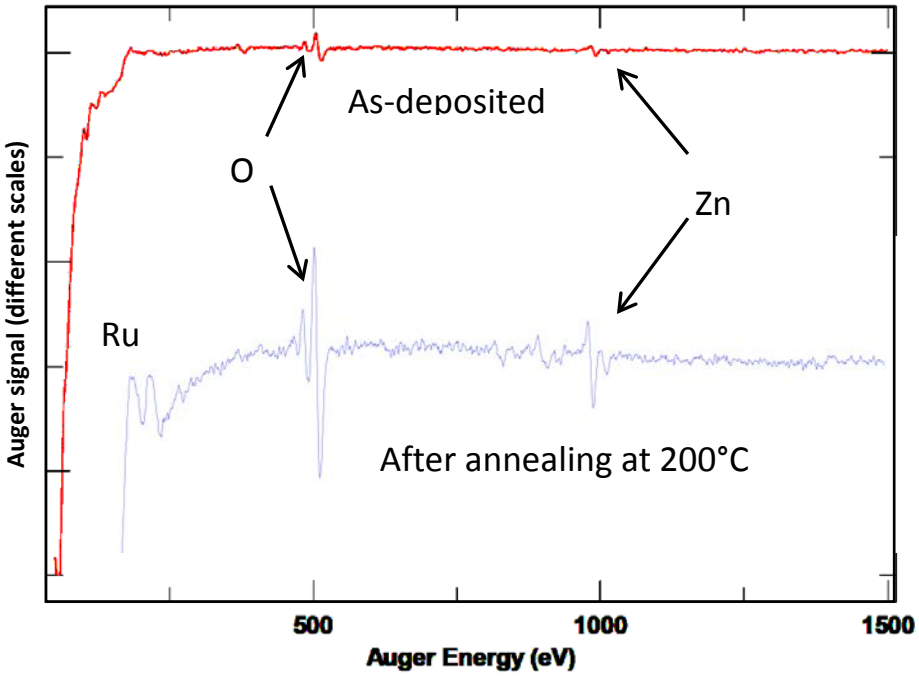

Figure 5-7. AES image showing the existence of oxygen on the surface of the films before and after sublimation, suggesting the oxidation of the Zn film in the chamber.

5.3.1.1.3 SEM Results

Along with RHEED and AES data, obtaining more information about morphology of the sample using electron microscopy methods seems necessary and complementary. What SEM pictures revealed from the Zn films on Ru layer, showed that film properties

highly depend on the deposition conditions such as deposition method, rate, temperature, substrate and vacuum level. Deposition of Zn by the means of sputtering or evaporation directly on sapphire substrate always resulted in island growth and formation of large well separated grains. The films with this kind of morphology cannot serve as sacrificial layers. Better results were achieved using electron-beam evaporation on top of Ru buffer layer. SEM results showed that for the films deposited via e-beam evaporation on Ru layer, lower deposition rates yields larger crystals and increasing deposition rate, rises the chance of depositing amorphous/polycrystalline films, while improving the roughness of the films. Clearly, larger crystals that were formed at low rates (smaller than 0.5Å/sec) produce very rough films. On the other hand, increasing the rate, produces an amorphous or polycrystalline phase that is like a matrix surrounding small crystals and the ratio of this amorphous matrix to crystals increases by increasing the deposition rate (Figure 5-8a, b and c). Although, higher rate does not produce a perfect crystalline film, its produces a smooth film which can be used as sacrificial layer for the growth of polycrystalline origami structures.

The increasing substrate temperature while maintaining deposition rate, promoted growth of larger crystals with better crystallinity. A comparison between morphologies of the films deposited at room temperature and at 100ºC is presented in Figure 5-8. What is obviously can be seen at SEM images, deposition at higher temperatures yielded a larger isolated crystalline islands on the surface, but not a film. This suggests that growth mechanism in these conditions follow the island growth (Volmer-Weber[16]) mode and does not yield in an acceptable film.

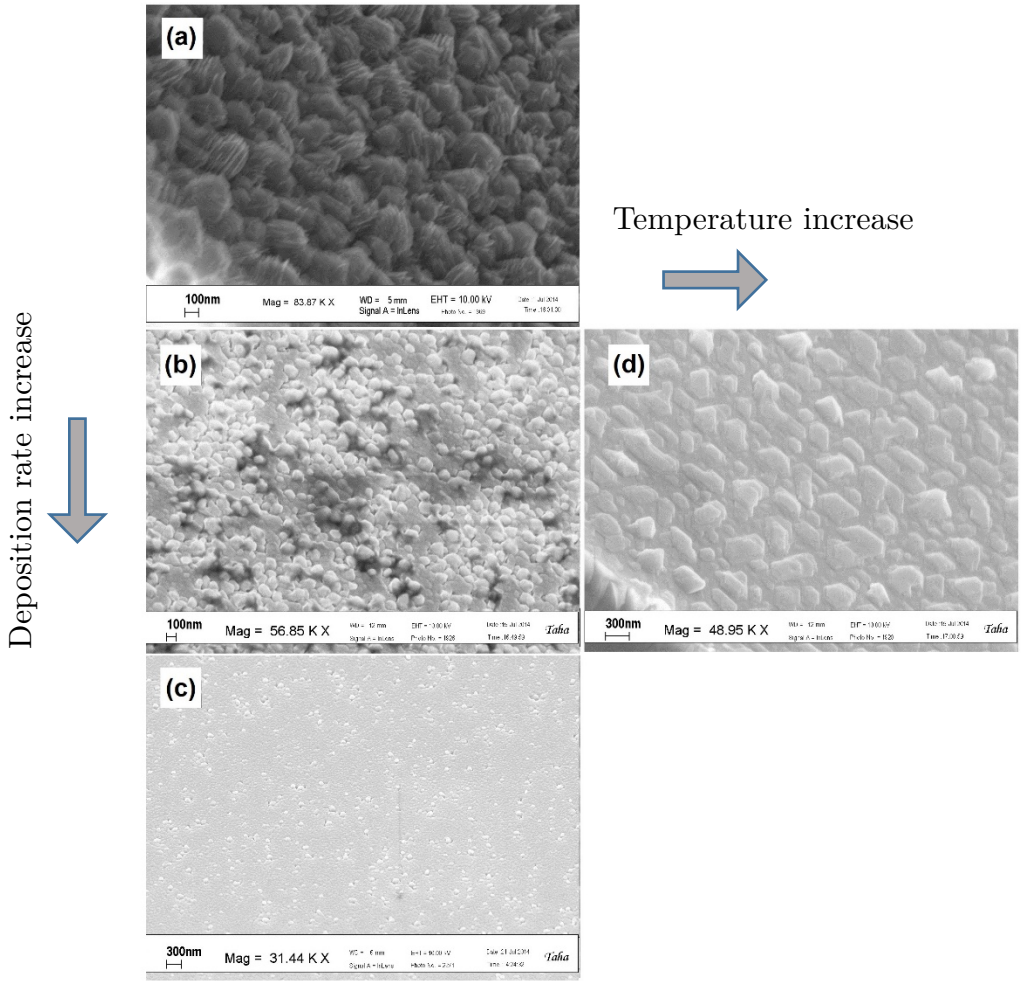

Figure 5-8. SEM images of surface of the zinc films deposited at different conditions. Images (a), (b) and (c) show the morphology of the films that were deposited at room temperature with deposition rates of 0.2Å/sec, 0.5Å/sec and 1.0Å/sec, respectively. Images (b) and (d) show the deposition temperature effect on the morphology of the films. Both (b) and (d) were deposited at 0.5Å/sec deposition rate, at room temperature and 100°C , respectively.

SEM images after sublimation of the films also confirmed AES results, showing an existing residue for almost all the samples. The amount of the residue which can be attributed to the ZnO due to oxidation during and/or after deposition, was dependent to the deposition conditions. Figure 5-9 is the SEM images from the samples represented at Figure 5-8 after sublimation process at 200°C for 10min. Clearly, sample that showed

better and larger crystals (Figure 5-8d) showed better results and less residue after sublimation (Figure 5-9d). The amount of ZnO residue on the samples that were deposited at RT at different rates, decreased by increasing rate. This suggests that slow deposition rate although may increase crystallite size but meanwhile increases chances for oxidation of depositing material, too.

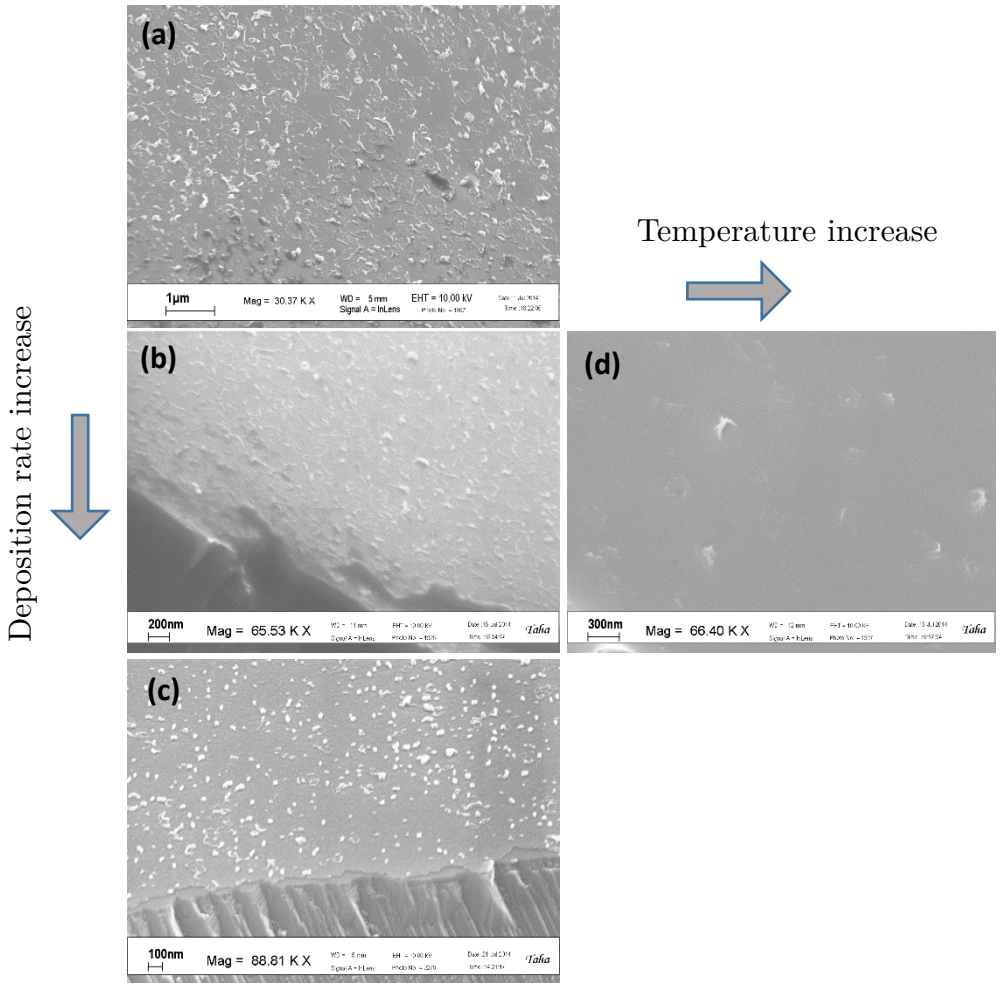

Figure 5-9. SEM image of the surfaces of the samples after sublimation of zinc film. (a), (b) and (c) relate to the films that were deposited at room temperature with deposition rates of 0.2Å/sec, 0.5Å/sec and 1.0Å/sec, respectively. Images (b) and (d) are from samples that were deposited at 0.5Å/sec deposition rate, at room temperature and 100°C, respectively.

5.3.1.2 Zinc on Sapphire with Ti Buffer Layer

Although, both Ru and Ti films were good quality single crystals, as evidenced by RHEED patterns(Figures 5-5and 5-10), Ti buffer layer looked to be a better option for Zn film since it produced smoother films with better crystallinity even at room temperature by e-beam evaporation. For this purpose, sapphire substrate was cleaned as explained in earlier section (Section 5.2). Ti layer was deposited to serve as buffer layer via e-beam evaporation system[17]. The chamber first pumped down to 7.0×10^{-8}torr and substrate was heated to 200ºC. 100nm of Ti film was evaporated at the rate of 0.2Å/sec at substrate temperature of 200ºC. The Zn film that showed the best crystallinity, was deposited at room temperature at the rate of lower than 0.2Å/sec with e-beam evaporation. Chamber's pressure at the beginning of deposition was equal to 6.0×10^{-8}torr and during deposition raised to 9.0×10^{-8}torr. All RHEED images were obtained at room temperature at the same direction as the substrate. Half of the sample were coated with 5nm of platinum (Pt) and other half was subjected to the heat treatment at 200ºC for 20min to sublimate Zn layer.

Titanium has a hexagonal closed pack (hcp) crystal structure with lattice constant $\vec{a}$ equal to 2.95Å and $\vec{c}$ equal to 4.68Å. Except for the very thin Ti layers (thinner than 6nm), the direction of epitaxial growth of Ti on sapphire is expected to be as following: Ti(0001) will be parallel to Al_2O_3(0001), Ti[$1\bar{1}00$] direction parallel to Al_2O_3[$2\bar{1}\bar{1}0$] and Ti[$10\bar{1}0$] will be parallel to Al_2O_3[$1\bar{1}00$] direction[15].

The mismatch between Ti layer and sapphire substrate considering the similar epitaxial growth mechanism that was explained at Figure 5-4, was calculated to be 7.4%. Also, the mismatch for epitaxy of Zn film on Ti layer is equal to 9.8% which confirms the possibility of epitaxial growth of Ti and Zn layers.

5.3.1.2.1 RHEED Results

RHEED diffraction patterns were obtained when the sample was at room temperature. Sapphire substrate rotated in which the electron beam be parallel to $[1\bar{1}00]$ direction of Al_2O_3 direction and kept at the same direction for the whole deposition processes. Figure 5-10 shows the RHEES pattern of sapphire substrate, 100nm of Ti film deposited at 200ºC and 100nm of Zn film deposited at room temperature. Straight and distinct parallel diffraction lines of Zn film proves epitaxy of it. Diffraction pattern is taken with incident beam parallel to $[1\bar{1}00]$ direction of the sapphire substrate.

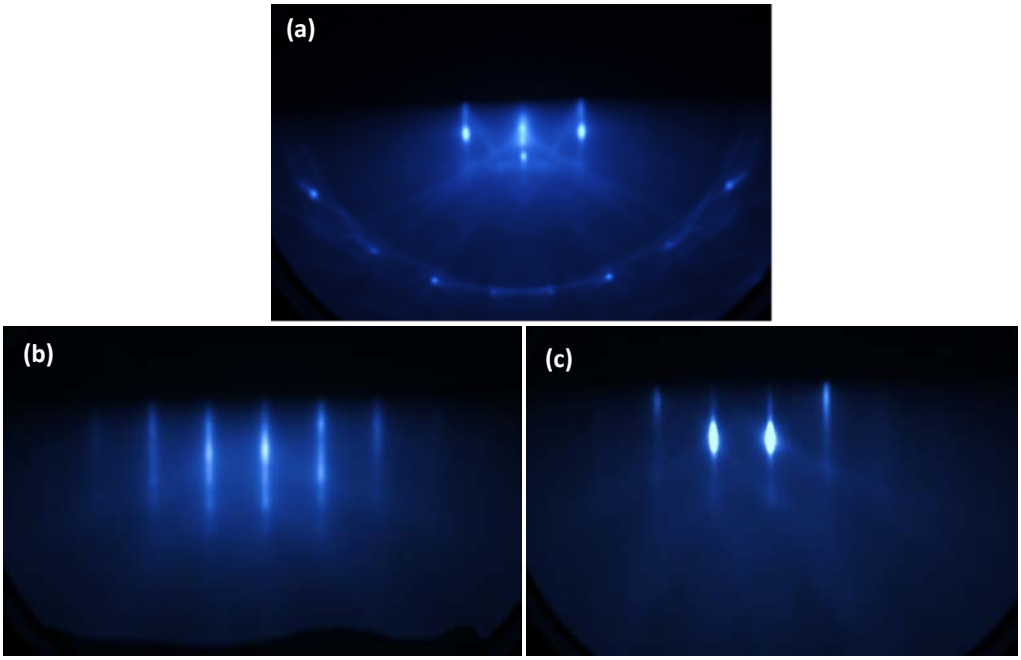

Figure 5-10. RHEED images of: (a) sapphire substrate, (b)100 nm film of Ti deposited by e-beam evaporation at 200°C, (c) 100 nm film of Zn evaporated on top of Ti at room temperature. All measurements were carried out at acceleration voltage of 20kV.

5.3.1.2.2 SEM Results

Morphology of the Zn films were deposited on Ti is presented in Figure 5-11. Tracing the growth mechanism of Zn layer, shows that Zn film start growing in an island form (Figure 5-11a) until islands join each other and form a continuous film (Figure 5-11b) with some evidence from grain growth. This looks different than the growth of Zn on Ru layer which was yielded a complete granular growth. Zn film on Ti could be from Stranski/Krastanov growth mode in which film grows in a mixed form of layers and islands[16]. Island form dominates at lower thicknesses and with increasing thickness of the film, continuous film forms, although some larger grains still rise above the surface (shown with red arrows in Figure 5-11c).

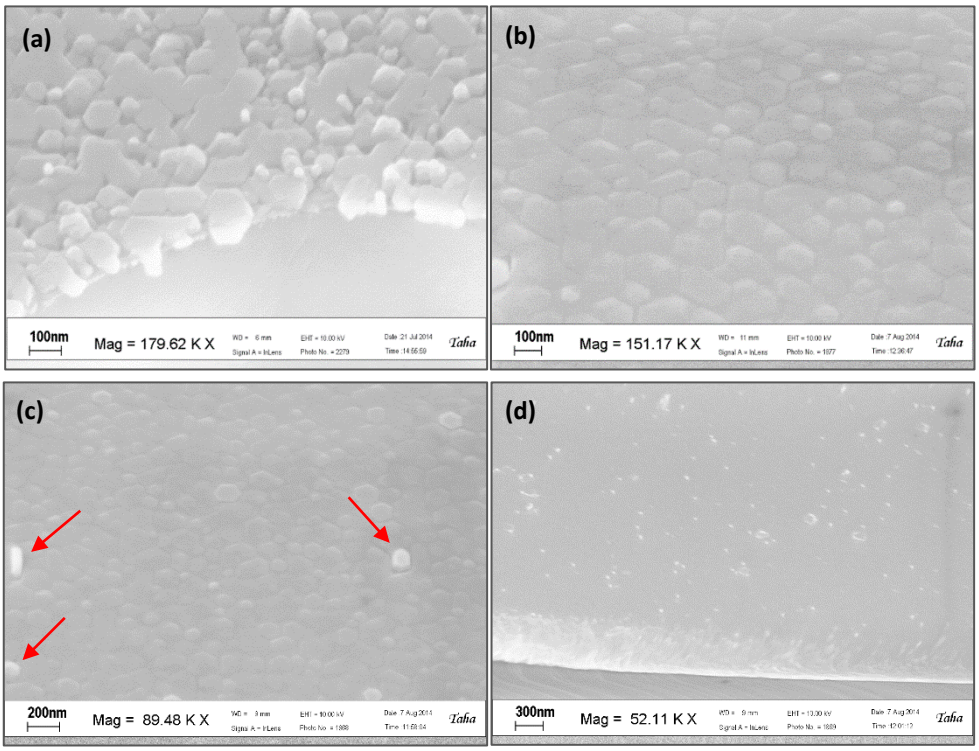

Figure 5-11. SEM graphs of Zn films deposited at room temperature with 50nm (a) and 100nm (b and c) thickness. Graph (d) shows the surface after sublimating Zn layer.

Sublimation results were also promising. Since, film had better crystallinity, oxygen incorporation was expected to be trivial or not at all. After sublimation of the film at 200°C for 20min, a surface which was much cleaner compared to the films with Ru buffer layer was recovered. Composition of the surface, before and after sublimation analyzed using an EDS system. Sample that was not subjected to sublimation, was coated with 5nm of Pt for protection.

EDS spectra prior and after sublimation is shown at Figure 5-12. Left graph shows the composition before sublimation. Zn peak is obvious along with smaller peaks of Al, Ti and Pt. Oxygen peak seems to be very small or zero, confirming the cleaner growth with less oxidation mechanism. Spectra for the after sublimation, shows no marks of elemental Zn and this proves nearly complete sublimation process.

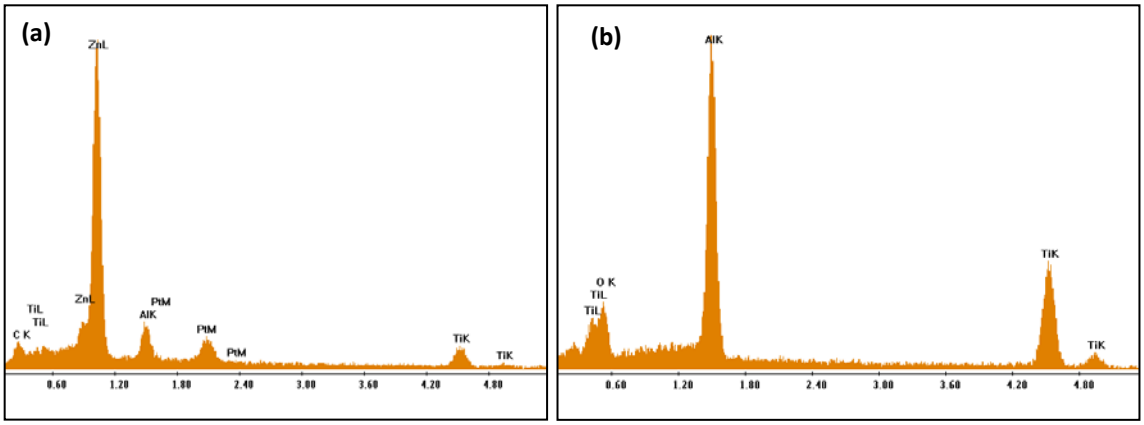

Figure 5-12. EDS measurement graphs of the Zn film before (a) and after (b) sublimation at 200ºC.

5.3.2 Epitaxy of NaCl on MgO

As explained earlier, for biological applications bio-friendly materials which don't require toxic and harsh process environment such as strong acids for synthesis, are needed. Regular salt (NaCl) which is consumed by humans, has interesting characteristics. It can be dissolved in water and is biologically and environmentally safe. Its crystal structure matches some common substrates such as MgO and moreover, variety of transition metals and oxides can be epitaxially grown on it.

In this section results of the experiments about epitaxy of NaCl is presented. NaCl deposition via e-beam evaporation technique was examined and optimized on MgO by varying deposition conditions such as deposition rate and temperature. First observations showed that when the surface of MgO is homoepitaxially coated with few nanometers of evaporated MgO, the crystallinity and roughness of the films coated on top of them was improved. For the case of NaCl on MgO with and without MgO modified surface the roughness is improved from 7nm to 4nm with evaporation of 5nm MgO on the MgO substrate. For epitaxial thin film growth, first thing to be considered is the crystal structure of film and substrate and the mismatch between them. Crystal structure of NaCl is same as MgO, both having face centered cubic structure with space group of $Fm\bar{3}m$. Lattice constant of MgO is 4.21Å and NaCl equals to 5.64Å. Now, if we consider epitaxial growth with the same alignment as substrate, the mismatch is above 25% which is not very promising. Therefore, salt crystal has to rotate 45° about c-axis, so its sides which have <100> sits parallel to diagonal direction of the substrate (along <110> direction) which is equal to 5.95Å with the mismatch of 5.5%. Figure 5-13 represents RHEED pattern of the MgO substrate and 70nm of salt evaporated on it with 30keV incident electron beam along <100> direction of the substrate. Samples deposited at

350°C with deposition rate of 0.1 Å/sec showed best characteristics considering epitaxy and roughness.

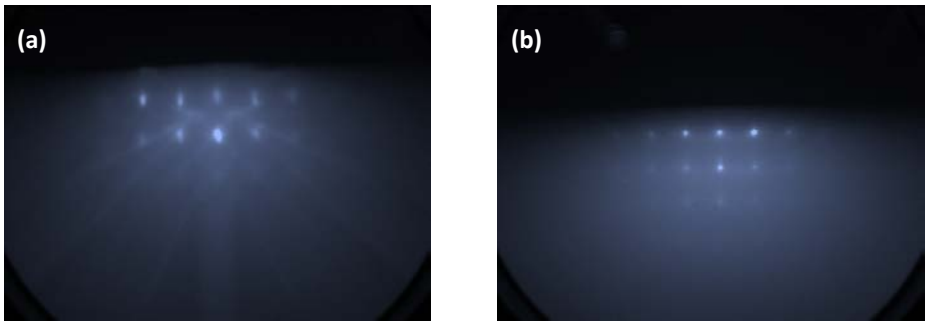

Figure 5-13. (a) RHEED image of virgin MgO substrate and (b) 70nm of NaCl evaporated at 350°C on 5nm MgO passivated MgO substrate along [001] direction.

5.3.3 Epitaxy of Cr and Fe on MgO

RHEED images are presented in Figure 5-14. Well defined diffraction spots are the sign of good epitaxial film. This substrate makes it possible to grow heteroepitaxial structures of NaCl and Cr (or other transition metals).

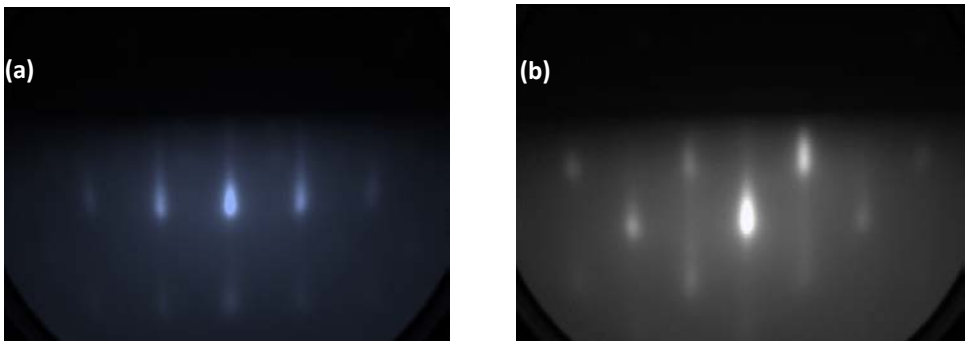

Figure 5-14. RHEED pattern from the surface of 15nm Cr deposited on NaCl (170nm)/MgO(5nm)/MgO substrate along <100> (a) and <110> (b) directions of the substrate. Incident beam voltage was 10keV.

Iron (Fe) seems to be a good candidate to be grown on top of MgO. With slight modification of the MgO surface with 5 nm homoepitaxy of MgO, the quality of the

substrate improves and Fe can be grown epitaxially on MgO. The RHEED results are presented in Figure 5-15.

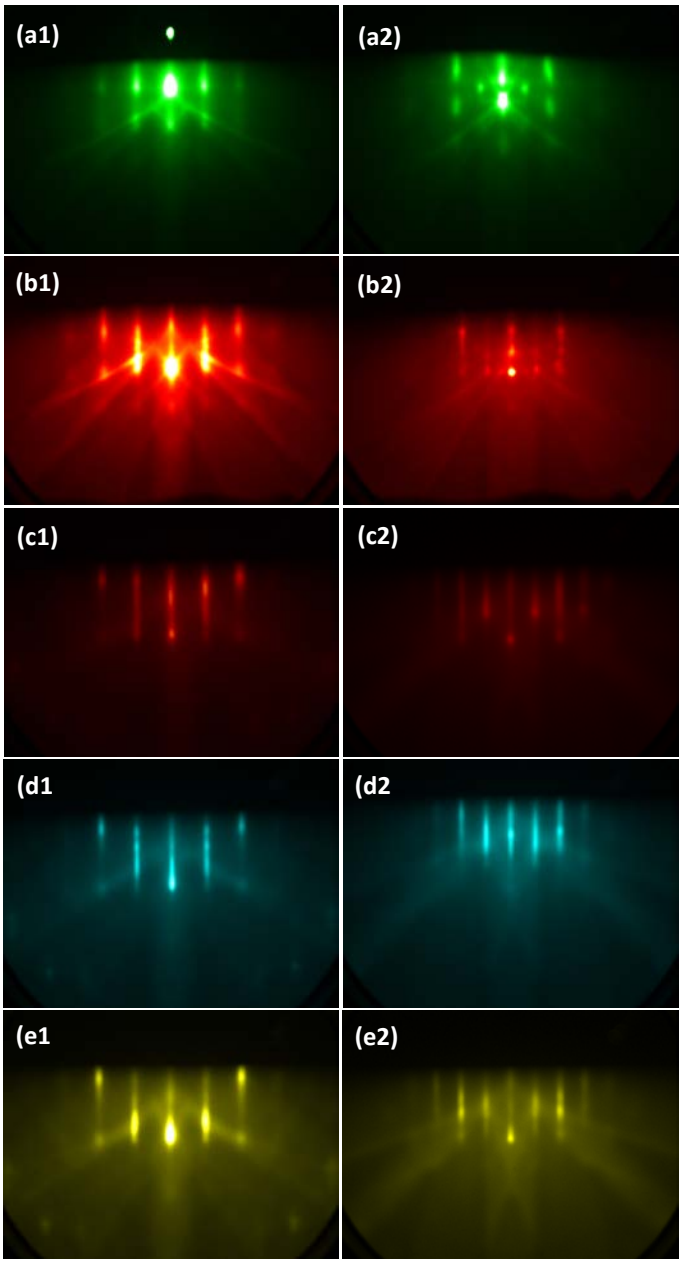

Figure 5-15. RHEED pattern of MgO substrate (a), after 5nm MgO homoepitaxy (b), 10nm of Fe (c), 20nm of Fe (d) and 30nm Fe (e). Pictures are taken with the 25keV incident beam along <001> (left side) and <011> (right side) directions (unpublished).

5.4 Conclusion

Successful microtube production using micro-origami techniques encouraged us to optimize the synthesis conditions and structure of them for their diverse applications. We speculated that this technology can be utilized in fabrication of three-dimensional structures on the surface of solar cells such as micro-rolls or micro-prisms that serve as concentrating lenses in order to improve efficiency of solar cells.

Initial works on microtubes were carried out with incorporation of a thin polycrystalline copper layer as sacrificial layer. The structure that was built was polycrystalline and the process for dissolving Cu needed strong acids. This could prohibit their usage in bio applications. Therefore, introducing a new sacrificial layer that could promote epitaxial growth and could be removed with bio-friendly methods was investigated.

Zn film is envisioned as an excellent candidate for the sacrificial layer for micro-origami patterns, because it can be selectively removed by sublimation in vacuum at relatively low temperatures. Because initial experiments showed that Zn films that were grown by sputtering and e-beam evaporation directly on sapphire substrate were polycrystalline and rough, Ru and Ti layers were introduced to serve as buffer layers on sapphire. Both Ru and Ti films were good quality single crystals, as evidenced by RHEED patterns. Films that were grown on Ru, were strongly dependent on the deposition conditions such as rate and temperature. Increasing deposition rate decreased grain size while sacrificing crystallinity and increasing temperature promoted crystalline growth in the form of island growth and not a uniform film. Smoother films were found to grow at room temperature by e-beam evaporation on Ti buffer layer. Growth of Zn on Ti layers

seems to be a mixture of layer and grain form which turns into a more uniform film with increasing thickness.

Zn films that grew in crystalline form (either island or Stranski/Krastanov modes[16]) on both Ru and Ti buffer layers were successfully sublimated in vacuum chamber by increasing the substrate temperature to 200°C.

As a bio friendly option, epitaxial growth of NaCl as sacrificial layer on (001) MgO substrate was investigated. Electron beam evaporation was used to deposit single crystal NaCl on MgO substrate. Modifying surface of MgO with 5nm e-beam evaporated MgO improves the roughness and epitaxy of the films grown on top of it. The optimum temperature for the growth of the heteroepiaxial structures was found to be 350°C for the epitaxial layers of NaCl/Cr or NaCl/Fe.

To sum up, epitaxial thin films of Zn and NaCl were successfully grown on appropriate substrates and their easy and clean removal process promises a feasible release mechanism for the layers that are grown on top of them. Additionally, their epitaxial growth also promotes epitaxial growth of upper films which gives better control of bending and curving of the origami structures by stress engineering at the interface of the films.

References

1. Prinz V. Ya, Vorob'ev A. B., S. V. A. Three-dimensional structuring using self-rolling of strained InGaAs/GaAs films. in *Compound Semiconductors 2001* **170,** 319–323 (2002).
2. Li, X. Strain induced semiconductor nanotubes: from formation process to device applications. *J. Phys. D. Appl. Phys.* **41,** 193001 (2008).
3. Prinz, V. Y. *et al.* Free-standing and overgrown InGaAs/GaAs nanotubes, nanohelices and their arrays. *Phys. E* **6,** 828–831 (2000).
4. Deneke, C. *et al.* Fabrication of radial superlattices based on different hybrid materials. *Phys. Status Solidi Curr. Top. Solid State Phys.* **5,** 2704–2708 (2008).
5. Schumacher, O. *et al.* Lithographically defined metal-semiconductor-hybrid nanoscrolls. *Appl. Phys. Lett.* **86,** 143109 (2005).
6. Clemens, B. M. & Eesley, G. L. Relationship between interfacial strain and the elastic response of multilayer metal films. *Phys. Rev. Lett.* **61,** 2356–2359 (1988).
7. Chun, I. S., Challa, A., Derickson, B., Hsia, K. J. & Li, X. Geometry effect on the strain-induced self-rolling of semiconductor membranes. *Nano Lett.* **10,** 3927–3932 (2010).
8. Freund, L. B. & Suresh, S. *Thin film materials: stress, defect formation and surface evolution.* (Cambridge University Press, 2003).
9. Min, S. *et al.* Fabrication of scrolled magnetic thin film patterns. *J. Appl. Phys.* **111,** 2014–2017 (2012).
10. Min, S. *et al.* Novel approach to control diameter of self-rolled magnetic microtubes by anodizing ti layer. *IEEE Magn. Lett.* **3,** 4000304 (2012).
11. Malkinski, L. & Eskandari, R. in *Magnetic Materials* (ed. Maaz, K.) (InTech, 2016).
12. Yamaguti, T. & Watanabe, Y. Sublimation of cleaved surfaces of zinc and galena single crystals I: Experimental. *Thin Solid Films* **147,** 57–64 (1987).
13. Campbell, C. T. Ultrathin metal films and particles on oxide surfaces: structural, electronic and chemisorptive properties. *Surf. Sci. Rep.* **27,** 1–111 (1997).
14. Sutter, P. W., Albrecht, P. M. & Sutter, E. A. Graphene growth on epitaxial Ru thin films on sapphire. *Appl. Phys. Lett.* **97,** 213101 (2010).
15. Søndergård, E., Kerjan, O., Barreteau, C. & Jupille, J. Structure and growth of titanium buffer layers on Al_2O_3(0001). *Surf. Sci.* **559,** 131–140 (2004).
16. Ohring, M. *Materials science of thin films: deposition and structure.* (Academic Press, 2002).
17. Peddada, S. R., Robertson, I. M. & Birnbaum, H. K. Growth of Ti thin films on sapphire substrates. *J. Mater. Res.* **12,** 1856–1865 (1997).

Appendix: Copyright Permissions

Copyright Clearance Center

Note: Copyright.com supplies permissions but not the copyrighted content itself.

1 PAYMENT | 2 REVIEW | 3 CONFIRMATION

Step 3: Order Confirmation

Thank you for your order! A confirmation for your order will be sent to your account email address. If you have questions about your order, you can call us 24 hrs/day, M-F at +1.855.239.3415 Toll Free, or write to us at info@copyright.com. This is not an invoice.

Confirmation Number: 11640470
Order Date: 04/26/2017

If you paid by credit card, your order will be finalized and your card will be charged within 24 hours. If you choose to be invoiced, you can change or cancel your order until the invoice is generated.

Payment Information

Rahmatollah Eskandari
reskanda@uno.edu
+1 (504) 638-5649
Payment Method: n/a

Order Details

Reports on Progress in Physics

Order detail ID: 70403098
Order License Id: 4096340548070
ISSN: 0034-4885
Publication Type: Journal
Volume:
Issue:
Start page:
Publisher: IOP Publishing

Permission Status: Granted
Permission type: Republish or display content
Type of use: Thesis/Dissertation
View details

Note: This item will be invoiced or charged separately through CCC's **RightsLink** service. More info **$ 0.00**

Total order items: 1

This is not an invoice.

Order Total: 0.00 USD

Copyright Clearance Center

Note: Copyright.com supplies permissions but not the copyrighted content itself.

1 PAYMENT | 2 REVIEW | 3 CONFIRMATION

Step 3: Order Confirmation

Thank you for your order! A confirmation for your order will be sent to your account email address. If you have questions about your order, you can call us 24 hrs/day, M-F at +1.855.239.3415 Toll Free, or write to us at info@copyright.com. This is not an invoice.

Confirmation Number: 11640472
Order Date: 04/26/2017

If you paid by credit card, your order will be finalized and your card will be charged within 24 hours. If you choose to be invoiced, you can change or cancel your order until the invoice is generated.

Payment Information

Rahmatollah Eskandari
reskanda@uno.edu
+1 (504) 638-5649
Payment Method: n/a

Order Details

Journal of micromechanics and microengineering : structures, devices, and systems

Order detail ID: 70403100
Order License Id: 4096350187711
ISSN: 0960-1317
Publication Type: Journal
Volume:
Issue:
Start page:
Publisher: INSTITUTE OF PHYSICS PUBLISHING

Permission Status: Granted
Permission type: Republish or display content
Type of use: Thesis/Dissertation
View details

Note: This item will be invoiced or charged separately through CCC's **RightsLink** service. More info **$ 0.00**

This is not an invoice.

Total order items: 1

Order Total: 0.00 USD

AIP PUBLISHING LLC LICENSE
TERMS AND CONDITIONS

Apr 26, 2017

This Agreement between Rahmatollah Eskandari ("You") and AIP Publishing LLC ("AIP Publishing LLC") consists of your license details and the terms and conditions provided by AIP Publishing LLC and Copyright Clearance Center.

License Number	4096350748320
License date	
Licensed Content Publisher	AIP Publishing LLC
Licensed Content Publication	Journal of Applied Physics
Licensed Content Title	Fabrication of scrolled magnetic thin film patterns
Licensed Content Author	
Licensed Content Date	Apr 1, 2012
Licensed Content Volume	111
Licensed Content Issue	7
Type of Use	Thesis/Dissertation
Requestor type	Student
Format	Print and electronic
Portion	Figure/Table
Number of figures/tables	1
Title of your thesis / dissertation	Ferroelectric-Semiconductor Systems for New Generation of Solar Cells
Expected completion date	May 2017
Estimated size (number of pages)	120
Requestor Location	Rahmatollah Eskandari 2000 Lakeshore Dr. Science Bldg University of New Orleans NEW ORLEANS, LA 70148 United States Attn: Rahmatollah Eskandari
Billing Type	Invoice
Billing Address	Rahmatollah Eskandari 2000 Lakeshore Dr. Science Bldg University of New Orleans NEW ORLEANS, LA 70148 United States Attn: Rahmatollah Eskandari
Total	0.00 USD

ELSEVIER LICENSE
TERMS AND CONDITIONS

Apr 26, 2017

This Agreement between Rahmatollah Eskandari ("You") and Elsevier ("Elsevier") consists of your license details and the terms and conditions provided by Elsevier and Copyright Clearance Center.

License Number	4096341172261
License date	
Licensed Content Publisher	Elsevier
Licensed Content Publication	Microelectronic Engineering
Licensed Content Title	A new concept in fabricating building blocks for nanoelectronic and nanomechanic devices
Licensed Content Author	V.Ya Prinz
Licensed Content Date	September 2003
Licensed Content Volume	69
Licensed Content Issue	2-4
Licensed Content Pages	10
Start Page	466
End Page	475
Type of Use	reuse in a thesis/dissertation
Intended publisher of new work	other
Portion	figures/tables/illustrations
Number of figures/tables/illustrations	1
Format	both print and electronic
Are you the author of this Elsevier article?	No
Will you be translating?	No
Order reference number	
Original figure numbers	Figure 1
Title of your thesis/dissertation	Ferroelectric-Semiconductor Systems for New Generation of Solar Cells
Expected completion date	May 2017
Estimated size (number of pages)	120
Elsevier VAT number	GB 494 6272 12
Requestor Location	Rahmatollah Eskandari 2000 Lakeshore Dr. Science Bldg University of New Orleans NEW ORLEANS, LA 70148 United States Attn: Rahmatollah Eskandari
Publisher Tax ID	98-0397604
Total	0.00 USD

THE AMERICAN ASSOCIATION FOR THE ADVANCEMENT OF SCIENCE LICENSE TERMS AND CONDITIONS

Apr 26, 2017

This Agreement between Rahmatollah Eskandari ("You") and The American Association for the Advancement of Science ("The American Association for the Advancement of Science") consists of your license details and the terms and conditions provided by The American Association for the Advancement of Science and Copyright Clearance Center.

License Number	4096340946632
License date	
Licensed Content Publisher	The American Association for the Advancement of Science
Licensed Content Publication	Science
Licensed Content Title	A method for building self-folding machines
Licensed Content Author	S. Felton,M. Tolley,E. Demaine,D. Rus,R. Wood
Licensed Content Date	Aug 8, 2014
Licensed Content Volume	345
Licensed Content Issue	6197
Volume number	345
Issue number	6197
Type of Use	Thesis / Dissertation
Requestor type	Scientist/individual at a research institution
Format	Print and electronic
Portion	Figure
Number of figures/tables	1
Order reference number	
Title of your thesis / dissertation	Ferroelectric-Semiconductor Systems for New Generation of Solar Cells
Expected completion date	May 2017
Estimated size(pages)	120
Requestor Location	Rahmatollah Eskandari 2000 Lakeshore Dr. Science Bldg University of New Orleans NEW ORLEANS, LA 70148 United States Attn: Rahmatollah Eskandari
Billing Type	Invoice
Billing Address	Rahmatollah Eskandari 2000 Lakeshore Dr. Science Bldg University of New Orleans NEW ORLEANS, LA 70148 United States Attn: Rahmatollah Eskandari
Total	0.00 USD

AIP PUBLISHING LLC LICENSE
TERMS AND CONDITIONS

Apr 26, 2017

This Agreement between Rahmatollah Eskandari ("You") and AIP Publishing LLC ("AIP Publishing LLC") consists of your license details and the terms and conditions provided by AIP Publishing LLC and Copyright Clearance Center.

License Number	4096330952651
License date	
Licensed Content Publisher	AIP Publishing LLC
Licensed Content Publication	Journal of Applied Physics
Licensed Content Title	Theory of the electrical and photovoltaic properties of polycrystalline silicon
Licensed Content Author	Amal K. Ghosh,Charles Fishman,Tom Feng
Licensed Content Date	Jan 1, 1980
Licensed Content Volume	51
Licensed Content Issue	1
Type of Use	Thesis/Dissertation
Requestor type	Student
Format	Electronic
Portion	Figure/Table
Number of figures/tables	1
Title of your thesis / dissertation	Ferroelectric-Semiconductor Systems for New Generation of Solar Cells
Expected completion date	May 2017
Estimated size (number of pages)	120
Requestor Location	Rahmatollah Eskandari 2000 Lakeshore Dr. Science Bldg University of New Orleans NEW ORLEANS, LA 70148 United States Attn: Rahmatollah Eskandari
Billing Type	Invoice
Billing Address	Rahmatollah Eskandari 2000 Lakeshore Dr. Science Bldg University of New Orleans NEW ORLEANS, LA 70148 United States Attn: Rahmatollah Eskandari
Total	0.00 USD

AIP PUBLISHING LLC LICENSE
TERMS AND CONDITIONS

Apr 26, 2017

This Agreement between Rahmatollah Eskandari ("You") and AIP Publishing LLC ("AIP Publishing LLC") consists of your license details and the terms and conditions provided by AIP Publishing LLC and Copyright Clearance Center.

License Number	4096330765054
License date	
Licensed Content Publisher	AIP Publishing LLC
Licensed Content Publication	Applied Physics Letters
Licensed Content Title	High efficient photovoltaics in nanoscaled ferroelectric thin films
Licensed Content Author	Meng Qin, Kui Yao, Yung C. Liang
Licensed Content Date	Sep 22, 2008
Licensed Content Volume	93
Licensed Content Issue	12
Type of Use	Thesis/Dissertation
Requestor type	Student
Format	Electronic
Portion	Figure/Table
Number of figures/tables	1
Title of your thesis / dissertation	Ferroelectric-Semiconductor Systems for New Generation of Solar Cells
Expected completion date	May 2017
Estimated size (number of pages)	120
Requestor Location	Rahmatollah Eskandari 2000 Lakeshore Dr. Science Bldg University of New Orleans NEW ORLEANS, LA 70148 United States Attn: Rahmatollah Eskandari
Billing Type	Invoice
Billing Address	Rahmatollah Eskandari 2000 Lakeshore Dr. Science Bldg University of New Orleans NEW ORLEANS, LA 70148 United States Attn: Rahmatollah Eskandari
Total	0.00 USD

AIP PUBLISHING LLC LICENSE
TERMS AND CONDITIONS

Apr 26, 2017

This Agreement between Rahmatollah Eskandari ("You") and AIP Publishing LLC ("AIP Publishing LLC") consists of your license details and the terms and conditions provided by AIP Publishing LLC and Copyright Clearance Center.

License Number	4096330497730
License date	
Licensed Content Publisher	AIP Publishing LLC
Licensed Content Publication	Applied Physics Letters
Licensed Content Title	Ferroelectricity in hafnium oxide thin films
Licensed Content Author	T. S. Böscke,J. Müller,D. Bräuhaus, et al.
Licensed Content Date	Sep 5, 2011
Licensed Content Volume	99
Licensed Content Issue	10
Type of Use	Thesis/Dissertation
Requestor type	Student
Format	Electronic
Portion	Figure/Table
Number of figures/tables	1
Title of your thesis / dissertation	Ferroelectric-Semiconductor Systems for New Generation of Solar Cells
Expected completion date	May 2017
Estimated size (number of pages)	120
Requestor Location	Rahmatollah Eskandari 2000 Lakeshore Dr. Science Bldg University of New Orleans NEW ORLEANS, LA 70148 United States Attn: Rahmatollah Eskandari
Billing Type	Invoice
Billing Address	Rahmatollah Eskandari 2000 Lakeshore Dr. Science Bldg University of New Orleans NEW ORLEANS, LA 70148 United States Attn: Rahmatollah Eskandari
Total	0.00 USD

VITA

Rahmatollah Eskandari was born in Zanjan province in Iran. He got admitted to the Amirkabir University of Technology in 1997 and graduated with Bachelor of Science in Applied Physics in 2002. Then he joined University of Tabriz for the program of Master of Science in Solid State Physics and graduated in 2006. He then worked at Materials and Energy Research Center in Tehran as a process engineer and lab manager until 2010 before joining Advanced Materials Research Institute at the University of New Orleans. He started his doctoral study in Engineering and Applied Science (ENAS) program with concentration in Physics in summer 2011.